August 2019

Interfacial Interactions and Dynamic Adhesion of Synthetic and Living Colloids in Flow

Molly Shave

Interfacial Interactions and Dynamic Adhesion of Synthetic and Living Colloids in Flow

A Dissertation Presented
by
MOLLY K. SHAVE

Submitted to the Graduate School of the University of Massachusetts Amherst in partial fulfillment of the requirements for the degree of

DOCTOR OF PHILOSOPHY

May 2019

Polymer Science and Engineering

Interfacial Interactions and Dynamic Adhesion of Synthetic and Living Colloids in Flow

A Dissertation Presented
by
MOLLY K. SHAVE

Approved as to style and content by:

_____
Maria M. Santore, Chair

_____
Greg Grason, Member

_____
Jessica Schiffman, Member

_____
E. Bryan Coughlin, Department Head
Polymer Science and Engineering

ACKNOWLEDGEMENTS

I would like to thank the Department of Polymer Science and Engineering at UMass Amherst for the opportunity to pursue my Ph.D. This work was partially funded by the National Research Service Award T32 GM008515 from the National Institutes of Health through the UMass Chemistry and Biology Interface program and NSF Award #1264855.

I would like to thank my advisor Dr. Maria Santore for all the help and guidance throughout my thesis work. Her knowledge and experience were extremely helpful as she encouraged me to grow as a scientist. I would also like to thank the members of my committee, Dr. Jessica Schiffman and Dr. Greg Grason, for their helpful discussions, comments and suggestions during this project.

I would like to thank everyone in my group over the years, Surachate Kalasin, Bing Fang, Dong Chen, Aaron Chen, Hao Wan and Weiyue Xin. They provided many thoughtful discussions and friendship throughout my time here. I would also like to thank the undergraduate students who I have had the opportunity to mentor and work with throughout the years, in particular, Aiste Balciunaite and Eric Ying. I would like to thank my collaborators Vishnu Raman from the Forbes lab as well as Kris Kolewe and Irene Kurtz from the Schiffman Lab for all their help with my project. Additionally, I would like to thank the Schiffman Lab for welcoming me into their lab, without which my bacteria projects would not have been possible.

Finally, I would like to thank my friends and family for all their support through the years, especially my parents, MaryJane and Dick Shave, and my sister, Jill Shave.

ABSTRACT

INTERFACIAL INTERACTIONS AND DYNAMIC ADHESION OF SYNTHETIC AND LIVING COLLOIDS IN FLOW

MAY 2019

MOLLY K. SHAVE

B.S., COLORADO SCHOOL OF MINES

M.S., UNIVERSITY OF MASSACHUSETTS - AMHERST

Ph.D., UNIVERSITY OF MASSACHUSETTS - AMHERST

Directed by: Professor Maria M. Santore

This thesis focuses on the interactions between flowing particles and a surface, where hydrodynamics couples with chemical interactions in order to modify the way they come into play.

First this thesis shows how electrostatic chemical heterogeneities on a flowing particle affect the interactions with a wall, using a highly tunable electrostatically heterogenous system produced by adsorbing small amounts of cationic polyelectrolytes onto silica particles in suspension and studying their behavior in flow over the fixed surface. By comparing this behavior to a system with equivalent chemical heterogeneity on a channel wall it was shown that the rotation of a particle will produce a lower attempt frequency, resulting in chemical heterogeneity being less effective on a flowing particle then on a fixed surface. This establishes the importance of hydrodynamics in the chemical interactions of flowing colloids.

Next this work shows how swimming of *Escherichia coli* increases both the frequency of bacteria encountering a surface and the durations of the resulting engagements, in an unconfined flowing environment, due to hydrodynamic interactions between bacteria and surfaces. This swimming effect was decoupled from the effect of flagella interactions. It was found that the presence of flagella, when not active, producing steric kicks, increasing the escape frequency and as a result reducing surface engagements length. Expansion of this work showed that the effects caused by morphological differences between bacteria strains can be significantly reduced by altering the mechanical properties of a surface coating.

Finally, this thesis shows that rod shaped particles are able to diffuse through a concentration boundary layer and adhere to surfaces at a rate faster than possible with spherical particles, due to hydrodynamic interactions between the non-spherical particles and the surrounding fluid. Current literature contains a wide variety of experiential results and mathematical predictions for the behavior of rods in flow but the lack of consistent systems with well-studied spherical controls has led to many discrepancies in their results. This thesis addresses these apparent discrepancies using model rod-shaped silica particle suspensions and spherical controls. Overall, this thesis probes the effects of three hydrodynamic effects on interactions between particles and surfaces in the presence of flow.

TABLE OF CONTENTS

Page

LIST OF TABLES

Table **Page**

LIST OF FIGURES

Figure **Page**

LIST OF ABBREVIATIONS

B. subtilis: Bacillus subtilis

BSA: Bovine Serum Albumin

CDC: Center for Disease Control

CGSC: Coli Genetic Stock Center

DLS: Dynamic Light Scattering

DLVO Theory: Derjaguin, Landau, Verwey, and Overbeek Theory

E. coli: *Escherichia coli*

LB: Luria-Bertani broth

PB: Phosphate Buffer

PBS: Phosphate Buffered Saline

PEG: Polyethylene glycol

PDMS: Polydimethylsiloxane

PLL: Poly-(L-Lysine)

PVP: Polyvinylpyrrolidone

Re_p: Reynolds number of a particle

SEM: Scanning Electron Microscopy

St: Stokes number

TEOS: Tetra-ethyl orthosilicate

CHAPTER 1

INTRODUCTION

The interactions between colloids or bacteria and surfaces are critical in many industrial[1–4] and natural[5] systems. While many models[6] for such interactions focus on simple spheres, this thesis focuses on certain particle properties that, when coupled with hydrodynamic particle behaviors, dominate the ultimate behavior of systems and produce results that are quantitively different then seen for uniform spheres. Initially, the question of the effect of charge heterogeneity on a particle, motivated by studies of charge heterogeneity on surface,[7,8] led to the discovery that as a result of particle rotation (a hydrodynamic effect) the effect of surface chemistry plays out differently.[9] This led to probing of different potential ways that complex hydrodynamics of particles or cells could be used to influence interactions with surfaces. This thesis will focus on how the particle surface heterogeneity, motility of bacteria, and particle shape all use hydrodynamic interactions to effect particle or cell-wall interactions. All three of these present a different and unique set of considerations to consider when looking at the interactions.

1.1 Surface Heterogeneity

Most surfaces are not uniform and have some degree of heterogeneity. Surface heterogeneity can be in the form of chemical heterogeneity or topographical heterogeneity. The presence of heterogeneity causes behavior that is often different from the mean field behavior,[10–12] yet these differences are extremely system dependent. For example, chemical surface heterogeneity on polymeric materials has been shown to dominate the wetting and contact angle behavior,[13–15] while impurities in minerals[16–19] and chemical

heterogeneity[11,20–24] in colloidal dispersions often cause aggregation.[25–30] Topographical heterogeneity or roughness has long been known to increase friction between surfaces.[31,32] The length scales of heterogeneity in systems is highly variable ranging from a few nanometers to about a micron. Depending on the length scale of the roughness, it can either increase or decrease colloid attachment on surfaces.[31]

1.1.1 Surface Heterogeneity in Biological Systems

In addition to surface heterogeneity found in material systems, nearly all biological surfaces, especially cells, are heterogeneous. Within the cell membrane there is an extremely heterogenous distribution of phospholipids and proteins that make up the exterior of the cell.[33–35] Some of these proteins contain functional groups are receptors that will only bind with certain ligands. This leads to a heterogenous distribution of potential binding sites. The charge of surface proteins can make different sections of a bacterium have different surface charges. For example, both the gram-negative *Escherichia coli* (*E. coli)* and the gram-positive *Bacillus subtilis* have a different surface charge on their poles then the on the sides of the cells.[36–38]

In addition to surface heterogeneity resulting from the structure of phospholipids, extracellular organelles can contribute additional heterogeneity. For example, many bacteria have pili which extend up to 100 nm from the surface of the cell and have different chemical functionality than the body of the cell.[39,40]

1.1.2 Electrostatic Heterogeneity

Surfaces with electrostatic heterogeneity deviate from theoretical models which rely on average surface properties.[6,41,42] The interactions between colloidal particles are classically

modeled with the Derjaguin, Landau, Verwey, and Overbeek (DLVO) Theory (Equation 1.1) which treats the force between particles or particles and surfaces as the sum of the van der Waals attractive forces and the electrostatic double layer forces.

$$F_{DLVO} = F_{vdW} + F_{dl} \quad (1.1)\ ^{41}$$

Where F_{vdW} is the van der Waals forces between particle and surface and F_{dl} is the electrostatic double layer force. The van der Waals forces are insensitive to the ionic strength of the solution in the region of ionic strengths studied in this dissertation and can be approximated using the by Equation 1.2,

$$F_{vdW} = \frac{-Ar}{6D} \quad (1.2)\ ^{41}$$

where A is the Hamaker constant, r is the particle radius, and D is the distance between two particles or a particle and a surface. The double layer force between two spheres is (Equation 1.3),

$$F_{dl} = \frac{64\pi k_B T r \rho_\infty \gamma^2}{\kappa^2} e^{-\kappa D} \quad (1.3)\ ^{41}$$

where ρ_∞ is the number density of ions in the bulk solution, κ^{-1} is the Debye length (equation 1.4), γ is the reduced surface potential (shown in Equation 1.5 for a symmetric electrolyte), and D is the distance between the particles. The double layer force is the electrostatic component of the interactions and depends on the Debye length κ^{-1}. Physically, the Debye length is the length where the electrostatic potential decreases by 1/e. The inverse Debye length and the reduced surface potential are,

$$\kappa = \sqrt{\sum_i \frac{\rho_{\infty i} e^2 {z_i}^2}{\varepsilon \varepsilon_0 k_B T}} \quad (1.4)\ ^{41}$$

$$\gamma = \tanh\left(\frac{z_i e \psi_0}{4 k_b T}\right) \quad (1.5)\ ^{41}$$

where z is the valency of the ion, ε the dielectric constant, ε_0 is the permittivity of free space, and ψ_0 is the reduced surface potential. Combining these for silica at different salt concentrations gives an interaction force with a secondary minimum due to the van der Waals attractions and an energy barrier due to the electrostatic repulsions between surfaces and particles with like charge. As the salt concentration is increased, this energy barrier is lowered, allowing for particles to adhere due to van der Waals attraction. At ionic strength both the Debye length and the energy barrier are larger, which will give a stable solution of individual colloids. While the equations above are for two particles in a symmetric electrolyte the same principles apply for the systems studied, mainly a particle-wall interaction in an asymmetric electrolyte.

In the presence of electrostatic heterogeneity, the use of average properties in the DLVO theory fails to accurately predict the stability of suspensions or the interactions between particles or between particles and surfaces. To account for deviation from predicted behaviors models have added an attractive non-DLVO force between the regions of heterogeneity and the underlying exposed areas on the colloid.[43,44] A qualitative charged patch attraction model for these faster aggregations was first proposed by Gregory.[20,22] Miklavic, et al. proposed a quantitative model for the long range attractions but this model has been shown to be limited due to insensitivity to short range interactions. [44–46] Popa, et al. modeled this as an additional attractive non-DLVO attractive force and showed that this treatment agreed with the charge patch attraction models.[47]

While the models of the previous paragraph were developed for electrostatic heterogeneity, significant research has been done on the interactions between a heterogeneous flat surface

and uniform spherical particles. It was shown that heterogeneity dominates the interactions, with adhesion occurring with as little as 10% of the surface being electrostatically attractive.[8] Surfaces, having nanometric clusters of cationic charge are highly controllable and have been shown to be able to mimic the behavior of biological mechanisms such as the rolling of leukocytes using a purely synthetic surface.[48,49] These types of surfaces can also be used to selectively capture cells lines or bacteria without the use of biological ligands or receptors.[50–52]

The studies discussed previously all focus on systems in which the functionality occurs on the fixed flat surface that is exposed to a colloid or colloidal dispersion. While many flat surfaces are heterogenous there is a need to determine the effect of location of heterogeneity as in nature the heterogeneity often occurs on the surface of the particle.

1.2 Swimming Behavior

The motility of colloids is an additional property that effect hydrodynamic properties of colloids or cells and effect their interactions with surfaces. Fundamentally the motion of a colloid is caused by a force on one side of the particle or bacteria. The work in this thesis focuses on swimming behavior of bacteria, specifically *E. coli* however it is instructive to consider the fundamental mechanics that driving swimming as a whole.

1.2.1 Mechanisms of Swimming at the Microscale

An understanding of swimming behavior of bacteria in quiescent conditions forms a basis for understanding swimming in shear. There are multiple mechanisms for swimming at the microscale. The first mechanism which will not be covered in detail, is important in the field of synthetic swimmers. This mechanism is commonly used in the design of synthetic

active colloids, with either a reactive component as part of a janus particle[53–55] or a catalytic site on a particle with the reactants in the solution.[56–58] In this mechanism a reaction is localized at one (or more) points on a colloid.[59] The reaction creates a concentration gradient in the solution in which the particle diffuses. Additionally, some of these self-propelled colloids have been designed to be light activated allowing for the easy turn on and off swimming behavior.[60,61] Similar non-appendage based swimming is also seen in bacteria in the *Listeria* genus, in which cells are propelled forward by the polymerization of an actin tail, while the tail can be considered an appendage it is the reaction not the motion of the tail that propels the bacteria forward.[62]

The majority of bacterial swimming at the microscale is done using extracellular appendages. Swimming using appendages at the microscale is very different then swimming in the macroscale world that we live in. The biggest different is that at a microscale swimming requires a series of motions that are nonreciprocal. Without the inertial effects (the ability to coast) present at the macroscale, the majority of mechanisms will have a net zero displacement. While the detailed mechanisms vary depending on the type of cell, there are two main classes of bacterial swimming. The first is a rigid helix power by a fixed motored that rotates, hereby propelling the cell forward. This is known as "the corkscrew", and the second is a flexible tail that propels the bacteria using whip-like motions, known as the "flexible oar".[63,64]

These appendage motions either push the cell forward away from the appendage, as in the case of *E. coli* or *Salmonella typhimurium*[65] or pull the cell back towards the appendage as in some strains of *Vibrio alginolyticus*.[66] Additionally there are some bacteria that,

depending on the direction of their flagella rotation, can switch directions. For example *Caulobacter crescentus* will travel forward when its single flagella rotates clockwise (when viewed looking along the flagella towards the body of the cell), but when travels backwards during counter-clockwise rotation.[67]

While exterior appendages are the mechanism for the majority of swimming bacteria there are bacteria that exploit other mechanisms. For example, *Spiroplasmas* are a small helically shaped bacteria that is approximately 150 nm wide by a few microns is able to swim by propagating a pair kinks down its body. This generates thrust along the length of the bacteria propelling it through the fluid.[68]

1.2.2 Swimming Behavior of *E. coli*

The work in this thesis focuses on the flagella driven swimming behavior of *E. coli*. The flagella itself consists of a motor that is attached to the body of the bacterium and a helical filament, and a hook connects the filament to its motor.[69] The flagella filaments are left-handed helices approximately 10 μm long with a filament diameter of about 20nm and a helix diameter of about 0.5 μm.[70] While the number of flagella can vary between strains a review reports that there are generally approximately four flagella per bacterium.[69]

When wild type *E. coli* swim, they undergo what is called a "run and tumble" behavior. This is illustrated in Figure 1. Initially during the "run" phase, the flagella are all bundled behind the bacteria and rotating in a counter clock wise direction (Figure 1a). At some instant one or more of the flagella motors reverse their rotation. This causes a transition from the "run" phase to the "tumble" phases as the flagella become unbundled and the cell becomes reoriented (Figure 1b).[69,71] Once the motors all return to counter clock wise

rotation, the flagella re-bundle as the cell moves forward (Figure 1c),[63] now running in a new direction (Figure 1d).

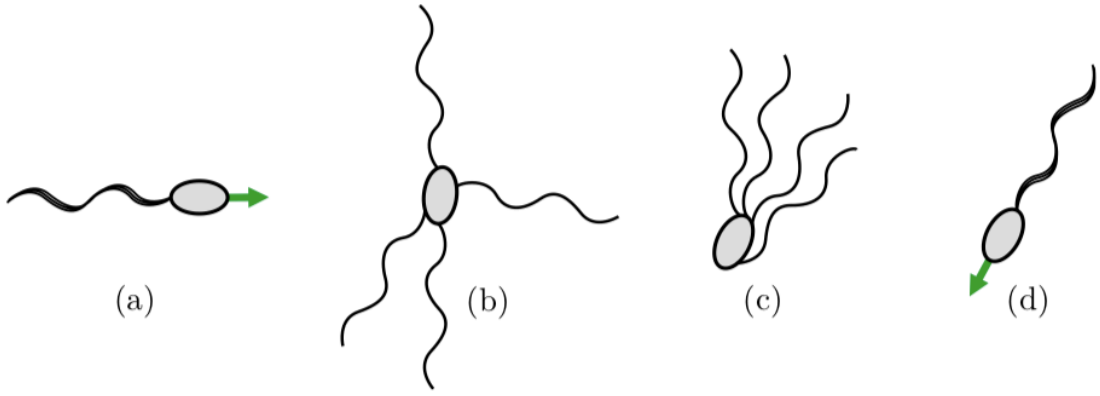

Figure 1. Bundling of bacteria flagella in *E.coli* "run and tumble" swimming. (a) during initial "run" the flagella are bundled tightly together. (b) a "tumble" the flagella motion reverses and flagella unbundle this randomly reorients the cell (c) hydrodynamic interactions bring flagella back together (d) flagella bundle together in different direction for next "run" phase. Figure from Lauga and Powers (2009) [63]

This "run and tumble" behavior benefits the bacteria because it allows the bacteria to undergo chemotaxis, or the ability of an organism to navigate based on chemical signals in its environment. A bacterium has no mechanisms to control its orientation, relying completely on the random orientation of each tumble. Bacteria can however control the frequency of tumbling events, going further before a tumble when traveling towards a nutrient source and tumbling more frequently when traveling away from the nutrient source.[72,73] In the laboratory setting *E. coli* have been genetically modified to remove the genes responsible for chemotaxis. This gives a strain that does not tumble and there for exhibits what is known as smooth swimming.[74] Smooth swimming cells travel in locally straight or gradually curved trajectories (comped with the size of the cells). These types of smooth swimming strains have been widely used in studies on how *E. coli* interacts with surfaces.

1.2.3 Bacteria Interactions

The work presented in this thesis occurs with bacteria suspensions in the dilute limit where interactions between bacteria do not contribute significantly to the interactions. However, it is helpful when considering the interactions between bacteria and surfaces to first consider the hydrodynamic forces generated by the bacteria and the potential for interactions with one another. As "pusher" bacteria, *E. coli* repel fluid away from the ends of the bacteria as they swim through the fluid. This creates a force inwards from the sides of the bacterium. When pullers are near one another in a fluid their quadrupoles cause a reorientation into a side by side cellular configuration.[63]

In addition to interactions between multiple bacterial cells, it is important to consider the interactions between swimming bacteria and surfaces. The presence of a surface affects the motion of the bacteria in multiple ways. For *E. coli*, one of the most studied wall effects is the difference in swimming behavior near walls. In the bulk solution, smooth swimming *E. coli* swims in a straight line due to the axisymmetric nature of the propulsion force when averaged over a full rotation of the flagella. Near a wall however the chiral nature of the propulsion leads to turning because the wall breaks this symmetry.[75] The rotation of the helical flagella near a wall creates a net force on the flagella perpendicular to the flagella bundle and parallel to the surface causing the bacteria to rotate. The left-handedness of the *E. coli* flagella helix causes the bacterium to turn to the right.[63,75] Another wall effect is similar to the hydrodynamic attraction effect between two bacteria. The flow field around a swimming bacterium will lead to a reorientation of the bacterium to orientate the body parallel to the surface. The quadrupoles then cause the bacteria to stay near the surface.[76]

This effect is seen in numerous systems.[76–79] These hydrodynamic attractions have been shown between particles and surfaces to elevate the concentration at the wall.[76,80]

1.2.4 Bacteria in Flow

The addition of flow further complicates the bacterial-surface interactions. The shear flow creates a torque on the bacteria that will cause periodic rotations. In the absence of motility and away from chamber walls these flow-induced rotations are known as Jeffery orbits.[81] In swimming bacteria these rotations can affect the bacteria's ability to chemotax.[82]

In microfluidic devices a depletion region has been seen for motile bacteria where there is a concentration gradient within the chamber and more bacteria present near the walls then the center of the chamber.[83] This shear trapping effect is a result of interactions of swimming hydrodynamics and a velocity gradient. It does not involve cell-wall interactions. Separately, the upstream swimming of bacteria or rheotaxis has been seen for many types of bacteria including *E. coli*.[82,84] It has been seen that, in high shear flows *E. coli* migrate into the corner or left sidewall of a channel or reside in a crevice facilitating upstream migration.[85] Prior studies however have been done in the confined regions of microfluidic channels where the geometry of the channel, (i.e. interactions with multiple walls) can play a significant role in the interactions.

1.3 Particle Shape

Particle shape is another important factor in studying the interactions between particles and surfaces in flow. Many particles in real world applications, including many bacteria, are not spherical but the majority of studies of particle behavior in flow have been carried out using spherical particles.

The current literature on the effect of particle shape in flow can mainly be classified into two categories. The first is the observation either by experiment or simulation of the flow and capture behavior of non-spherical particles. These observations lead to the second category of papers; the development of models to attempt to explain these often-unanticipated findings. The lack of studies that systematically vary particle features, or work with well characterized, uniform samples has made it difficult to corroborate and expand the mathematical models to the point where they can be used to predict *in vivo* behavior. In the current literature three types of particles are studied. Spheres which have an aspect ratio (L/D) of 1, rods which are elongated and have aspect ratios greater than 1, and finally disks with have an aspect ratio less than 1.

1.3.1 Particle Behavior in Flow

The behavior of any type of colloid or bacteria in flow near a surface can be broken up into two steps. First the transport of the particle through the bulk fluid towards or away from the surface. In the event that the transport brings the particle to the surface, the second step is possible static or dynamic engagement or adhesion to the surface.

1.3.1.1 Transport to Surface

Due to the fact that a lot of the literature involving non-spherical particles is related to drug delivery, it is common for the transport portion of the flow behavior to be referred to mainly as margination. Margination is an effective lateral drift velocity induced in flowing suspensions for particles or unlike cells in blood as a result of multibody interactions and competing hydrodynamic and inertial forces.[86] It should be noted that margination occurs as a result of multibody interactions and does not occur in dilute systems. In these dilute

systems and with small particles, diffusion is the primary mechanism of transport to a surface, in quiescence or shear flow.

Mathematical simulations by Lee et al. on the dynamics of a particles in linear laminar flow near a wall, showed that disk and rod-shaped particles exhibit significantly more margination than spherical particles, especially at higher flow velocities.[86] The simulations by Lee et.al however are only single particle simulations and don't account for the multibody interactions. Lee et. al found that particles that are closer to the wall and have a larger density or size tend to drift laterally, while particles far away from a wall, with a small size or small density relative to the fluid density do not exhibit as much lateral drift.[86] Overall they found that high aspect ratio discs have the most efficient lateral drift, then rods, then low aspect ratio discs and finally the spheres have the least efficient lateral drift.[86]

Recently studies have been done on the margination of particles in the presence of red blood cells. The resulting multibody interactions occurring between red blood cells and drug particles, produce a cell-free layer next to the blood vessel wall.[87] Vahidkah and Bagchi considered the behavior of disks and rods with two different aspect ratios, and spheres, in a three-dimensional simulation of a red blood cell suspension. They found that discs marginate to the cell-free layer more than spheres and rods, and that lower aspect ratios result in more effective margination.[87]

However, experiments by Apolito et. al studied the differences in margination of two sizes of spheres, disks, and rods in the presence of red blood cells within a microfluidic device.

In this study rods marginated less than all of the other particles with the largest spheres marginating the most effectively.[88]

Overall, many studies have established that particle shape has an effect on the margination of particles to the wall in a flowing system,[86,89–95] but the most effective particle shape seems to be highly system dependent which leads to the need for a highly controlled, systematic study of particle shape effects.

1.3.1.2 Adhesion to Surfaces

The adhesion of particles to a surface can be described as a two-step process. First is the initial contact with the surface and the second is adhesive binding, the strength of the adhesion. The strength of adhesion is typically determined by pull-off experiments, which measures the conditions required to remove particles adhered to the surface. If the strength of the adhesion is strong it will lead to irreversible adhesion on the time scales of the experiment. However, if the strength of the adhesion is weaker, it will be either reversible adhesion, where the particle later disengages from the surface, or dynamic adhesion, where the forces are never strong enough to fully arrest the particle. It is important to note that the mechanism of development of adhesive bonds between a particle and a surface is fundamentally independent of transport mechanisms, be they margination or diffusion in dilute solution.

1.3.1.2.1 Initial Contact

In simulations the initial contact of the particle with a surface can be decoupled from the transport of the particle to the surface and adhesive binding events; however, experiments have not yet been able to decouple these events. Simulations by Vahidkah and Bagchi

showed that rod-shaped particles are the most effective (compated to spheres and disks) at obtaining an initial surface contact in shear flow. They hypothesize that this is due to the lower energy barrier for a critical fluctuation that can drive contact with the surface. The longer thinner rods require less fluctuations than a disk or sphere would. Consistent with this theory rods with a higher aspect ratio had more initial surface contacts than rods with a shorter aspect ratio.[87]

1.3.1.2.2 Strength of Adhesion

In addition to the initial contact it is important to consider the strength and stability of an adhesive bond or contact. The strength of adhesion is the force required to dislodge a particle from the surface this depends on balance between, the net attractive forces between the surface and the wall and could be caused by electrostatics, Van der Waals attractions or receptor-ligand binding among others and hydrodynamic forces from the shear stress and torque attempting to dislodge the particle. The strength of these hydrodynamic forces depends on the geometric features of the particle such as size, shape and aspect ratio along with the orientation of the adhesion and flow conditions such as the wall shear rate.

In an experimental study, Kolhar et al. coated nanoparticles with antibodies, and coated the walls of a microfluidic system mimicking the vasculature with receptors to the antibodies. They used two type of antibodies: ones that exhibited specific binding to the receptors, and ones that exhibit non-specific binding to the receptors.[96] They found that spheres had higher levels of non-specific binding while rods exhibited higher levels of specific binding.[96] The authors hypothesized this was because rods require a stronger interaction to stably adhere to a surface, and specific binding interactions are stronger than non-specific binding interactions. In a separate microfluidic experiment Doshi et al. coated the walls of

a microfluidic chamber, with Bovine Serum Albumin (BSA) and the particles with anti-BSA. A bifurcation was present in the chamber. They studied the adhesion of spheres, elliptical disks, circular disks, and rods in a synthetic microvascular network. Disks were used to study the importance of flatness on adhesion, and rods were used to test the importance of elongation.[97] Compared to the other disks and spheres, rod-shaped particles had the highest capture efficiency.[97]

In a simulation, Vahidkah and Bagchi found, in studies with a constant shear rate (~1000s^{-1}), and particle volume (7.238 μm^3), that though rods have the highest probability of contact with the wall, disks adhere more firmly.[87] Though both Kolhar et al. and Doshi et al. suggest that rods adhere more to surfaces in flow than disks or spherical particles, the results of Vahidkah and Bagchi suggest this may be because rods are establishing an initial contact with the wall at a higher rate than spheres or disks, and subsequently adhering. Their results do not speak to the strength of adhesion of the particle. Overall experiments and simulations have not shown a conclusion on the behavior of non-spherical particles in flow in many of the metrics studied. These often-conflicting studies have motivated the development of models for the behaviors seen in simulations and experiments.

1.3.2 Mathematical Models of Non-Spherical Particles

The main difficulty in determining effects of particle shape has is the lack of consistency in the experimental systems being studied. Everything from the general flow parameters to the actual synthesis of particles is varied. With each paper using a different set of experimental parameters. These differences have made direct comparisons and the ability to draw conclusions about the effects of particle shape impossible. This has led to the use

of mathematical treatments to model behaviors, typically describing systems using dimensionless groups, and identifying regimes of different behaviors. The Reynolds number of the particle (Re_p), which is the ratio of the inertial to viscous forces of on the particle and the Stokes number (St) which corresponds to the behavior of a particle within a fluid. These are shown in Equations 1.6 and 1.7 respectively.

$$Re_p = \frac{\rho_f r_s U}{\mu} \quad (1.6)^{98}$$

$$St = \frac{\rho_p r_s^2 \dot{\gamma}}{\mu} \quad (1.7)^{98}$$

Where ρ_f is the fluid density, ρ_p is the particle density, r_s is the radius of a sphere with equivalent volume as the particle of interest, U is the fluid velocity, $\dot{\gamma}$ is the shear rate, and μ is the dynamic viscosity of water.

1.3.2.1 Behavior of Rods in Bulk Flow

When a sphere moves within a flowing fluid, tracking the particle position is relatively simple due to the symmetry of the particle. It will rotate due to the shear field but that rotational motion will not be observable due to the particle symmetry. Rods on the other hand can have a wide variety of different observable behaviors such as, tumbling, log-rolling, kayaking, wagging, or a steady motion through a fluid in shear flow.[99] Based on the characteristics of the fluid flow, some of these behaviors will be more favorable. For example, based on models by Rosen et. al for a particle with an aspect ratio of 4 and $Re_p <$ 14, tumbling will be highly favored. For $15 < Re_p < 90$, tumbling continues to be a major mechanism, but log rolling and kayaking are also seen in various sub regions. For $90 < Re_p < 150$, steady-state particle motion is seen that is the particle translate through the fluid with no rotational motion.[99] These regions are also seen in the simulations of Kim et.al. [98] It is believed that this tumbling motion is due to the particle inertia dominating the fluid

inertia. As the flow rates are increased the fluid motion begins to dominate as both the Re_p and St increase leading to a smooth motion behavior with particles all traveling along the streamlines in the direction of the fluid.[99]

1.3.2.2 Particle Transport to Surfaces

While it is important to consider the behavior of particles in the bulk in many applications the critical factor is the ability of the particles to get to the surface.

1.3.2.2.1 Diffusion Limited Transport

For sufficiently small spherical particles still governed by diffusion in bulk solution, it has been shown that the experimentally observed transport limited adhesion of particles, that is for a rapid attachment step to the surface relative to other timescales in the system, can is well-described by Leveque Equation (Equation 1.8).[100–102]

$$\frac{dc_s}{dt} = \frac{1}{\Gamma\left(\frac{4}{3}\right) 9^{1/3}} \left(\frac{\gamma}{\mathcal{D}x}\right)^{1/3} \mathcal{D}c_{Bulk} \qquad (1.8)^{100}$$

In the transport-controlled limit, the particle accumulation rate, dc_s/dt, depends on the bulk solution particle concentration, C; the dilute-limit free solution diffusion coefficient, D; the wall shear rate, γ; and x, the distance from the entrance of the flow chamber to the point of observation. On the right side of Equation 6.3 and only here, Γ is the gamma function. This is equation assumes that any particles that are able to interact with the surface adhere immediately creating a concentration boundary layer near the surface due to a particle depletion region at the surface. While this model has been confirmed to be extremely accurate for spherical particles a few microns or smaller in water, it assumes a single concentration /orientation independent diffusivity.

1.3.2.2.2 Transport of Rod-Shaped Particles

Similarly, to the differences in behavior of spherical and rod-shaped particles in the center of a channel where shear forces are low, it is important to consider the effect that shape can have on the transport through the fluid towards the high shear region. The diffusion of a rod in shear flow will depend on the balance of hydrodynamic and inertial forces that can induce a lateral drift velocity.[86] In the case of spherical particle, without presence of external forces such as diffusion, particles will tend to follow the streamlines,[91] non-spherical particles in the same conditions are not restricted to following streamlines. This lateral drift velocity, (the direction of which is random) of a particle increases with an increase in particle size, density, and rotational inertia.[86] While the direction is random, increased lateral drift velocity increases the probability of surface interactions.[86] Additionally, a rod-shaped particle can experience a wall-induced drift, in laminar flow with modest particle Reynolds number, which has two components: first, is that the wall breaks the particle wake symmetry, resulting in lift away from wall and second, flow relative to particle accelerates faster in the gap between the particle and the wall. This increases the pressure drop between the particle and the wall, resulting in a drift of the particle towards the wall.[103]

A model by Kim et. al found that the drag force on a rod-shaped particle near a wall increases as the particle moves away from the wall due to the faster fluid motion. This model used a cylinder with an aspect ratio of 5 in linear shear flow.[98] Kim et al considered the effects of increased Stokes number on particle migration to a wall and found that at St << 0.1, there is little to no net migration of the particle towards the wall but as St increases up to 20, particle migration to a wall and lateral drift velocity increase. However, above St

~ 20, particle drift velocity decreases again. They hypothesize this is because at St ~ O(10) the force imbalances on the rod are largest, allowing for more particle rotation and movement, moving the particle towards the wall.[98] The St numbers for systems used in this thesis are all <<1.

The results of Kim et. al align with those presented by Lee et al., who concluded that at low St numbers, spherical or non-spherical particles will exhibit little to no net migration in shear flow towards a wall.[86] These results seem to disagree with other experimental and simulation observations of rod behavior in shear flow[86,103] where it would seem that even a low St numbers rods migrate to a wall more effectively than spheres.

1.3.2.3 Hydrodynamic Forces

In addition to inertia (of both the fluid and the particle) the main hydrodynamic forces on a particle near a wall in shear flow are lift, drag and torque. The magnitude and effect of these forces will depend on the distance from the wall, the orientation and aspect ratio of the particle and the Re_p. In a simulation of a single 2D elliptical particle and varying the distance of the particle from the wall, orientation, aspect ratio, and Re number Zarghjami et. al found that the drag force on a particle is constant far away from the wall, increases as the particle reaches a critical point of a distance away from the wall proportional to its largest length scale, and then decreases again closer to the wall.[103] Similarly, the lift force fall from the wall is 0, it peaks at a critical point and then decreases as the particle get close to the wall. The torque on the rod is lower near the wall causing less rotation. [103] Overall these results of Zarhjami et. al suggest a critical layer in which these forces will all push the 2D ellipsoid towards the surface. Additionally, the authors found that increasing the Re number, will increases all three of these forces on the rod.[103] Interestingly, increasing

aspect ratio had a similar effect, except for in the drag force which decreased between aspect ratios of 1 to 2, increasing again above 2.[103]

Zarhjami et. al also studied the effect of particle orientation using their 2D simulation. As the particle orientation angle increases from 0° (shear direction) to 90° (perpendicular to flow), the drag force on the particle also increases.[103] When the particle is aligned with flow at an angle of 0°, the particle has no lift force. Between 0° and 90° the particle experiences a lift force towards the wall, with the opposite effect occurring between 90 and 180°.[103] As the orientation of a rod has a significant effect on whether the rod will move towards or away from the wall it quickly becomes clear that the typical tumbling motion is going to cause rapid changes in hydrodynamic forces making the ability to predict rod motion difficult. 3D simulations of this behavior have not been studied.

1.3.3 Significance and Motivation

Gentile et al. conducted studies on particle margination using 1 µm spheres, 1.5 µm x 0.3 µm discoidal particles, and 1.6 and 3.2 µm quasi hemispherical silicon particles, studying effect of shear rates between 5 – 50s^{-1}.The flow chamber used in these studies is orientated so that gravity will be perpendicular (pushing particles into surface) to the flow cell surface being studied.[92] Particle surface accumulation was measured by counting surface capture rate on a test wall that was rendered adhesive by coating with type I collagen from rat tail, a method similar to methods used in the present study. The main difference is that their flow cell is horizontal, and not vertical, meaning gravity increases both particle transport and adhesion to the surface. The particles used in this study were silica with a density of 2.0 g/m^3, dense enough that they cannot be modeled as neutrally buoyant. Additionally, rod shape particles were not considered in this study. The authors found that number

captured particles decreases with an increase in shear rate for all particles, with the largest decrease observed for the quasi-hemispherical particles, then spherical ones, and finally discoidal particles.[92] Also, the Leveque equation described above describes an increase in particle transport with an increase in shear rate an opposite trend then is found in this study. Prior experiments from the Santore group have been consistent with Leveque's predictions.[8,51,104–106] The studies in this chapter address this apparent discrepancy, examining the capture of rod-shaped particles on an adhesively functionalized channel wall, similar to cases described by recent models. The study in this thesis orients the collecting surface to avoid the impact of gravity on particle transport and adhesion, so that particle shape may be more closely studied.

Overall the main conclusion that is drawn from current literatures is that spherical particles and rod shape particles behave very differently in flow, including their behavior in the bulk flow to the difference in transport rate to the surface and the forces on near surface particles. A lack of uniformity in studies has left a number of conflicting results. This has led us to the design a model system to study the effect of particle aspect ratio on the transport of particles to surface.

1.4 This Thesis

Chapter 2 addresses the effects of charge heterogeneity on the capture of flowing particles in shear flow, now placing the electrostatic heterogeneity on flowing spherical particles rather than on the wall of a flow chamber, as had been done previously. The work was designed to closely parallel previous studies of heterogeneously functionalized flow chamber walls, enabling quantitative comparison between systems in which the particles or the wall carried the charge heterogeneity. These studies were facilitated by the creation

and characterization of heterogeneously charged silica microparticles and the development of methods to allow their study in flow experiments before the dispersions aggregated.

Chapter 3 addresses the impact of bacteria swimming on biomaterial interactions with flowing cells. While many studies of swimming bacteria have focused on microfluidic chamber design and the impact of a wall on hydrodynamic interactions, this thesis focuses on how swimming dynamics and bacterial morphology influence biomaterial interactions, understood in terms of colloidal or surface forces, involving a single planar surface in shear flow. These physicochemical interactions are necessarily shorter range than the hydrodynamic interactions typically associated with swimming. The thesis addresses how the presence of a predominantly non-adhesive biomaterial PEG coating, with weak reversible interactions with *E. coli* cells influences bacterial dynamics. The study decouples swimming interactions from physical chemistry using an experimental design in which aggressively swimming cells are compared with a parent strain and non-motile variants which lack either flagella or motors that drive the flagella

Chapter 4 will expand on the chapter 3 and additionally explores the effects of surface mechanics on the bacteria surface interactions. We show in this objective that the mechanical properties of a surface can have dramatic effect on a bacteria's ability to engage with the surface with the softest hydrogel surfaces effectively eliminating the differences between different bacteria types seem in Chapter 3.

Finally, **Chapter 5** addresses the impact of particle shape on the interactions of flowing microparticles with a strongly adhesive wall. The study, conducted in collaboration with

UMass student Aiste Balciunaite, compared the capture of rod- and sphere-shape silica microparticles on a catatonically functionalized flow chamber wall. The work included a substantial effort to synthesize and characterize rod shaped particles, enabling variations in rod size and aspect ratio. The comparison between rod and spherical particles included pairings having the same particle volume or diameters and addressing the relative particle capture rates in the context of transport between the bulk solution and the surface.

The concluding remarks in **Chapter 7** summarize the findings and make recommendations for the next phases of study.

CHAPTER 2

ROTATION-CONTROLLED CAPTURE OF NANO-SCALE FUNCTIONALIZED PARTICLES FROM SHEAR FLOW

Adapted from: Shave, M.K.; Kalasin, S.; Ying, E.; Santore, M.M. Rotation-Controlled Capture of Nano-scale Functionalized Particles from Shear Flow. *ACS Applied Materials & Interfaces,* **2018**

2.1 Summary

Important processes in nature and technology involve the adhesive capture of flowing particles or cells on the walls of a conduit. This chapter introduces engineered spherical microparticles whose capture rates are limited by their near surface motions in flow. Specifically, these microparticles are sparsely functionalized with nanoscopic regions ("patches") of adhesive functionality, without which they would repel the conduit walls. Not only is particle capture on the wall of a shear-chamber limited by surface chemistry as opposed to transport, the capture rates depend specifically on particle rotations that result from the vorticity of the shear flow field. These particle rotations continually expose new particle surface to the opposing chamber wall, sampling the particle surface for an adhesive region and controlling the capture rate. Control studies with the same patchy functionality on the chamber wall rather than the particles reveal a related signature of particle capture but substantially faster (still surface limited) particle capture rates. Thus, when the same functionality is placed on the wall rather than the particles, the capture is faster because it depends on the particle translation past the functionalized wall rather than on the particle rotations. The dependence of particle capture on functionalization of the particles versus the wall is consistent with the faster near-wall particle translation in shearing flow,

compared with the velocity of the rotating particle surface near the wall. These findings, in addition to providing a new class of nanoscopically patchy engineered particles, provide insight into the capture and detection of cells presenting sparse distinguishing surface features and the design of delivery packages for highly targeted pharmaceutical delivery.

2.2 Introduction

From the workings of the immune system to cancer metastasis, from drug delivery to membrane fouling, and for mineral and bacterial transport in the environment, the capture of flowing particles on surfaces is critical in nature and technology. The flow sensitivity of particle deposition is a generally-accepted fact of life, since capture occurs when hydrodynamic forces are overcome by adhesive surface forces.[107–113] The surfaces forces themselves are often conceived as uniform (for instance following DLVO theory), but in many systems, roughness[114–117] and spatial variations in surface chemistry produce heterogeneities that discretize adhesive interactions, often producing interesting behavior.[118,119,128,120–127] Indeed intrinsic nanoscale heterogeneity has been identified as an important player in the capture and release of particles in flow.[31,129–132] Discretization length scales can approach molecular dimensions, and surface-bound molecules may interact across a nanometric gap.[46,133,134]

Molecular origins of adhesion include donor-acceptor pairings such as hydrogen bonding[135–139] and bimolecular ligand-receptor binding.[140–146] Particle capture governed by these interactions exhibits sensitivity to flow[136,139,147] or force. [140–146] For instance, the rolling of white blood cells on the inner walls of veins depends on coordination of cell motion and the forward binding rates of ligands and receptors on opposing surfaces:[148] cell capture is possible only when the binding rates are fast relative to the surface velocities of

the cell and the wall.[149] Additionally, the adhesion molecules on white blood cells exhibit force-sensitive dissociation.[150,151] Relatively simple model systems of hydrogen bondable brushy surfaces have also been demonstrated to exhibit highly flow-sensitive capture of particles.[136] These mechanisms now inspire targeted delivery strategies and cell capture schemes in the assessment of cancer treatment.[152–155]

Here we introduce engineered particles that exploit a different mechanism for the coupling of hydrodynamic and surface forces: capture controlled by particle rotation. (The particle rotation in this study is a result of the vorticity of the flow field.) This coupling mechanism applies in cases where a particle's capture is limited by its surface features, rather than by functionality, the collecting wall or by diffusive transport from bulk solution. In this study, engineered particles are sparsely functionalized with adhesive groups while the complimentary functionality on the wall is dense. This surface-based system therefore parallels the example of a second order reaction between two molecular species in solution where one is in excess and the reaction is controlled by the concentration of the second species. The particle-based system, however, adds the complexity of hydrodynamics. The resulting hydrodynamic coupling, because it involves the features of the particles, is highly relevant in delivery applications or other technologies relying on engineered particles.

We created micron-scale particles containing discrete nanoscopic adhesive features and studied their capture from shear flow onto a uniform wall that was adhesive only to the discrete features on the microparticles, in Figure 2. Without the adhesive features, the flowing silica microparticles were electrostatically repelled from the silica wall. We compared the capture of these functionalized particles on the uniform silica wall to a

control system with mirrored surface functionality: the same discrete adhesive features on the silica wall and the capture of uniform silica particles.

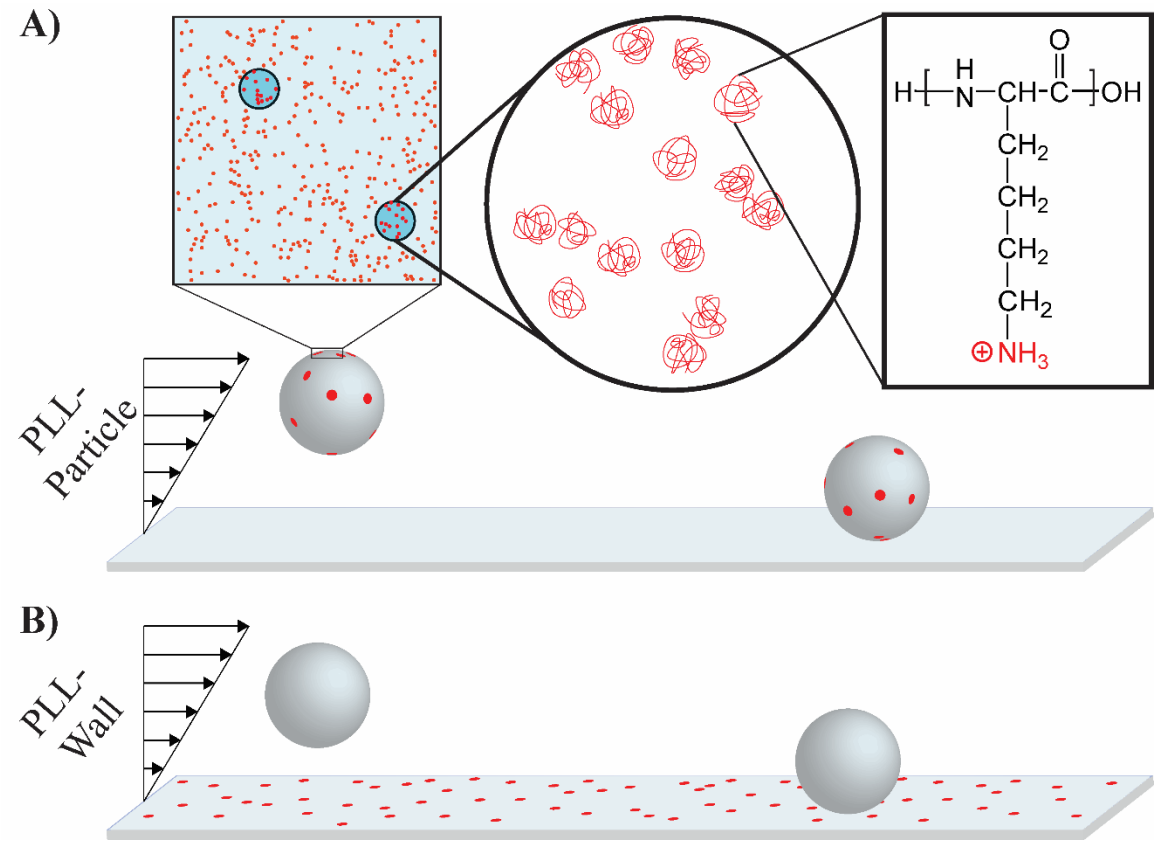

Figure 2. (A) Schematic of engineered particles containing nanoscopic adhesive features. Zoomed square is about 600 nm on each side and emphasizes the random placement and nanoscopic (10 nm approximate diameter) of the adhesive features, at a realistic loading of 1200/μm^2 corresponding to 0.04 mg/m^2 of PLL. The circle is size of zone of influence (defined below) at a Debye length of κ^{-1} = 2nm and has a diameter of ~90 nm. (B) Configuration for control experiment where adhesive features are placed on the wall and the particles are bare silica.

The adhesive features themselves were polycationic homopolymer chains, poly-l-lysine (PLL) on the order of 5-10 nm in size, randomly adsorbed[156] as shown in Figure 2. On negative silica surfaces at low levels, immobilized polycation chains produce isolated nanoscopic flat patches of positive charge on the otherwise negatively charged substrates.[105,106,156] The sparse regions of cationic charge from the PLL on the first surface

are attracted to an opposing uniformly negative silica surface. Placement of controlled amounts cationic features on silica microparticles rendered their surfaces rate limiting for particle capture on a silica wall, as shown in this work. Placement of the PLL on the wall rather than the particles, in control runs, facilitated particle capture rate limited by the wall, a behavior established using other polycations.[105,106,121,157,158]

Intuition, classical colloidal theory,[6] and computational schemes in the literature[32,118,159,160] suggest that surface forces between particles and a wall will be independent of placement of the polycations on the wall or the particle, as long as all other variables, especially the density of polycations, are fixed. We report, counter-intuitively, that placing the discrete (limiting) adhesive functionality on the particles versus on the wall profoundly influences particle capture from shear flow. We provide a quantitative explanation involving the hydrodynamically-driven rotation[161] of the functional particles in shear flow.

The findings identify a regime of materials design where synergy between surface chemistry the particle motion in a flow field may lead to new strategies for drug delivery, diagnostics, and self-healing systems, while providing further insight into cancer metastasis and the workings of the immune system.

2.3 Material and Methods

2.3.1 Materials

Poly-L-lysine hydrobromide (PLL), having nominal molecular weight of 15,000 -30,000 g/mol, was purchased from Sigma and used as received. Phosphate buffer with a pH of 7.4 (0.008 M Na_2HPO_4 and 0.002 M KH_2PO_4), having a Debye length of κ^{-1} = 2 nm was

employed in most studies unless otherwise noted. Variations in ionic strength, having different Debye lengths, were achieved either by diluting this buffer with deionized (DI) water or by adding buffer salts at the same ratio of Na_2HPO_4 and KH_2PO_4. In select control studies, rhodamine-tagged PLL was employed. The rhodamine labeling followed established procedures for fluorophore-isothiocyanate labeling of protein[162] and employed rhodamine B isothiocyanate from Sigma. Labeling was followed by dialysis to remove unreacted fluorophores and return the solution to the pH 7.4 phosphate buffer. The labeled polymer was lyophilized for storage and re-dissolved as needed.

2.3.2 Synthesis of Patchy Surfaces

Glass slides (Fisher Finest) were soaked in concentrated sulfuric acid overnight and rinsed with DI water. This procedure removes metal ions from the glass leaving a pure silica surface[163] with roughness less than a nanometer.[164] After rinsing, a slide was air dried and then sealed in the laminar slit flow chamber. The chamber was filled with phosphate buffer and used in deposition studies of functionalized particles, or further steps were taken to modify the silica surface itself.

To functionalize the silica wall with PLL, a 5 ppm solution of PLL in phosphate buffer was flowed through the chamber at a wall shear rate of 5 s^{-1} for a predetermined time. PLL chains adsorbed to the silica wall at the transport-limited rate, controlled by the PLL concentration and solution flow rate.[156] By replacing the flowing PLL solution with flowing buffer before the surface reached saturation (0.4 mg PLL/m^2)[156] , a controlled amount of PLL was deposited on the surface and free chains were removed from the bulk solution. The adsorption dynamics of the PLL chains were quantified separately in *in-situ* calibration runs using near-Brewster reflectometry as seen in Figure 3, having a resolution

of 0.01 mg/m^2.[156] This provided the error bars of about 5% reproducibility, down to 0.01m/m^2, in the reported amounts of the deposited PLL chains in particle studies. After PLL functionalization and rinsing the sealed chamber with flowing buffer for at least 10 minutes, deposition studies of unfunctionalized particles were initiated. The chamber was not opened between PLL functionalization and particle deposition measurements.

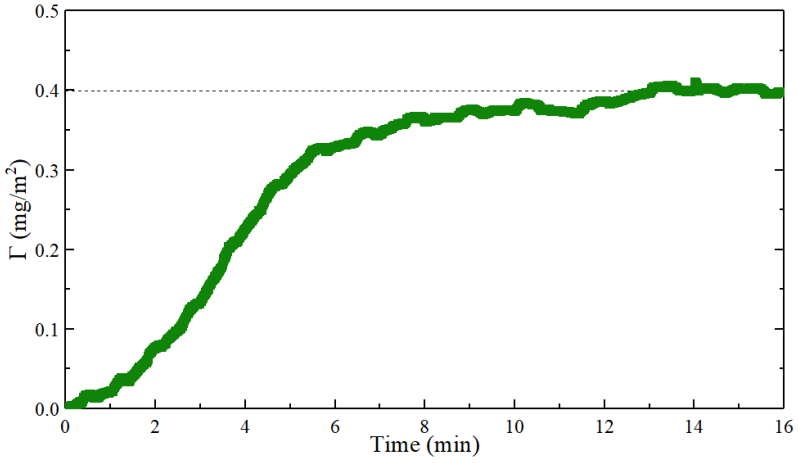

Figure 3. Near Brewster Angle Reflectometry calibration for PLL on a silica surface at shear rate of 5s^{-1}.

2.3.3 Synthesis of Patchy Particles

Monodisperse 1 μm silica microspheres (GelTech, Orlando FL) were used as received. PLL-functionalized particles were created by first dispersing 1μm silica particles in phosphate buffer having a concentration of 5.9 or 26 mmol, for studies to be conducted at Debye lengths of 4 and 2 nm respectively. At higher concentrations of buffer salts, the bare silica particles are more difficult to fully disperse and are more likely to aggregate because of van der Waals forces. At lower salt concentrations, the dispersion rapidly destabilizes and the particles aggregate with the addition of the oppositely charged polyelectrolyte.[20] PLL solution was added drop-wise, with stirring, to add the targeted amount of PLL chains to the particles. Adsorption occurred within tens of minutes though

suspensions were stirred for at least 4 hours to ensure complete adsorption and sonicated to ensure complete particle dispersion. For studies to conducted at a Debye length of 1 nm, where particles were less stable, preparation was done in 26 mmol buffer and, shortly before the flow study, concentrated buffer was added to bring the overall buffer concentration to 94 mmol. For studies conducted at a Debye length of 8 nm, functionalized microparticles were often unstable at the PLL loadings of interest. Preparation was therefore conducted in 5.9 mmol buffer and, shortly before the experiments, deionized water was added to bring the buffer concentration down to 1.5 mmol. As shown in Figure 4 it is important for experiments to occur at a time scale above the absorption time of the polyelectrolyte but below that of particle aggregation.

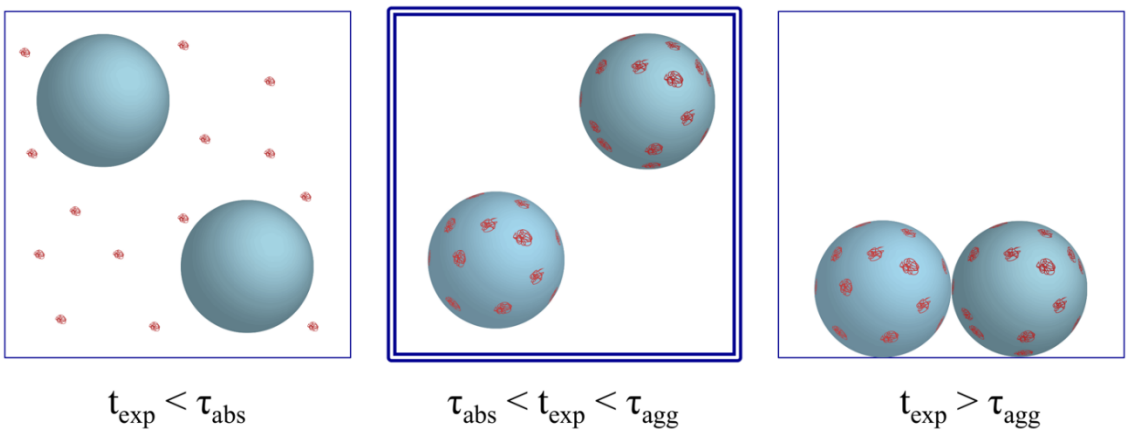

Figure 4. Schematic of synthesis of patchy particles. Experiments with patchy particles are performed in the window of time after the polyelectrolyte as absorbed onto the polymer before the particles have aggregated.

The necessary amount of PLL solution to add was determined by considering the targeted PLL loading and the area of the particles and the wetted glass container walls. (Polycation adsorption on silica and glass was estimated to be identical based on the chemical similarity and strong negative charge on both. This assumption was later confirmed using particle batches differing in overall particle concentrations.) Particles were prepared at

concentrations 250, 500, or 1000 ppm, so that the wall area was 5-20 % of the total, depending on the batch volume. Initial studies using 1000ppm microparticles were conducted at ionic conditions where suspensions were sufficiently stable over the ~10-minute time of a deposition study. However, to study the effect of ionic strength over a broader range, more dilute suspensions, 250 ppm, were employed to reduce the aggregation rate. Control studies with particle concentrations of 250 ppm, having greater proportions of wall area, produced the same particle capture efficiency observed at 1000ppm. This provided evidence that PLL adsorption onto the walls had been properly taken into account through the formulations. Additionally, considering the accuracy of our lab balances and solution handling techniques, we estimate a precision of 0.005 mg/m^2 in producing particles with targeted amounts of PLL.

2.3.4 Particle-Surface Interaction Studies

Particle capture studies were conducted in a custom-built microscope in which the test wall of the flow chamber was oriented perpendicular to the floor as seen in Figure 5. This eliminated gravitational contributions to normal particle-wall forces. A 20x objective provided a 260 x 178 μm field of view with 260 μm in the flow direction. A video camera recorded the particle capture dynamics at standard video capture rates. Particle adhesion studies were performed by flowing buffer of the desired ionic strength through the flow chamber at a wall shear rate of 22 s^{-1}, unless otherwise noted, followed by a suspension of microparticles in the same buffer and wall shear rate. Particle capture on the wall was recorded on video. Shear field in the chamber is controlled by the gasket size and pump settings. To ensure a uniform and known shear rate in the observation area, gaskets were sized so that the ratio between the width of the channel (between glass slide and

polycarbonate) and height of the channel is approximately 10, and the observation area is always near the middle of the channel.

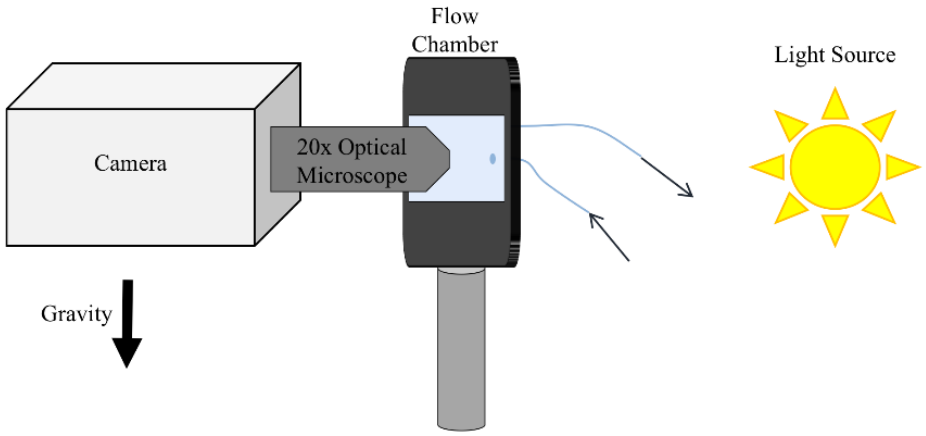

Figure 5. Schematic of laterally mounted flow cell system.

Video data of particle adhesion was fist exported into stacks of TIFF files using FFmpeg software. These image stacks were analyzed using manual tracking in *FIJI is just ImageJ*, or custom IDL tracking codes. Tracking manually allows only the fully arrested particles to be counted while automatic tracking also includes particles in focus near the surface but not adhered. The moving particles, however, serve as a fixed background that can be identified and subtracted.

Worth noting, because we could see the flowing particles in these studies, it was straightforward to avoid studies that were biased by particle aggregation and to eventually develop procedures that studied capture of single particles from suspensions that contained negligible aggregates.

2.4 Results

2.4.1 Characterization of Patchy Particles

Silica microparticles having targeted amounts of adsorbed PLL chains on their surfaces were created and employed in particle capture studies on silica flats. In most studies, the adsorbed amounts of PLL were substantially below the saturation coverage of 0.4 mg/m^2, though characterization and control runs employed particles having PLL loadings up to the saturation amount. The amount of PLL loaded onto particles (below saturation) was controlled by the amount of PLL added to the suspension, based on the fact that PLL adsorbs to silica surfaces rapidly (at the diffusion limited rate).[156] When the amount of PLL in solution is less than that needed to saturate the surface, all the PLL adsorbs to the silica particles and the glass container walls (which have been taken into account in formulations). The adsorption of nearly all PLL chains in a specimen, removing all measurable chains from the bulk solution, is a consequence of the strong polycation affinity for negative surfaces. For instance, with strong adsorption affinities, equilibrium free polymer volume fractions fall below 10^{-8}.[165,166]

2.4.1.1 Fluorescence Spectrometer Studies

A control experiment, employing fluorescent labeling to confirm the removal of all measurable PLL from free solution upon adsorption to silica microspheres, is shown in Figure 6. This validates the adsorption approach to produce PLL-functional particles with precise overall PLL loadings. Also worth noting, PLL adsorption is irreversible on the timescales of interest in particle capture experiments.[127] Additionally, polycations adsorbed on negative surfaces do not undergo measurable exchange with polycations in solution.[167,168] The complete retention of PLL on our particles was confirmed in studies

shown, where functionalized particles were rinsed and the washings analyzed for traces of removed PLL.

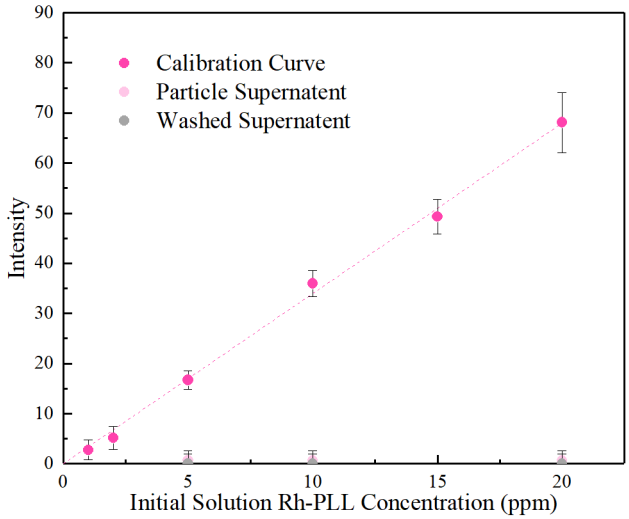

Figure 6. Fluorescence calibration curve for and points for the final supernatant concentrations for the formulations in Table 1.

Rhodamine-tagged PLL was employed in fluorescence studies designed to 1) confirm complete adsorption of PLL on particle and glass surfaces during particle preparation and 2) establish the complete retention of the PLL on the particles upon incubation in buffer and rinsing. These control experiments employed PerkinElmer Fluorescence Spectrometer, with excitation at 545 nm. Notably, the areas of the particles and the wetted glass walls of the containers were included in calculations determining how much PLL to add to a suspension to produce a targeted adsorbed amount of PLL adsorption.

Three separate preparations targeted Rh-PLL loadings on the microparticles, as described in Table 1. After the formulations were mixed, they were stirred in the dark for 4 hours and then centrifuged to remove the silica particles. The supernatants were then analyzed to determine their Rh-PLL contents, shown in Figure 6. The signal at a wavelength of 575 nm (corresponding to the measured peak in solutions of greater concentrations) was

compared to a calibration shown in Figure 6 and the supernatants from all formulations contained less than 0.9 ppm remaining in solution, the detectible limit.

Table 1. Summary of Formulations Studied

	Formulation A	Formulation B	Formulation C
Initial Rh-PLL Conc. (ppm)	20	10	5
Target PLL loading (mg/m2)	0.27	0.29	0.37
Target PLL Surface Coverage (%)	68%	73%	93%
Conc. Particles (mg/mL)	26.8	12.5	4.82
% of Surface Area on Particles	99.5%	99%	97%
Conc. PLL Remaining in supernatant (ppm)	Below Detectable Limit		
Conc. PLL in washed supernatant (ppm)	Below Detectable Limit		

To assess retention of Rh-PLL on the particles, the functionalized particles in the sediment were resuspended in 26 mmol buffer, stirred for 1 hour in the dark, and centrifuged again. Fluorescence measurements of the supernatants from this washing procedure are included in Figure 6. The fluorescence levels were below the detectible limits. With the 3.5 ml volume of the resuspension buffer similar to that of the initial formulation, we conclude that more than 99% of the Rh-PLL was retained on the functionalized particles upon exposure to buffer.

2.4.1.2 Fluorescence Microscope Studies

Figure 7 presents micrographs from two batches of microparticles with target loadings of rhodamine-PLL (Rh-PLL), 0.08 and 0.24 mg/m^2 as examples. While the micrographs, taken on dried specimens, should not be interpreted quantitatively in terms of fluorescence levels, it is clear that the fluorescent Rh-PLL resides with the particles and not in free

solution. The bar graph accompanying the images shows the light levels on the fluorescent channel for 200 individual (not aggregated) particles in each batch, measured from 10 different frames. The bar graphs show greater fluorescence in the batch containing the larger targeted Rh-PLL loading. Further, once the scattered light from the control particles (no Rh-PLL added) is subtracted, the fluorescence levels from the particles is roughly proportional to the targeted loadings. More importantly, the particles appear to be round in the fluorescence images, with relatively uniform fluorescence loading. The error bars on the bar graphs, which represent the standard deviation for 200 particles, are fairly narrow: this indicates good mixing during particle functionalization. We lack the problem of functionalizing some particles while leaving others unfunctionalized.

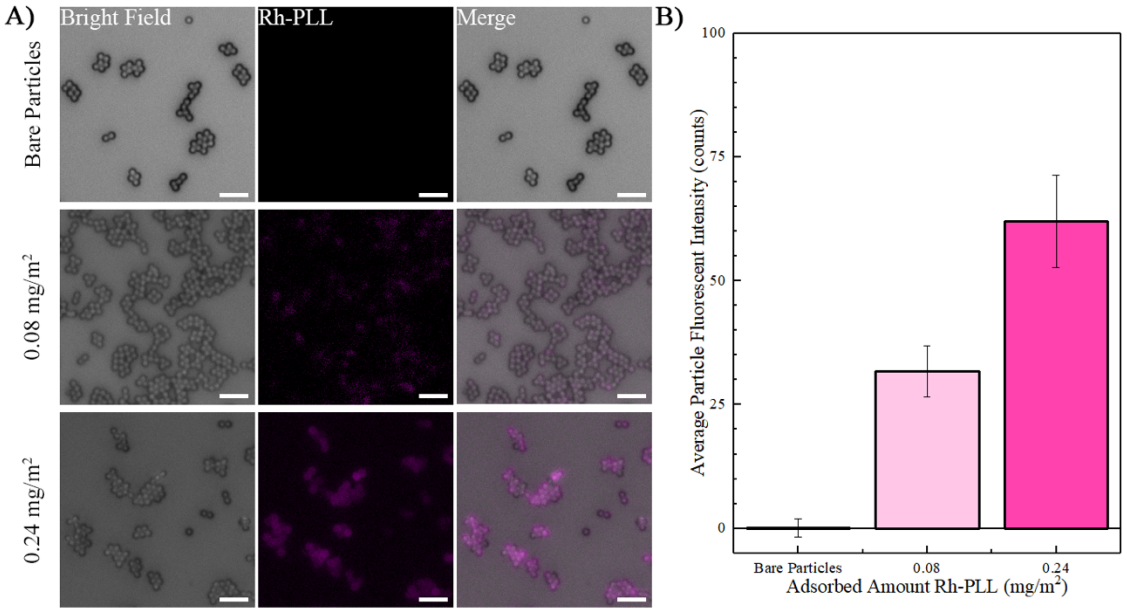

Figure 7. (A) Typical microscopic images of microparticles with different target loadings of Rhodamine-tagged PLL. Left panes are light microscopy. Middle panels are fluorescence. Right panels are combined. Scale bars are 5 microns. (B) Summary of particle fluorescence for different loadings of Rhodamine-PLL.

2.4.1.3 Zeta Potential Studies

The zeta potentials of particles with different loadings of PLL, in Figure 8, additionally support the quantitative PLL-functionalization of the microparticles. Here, in the limit of zero PLL loading, bare silica zeta potentials are in agreement with previously reported values.[169] Progressive addition of PLL, over a series of particle batches, produced incremental linear increases in the zeta potentials. Over the range of surface loadings relevant to interesting particle capture kinetics, below, from zero to about 0.25 mg/m^2, the zeta potentials are negative because the PLL coverage is relatively low. At a Debye length of κ^{-1} = 8 nm, the suspensions were unstable above PLL loadings of ~0.14 mg/m^2, so no zeta potential were reported above this level. More generally at other Debye lengths, for PLL amounts exceeding 0.4 mg/m^2, the zeta potential is positive and does not increase. This is because, when the added PLL exceeds that needed to saturate the particles, some PLL remains free in solution while the particles are saturated. Therefore, the same particles, with 0.4 mg/m^2 on their surface, are present in suspensions containing overall PLL concentrations corresponding to 0.5 and 0.6 mg/m^2, the PLL present when reported on a per particle area basis. The right-most data points correspond to suspensions of saturated particles and free PLL chains.

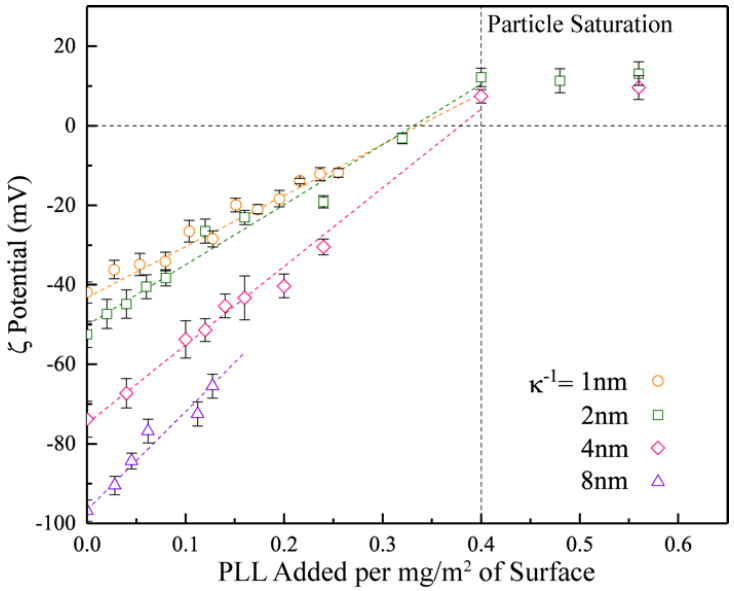

Figure 8. Zeta Potentials of silica microparticles with different amounts of PLL added. The x-axis indicates the amount of PLL present per unit of available surface area and the dashed vertical line indicates the saturation coverage of PLL on silica from previous measurements. Below the saturation coverage, the PLL is expected to adsorb to the particles. Above the saturation coverage, any additional PLL is expected to be free in solution.

The zeta potential plateau, in Figure 8 above PLL loadings of 0.4 mg/m^2, is an important observation in supporting the claim that the PLL loading is known precisely, ±0.005 mg/m^2 based on lab scale precision and fluid handling. The observed zeta potential plateau at 0.4 mg/m^2 PLL corresponds to the saturation coverage measured by reflectometry.[156] Therefore, Figure 8 shows that not only are we able to add PLL to silica microspheres in a linear and controllable fashion, the amount we aimed to add corresponds to that which actually is added, giving a plateau at the expected coverage. This observation, along with the tight error bars on the fluorescence per particle, argues for that our PLL functionalization of silica microspheres is quantitative.

Our combined results (microscopy, fluorescence spectrometry, zeta potential measurements) are quantitatively consistent with complete adsorption of PLL from

solution onto the silica microparticles (below the saturation coverage), forming the basis for the production of microparticles with controlled amounts of cationic patchiness. Fluorescence spectrometry argues against PLL remaining free in solution, while the lack of chain exchange for polycations in the literature[140] at these conditions argues against loss of PLL from particles during capture studies. This is consistent with the retention of PLL[156] and other polycations[106,170–172] on flats of opposite charge for relatively long times. Based on accuracy in preparing solutions and suspensions, we estimate a precision of 0.005 mg/m^2 PLL in the amount PLL adsorbed to the silica particles.

2.4.2 Flow Cell Studies

Each graph superposes multiple capture runs for different loadings of PLL on either the 1 μm silica particles or the silica wall. The data in Figure 9 show the particle accumulation as a function of time on the surfaces having the compositions indicated. Importantly, the accumulation increases linearly over the initial 10 minutes plotted for each run. This indicates that the particles already captured on each surface at a particular instant do not influence the capture of subsequent particles. As a result, the capture rates (the slopes of the data) are an indication of the interaction between the collecting surface and the individual particles, without complications from particle-particle interactions. This is observed experimentally (the accumulation is linear in time but the accumulation rate in the first 10 minutes of a given run is constant). This occurs because pseudo-steady state is achieved near the chamber wall. The concentration gradient of particles near the wall is fixed in time, giving rise to a fixed rate of particle accumulation on the wall. This occurs when the convection of particles to position L is matched with the diffusion across the boundary layer at that position, so that there is no concentration change (with respect to time) in the fluid near the surface. The pseudo-steady state condition fails initially when

the concentration gradient is being set up and also near surface saturation, when the gradient dissipates. It holds for substantial periods of time when adsorption / capture is occurring, and the surface is not saturated.

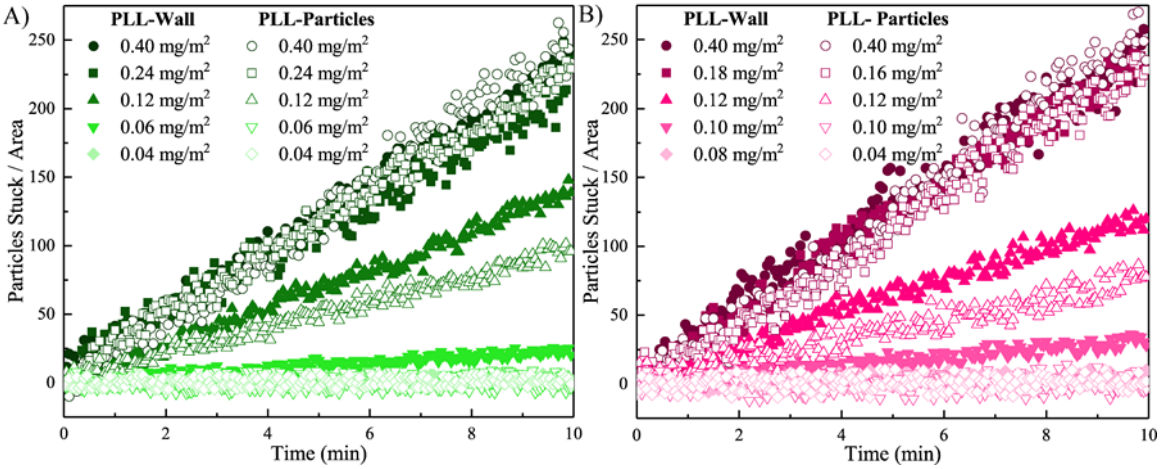

Figure 9. Example data for capture of silica particles on PLL-functionalized surfaces (solid symbols) compared with capture of PLL-functionalized particles on silica surfaces (hollow symbols). A) Runs conducted at κ^{-1} =2 nm. B) Runs conducted at κ^{-1} =4 nm. The PLL density on the particles or planar surfaces is varied as indicated.

The capture rates of the silica microparticles on saturated layers of PLL (0.4 mg/m^2) are observed to be transport-limited. The same rates are observed for fully PLL-coated microspheres on a bare silica wall. Flowing particles adhere on these sticky surfaces at a rate that matches their transport to the near-surface region. The quantitative form for this transport-limited adhesion on the wall of a shear flow chamber is described by the Leveque equation [100–102] (Equation 2.1).

$$\frac{dc_s}{dt} = \frac{1}{\Gamma\left(\frac{4}{3}\right) 9^{1/3}} \left(\frac{\gamma}{\mathcal{D}x}\right)^{1/3} \mathcal{D}c_{Bulk} \qquad (2.1)$$

In the transport-controlled limit, the particle accumulation rate, dc_s/dt, depends on the bulk solution particle concentration, C; the free solution diffusion coefficient, D; the wall shear

rate, γ; and x, the distance from the entrance of the flow chamber to the point of observation. On the right side of Equation 2.1 and only here, Γ is the gamma function.

The capture of flowing PLL-functionalized 1 μm silica particles on a silica wall is compared, in Figure 10, to the capture of flowing bare silica particles onto a silica wall functionalized with the same PLL. The wall shear rate is 22 s^{-1}. Variations in the PLL loading on the particles or the wall, on the x-axis, facilitate comparison of runs having the same amount of PLL on the particles or on the wall. The particle capture efficiency, on the y-axis, describes the measured particle accumulation rate normalized by the calculated diffusion-limited rate from Equation 2.1.

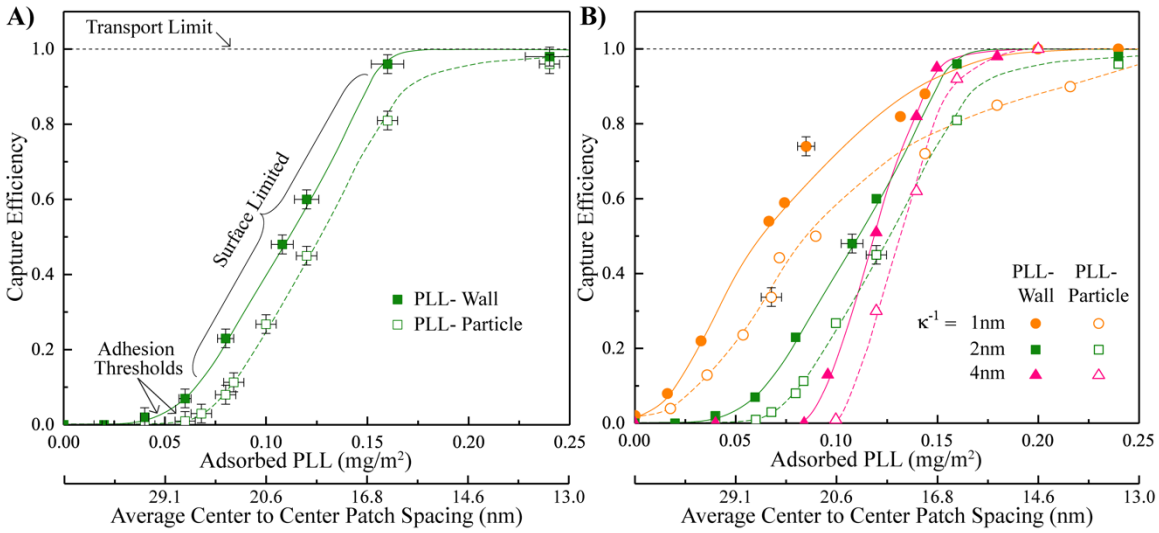

Figure 10. Capture efficiency of particles flowing at a wall shear rate of 22 s^{-1}. (A) Capture of functionalized particles is compared to capture on a functionalized wall for a Debye length of 2 nm. (B) Showing the impact of ionic strength for variations in Debye length from 1-4 nm.

Figure 10A, comparing runs for PLL placement on the particles or the wall, establishes the key observation that the capture of PLL-functional particles on a silica wall (hollow points) is always slower or equal to the capture of silica particles on the PLL- functionalized wall

(solid points), for the same loading of PLL on either the particles or the wall. Otherwise, the two sets of data share common qualitative features: 1) Both data series include the origin, indicating that, without PLL on either the particles or the wall, particles are not captured: This implicit control demonstrates that the immobilized cationic PLL chains provide the driving force for particle capture; 2) In Figure 10A both series of runs exhibit adhesion thresholds, a minimum amount of PLL required for particle capture. The adhesion threshold for the PLL-functionalized particles is greater than for a PLL-functionalized collecting surface; And 3) at high PLL loadings, the capture efficiency for PLL-functionalized particle or a PLL-functionalized wall approaches unity, as particles are captured at the transport-limited rate on the stickiest surfaces. It is in the surface limited regime, away from the transport-control, where the PLL placement on the particle or on the wall produces different rates in particle capture. Worth noting, in much of the surface-limited regime, the PLL functionalization is relatively sparse, less than 20% of saturation, and the zeta potentials are substantially negative, in Figure 8.

Motivated by the electrostatic nature of the particle-wall interactions, we considered the impact of ionic strength on particle capture. Figure 10B shows the slower capture of PLL-functionalized microparticles on a silica wall, compared with capture of silica microparticles on the PLL-functionalized wall, over a range of Debye lengths from 1-4 nm. Figure 10B illustrates that, although variations in Debye length shift the data, the essential features, from Figure 10A, are preserved. An interesting distinction occurs for κ^{-1} =1 nm: The adhesion threshold is substantially diminished and has almost vanished for the PLL-functionalized wall. Even so, greater PLL loadings are needed on the particles, compared with on the wall, to facilitate a given particle capture efficiency.

2.4.2.1 Low Ionic Strength Particle Accumulation Data

Particle aggregation for intermediate PLL loadings at a $\kappa^{-1} = 8$ nm prevented a full data set from being measured; however, capture was more efficient at these low salt conditions when the functionality was placed on the wall rather than the particles. For the capture of bare silica particles on PLL-functionalized walls, data was obtained over the full range of PLL loadings. However, for PLL-functionalized particles, we were unable to maintain dispersion stability long enough to conduct the experiments when the PLL loading on the particles was 0.14 mg/m^2 or more. This stability problem did not occur at the higher salt concentration. Because we were not able to obtain a complete data set and plotting the data was more complicated than in Figure 10, due to the additional annotation needed, these data are presented in Figure 11. Notably, for the full set of runs with the functionalized walls, there is a clear adhesion threshold and crossover to transport-limited particle capture on the functionalized wall. We were also able to identify a lower limit of 0.14 mg/m2 on the adhesion threshold for PLL-functionalized particles, also for inclusion in the state space diagram.

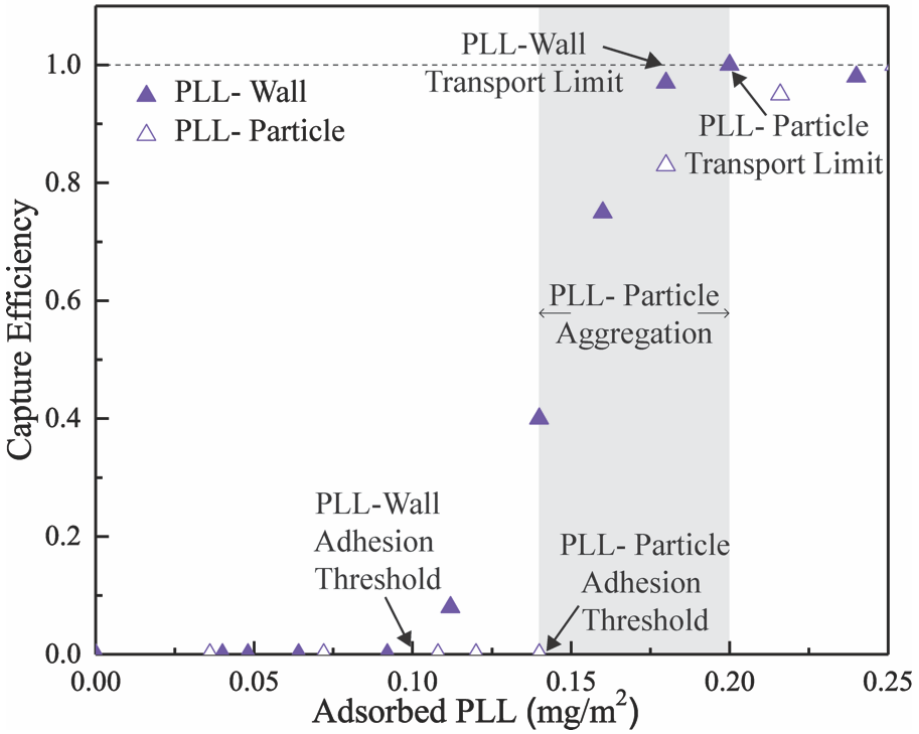

Figure 11. Particle capture efficiencies for PLL-functionalized walls or particles, as indicated, for a Debye length of $\kappa^{-1} = 8$ nm.

Looking closer at the zeta potential distribution in this lowest salt case (Debye length of 8 nm), we find that at low surface coverages (below 0.14 mg/m^2), the zeta potential distributions (Figure 12) consist of single uniform peaks indication that the polymer is adsorbing, and the particles are not aggregating. This agrees with our visual observations found in the flow cell data.

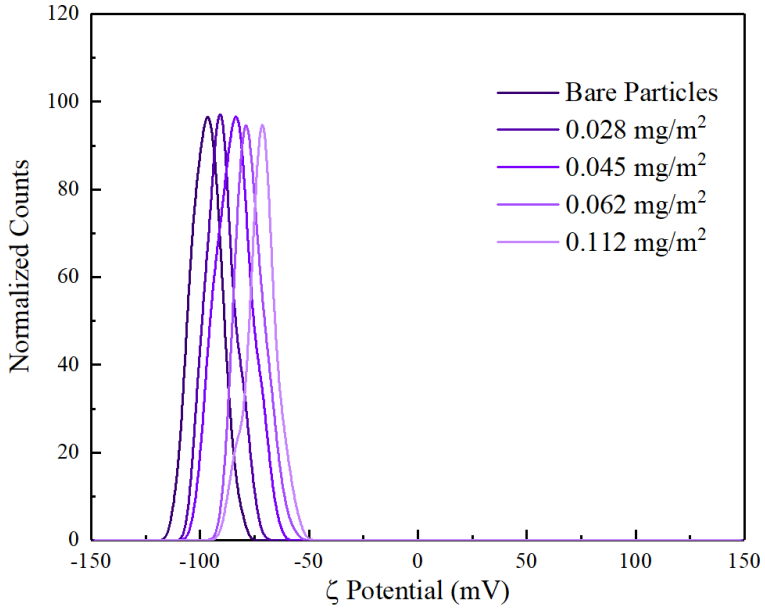

Figure 12. Zeta Potential distributions for functionalized particles in phosphate buffer having a Debye length of 8 nm.

2.4.2.2 Comparison Between Patchy Particle and Walls

Figure 13 summarizes the ratios of particle capture rates facilitated by PLL placement on the wall compared with on the particle, for variations in PLL loading and different ionic strengths. When particle capture occurs only above an adhesion threshold, the differences in the thresholds cause the ratio to diverge as a result of dividing by a zero rate for capture of PLL-functionalized particles. While the presence of adhesion thresholds causes the ratios of capture efficiencies Figure 13 to diverge, there is a maximum in the ratio for the data at κ^{-1}= 1 nm. This maximum ratio is approximately 2 at these ionic conditions.

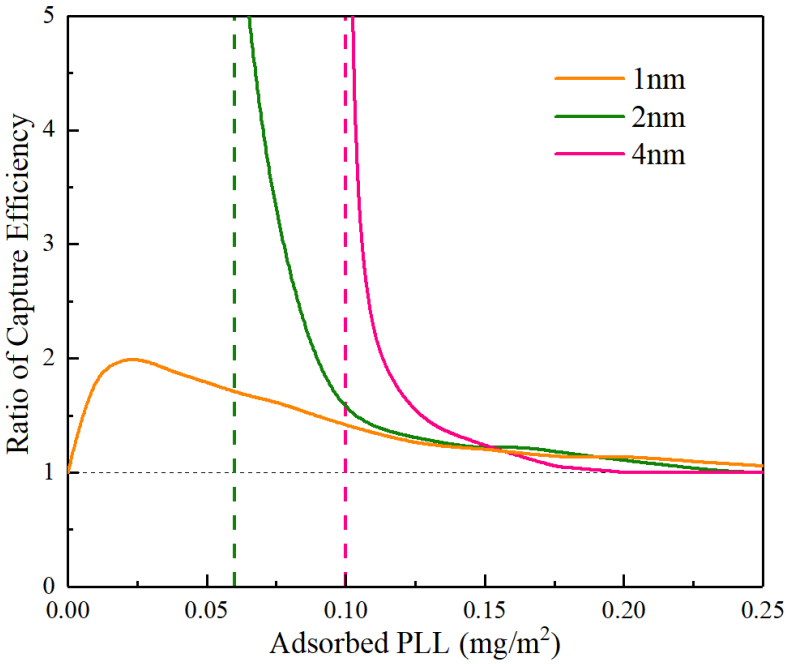

Figure 13. Ratio of capture efficiencies for functionalized walls, normalized by that for functionalized particles with the same amount of functionalization, from the data in Figure 10.

The ratio of PLL needed to obtain a given capture efficiency is shown in Figure 14. At shear rate of 22 s^{-1}, the functionalized particles always require more PLL than the functionalized surfaces. At higher salt concentrations and lower capture efficiencies, this ratio is higher.

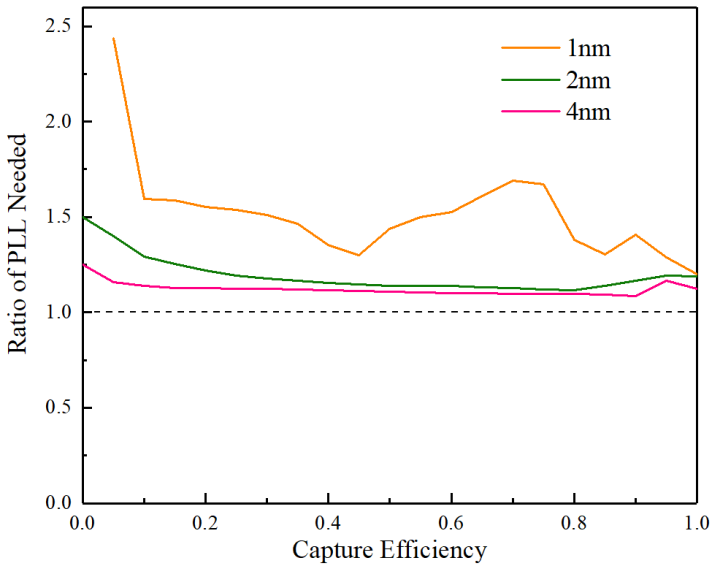

Figure 14. Ratio of PLL needed on the surface of functionalized particles normalized by the amount of PLL needed to give the same capture efficiency on a functionalized wall. Determined from the data given in Figure 10.

2.4.2.3 Effect of Flow Rate

Figure 15 illustrates the complicated influence of wall shear rate on particle capture. Because the transport-limited rate itself varies with wall shear, we present, in part A, the particle capture rates (not normalized by the transport limited rates) and in part B, the capture efficiencies, which more nearly collapse the data sets vertically as a result of normalizing on transport limited rates.

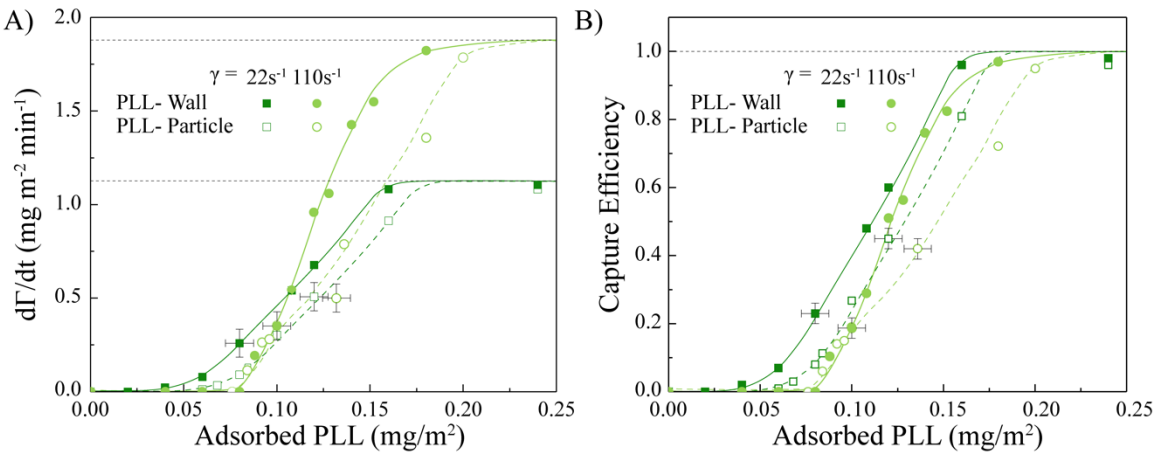

Figure 15. Influence of wall shear rate, 22 or 110 s^{-1} on the capture of flowing functionalized particles or with the wall bearing the adhesive functionality. (A) The capture rates for suspensions containing 250 ppm particles. Dashed lines represented the transport-limited rates for the two flow rates. (B) Data represented as capture efficiencies.

The data confirm the expectations that greater amounts of PLL are required to trap moving particles and overcome hydrodynamic forces. Also seen is that increases in wall shear reduce the difference in particle capture efficiencies corresponding to PLL functionalization on the particles versus the collecting wall. The ratios of the capture efficiencies for trapping of unmodified particles on a PLL-containing wall relative to PLL-modified particles on an unmodified wall are shown in Figure 16A. When comparing the amount of PLL needed to achieve a given capture efficiency (Figure 16B), the higher shear rate eliminates the advantage of functionalization of the wall at lower capture efficiencies, but at higher capture efficiencies, a difference in required polymer loading is still seen.

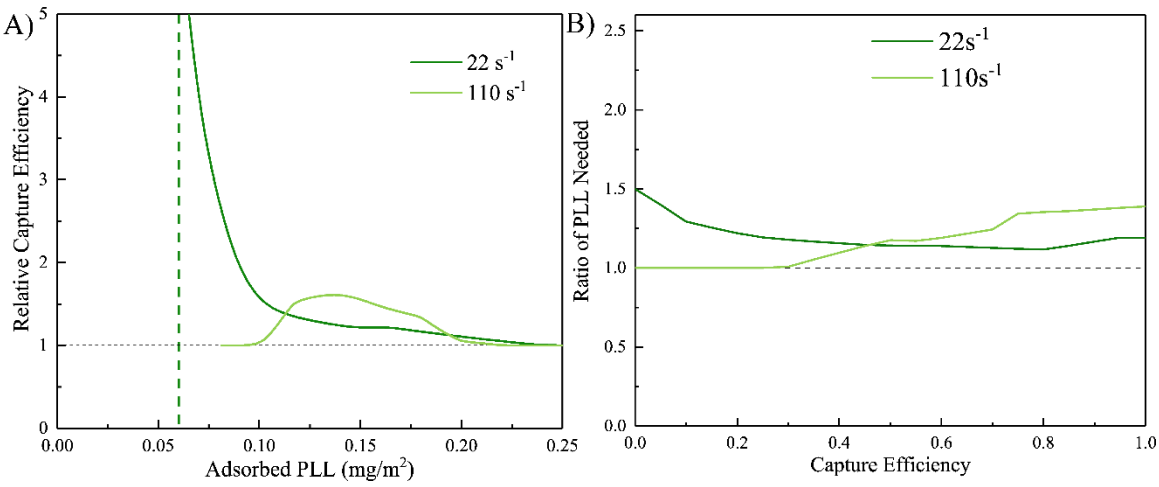

Figure 16. (A) Ratio of capture efficiencies, with the efficiency on the functionalized wall normalized by that on the functionalized particles. (B) Ratio of PLL needed on functionalized particles normalized by the amount needed on a functionalized surface.

2.4.2.4 State Space Map

Figure 17 summarizes the regimes of particle capture in terms of surface compositions, ionic strength, and factors controlling capture. This state space map includes the data from Figure 10 in addition to limited measurements from Figure 11 at low or very high PLL loadings at κ^{-1} = 8 nm that allow boundaries in Figure 17 to extend to low ionic strengths. The state space map facilitates the design of surfaces or particles that either 1) do not adhere to surfaces because their functionality is below the adhesion threshold, 2) adhere to the wall at a rate controlled by the loading of cationic PLL on the particles or wall, and 3) are captured at the transport-limited rate. This representation is useful because the boundaries can be compared with scaling theories and modeling efforts, capturing essential crossover physics. The differences resulting from functionalization of the wall versus the particle occur in the middle (white) section of state space.

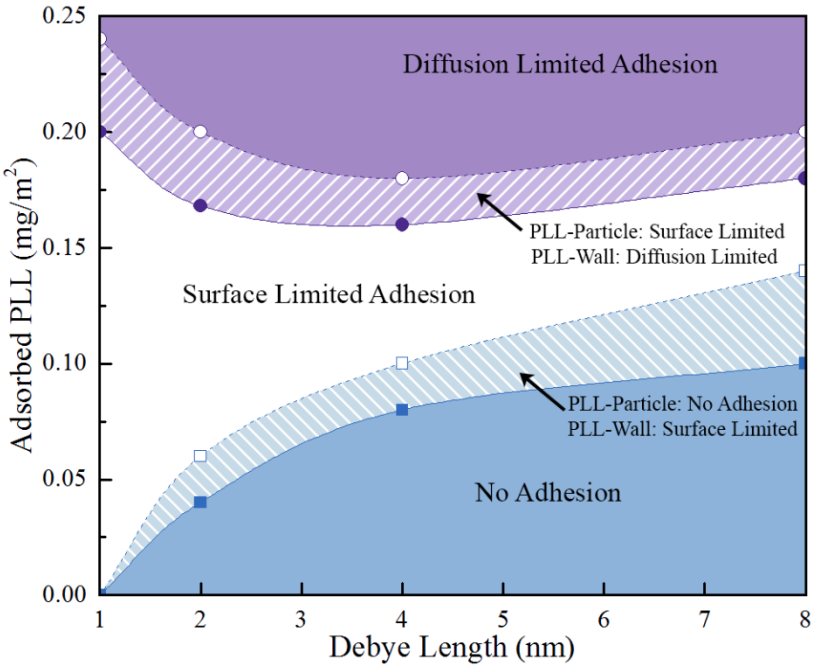

Figure 17. State Space Maps for the regimes of particle capture behavior when the particles or the wall are functionalized. The boundaries between "no adhesion" and surface-limited adhesion represent the locus of adhesion thresholds for PLL-functionalized particles or wall.

2.5 Discussion

Figure 10 - Figure 17 demonstrate that, in the regime of finite surface-controlled particle capture, more efficient capture was achieved by functionalizing the collecting wall rather than the particles with the same amount of PLL. The difference in capture rates was significant, often greater than a factor of two, when the wall shear rate was moderate, in the range of 20 s^{-1}. Less efficient capture of PLL-functionalized particles, compared with a functionalized wall, was observed for a broad range of PLL loadings and the full range of ionic strengths and Debye lengths studied. We were unable to find conditions leading to more efficient capture of functionalized particles compared with a functionalized wall for the same functionalization density.

The significance and generalizability of these findings is borne out through a recapitulation of the system's distinguishing material features. First, it is the surface-immobilized PLL chains that drive particle capture. Without PLL on the particles or the wall, particles flow past. (The exception, for κ^{-1} = 1 nm, is a very low level of particle capture which occurs more quickly above a small threshold in the amount of PLL added to the particles or the wall.) Further, the amount of immobilized PLL is rate-limiting for particle capture in the conditions of interest. (Studies with both particles and wall functionalized are beyond the current scope.) The adsorbed PLL chains constitute randomly distributed nanoscopic cationic patches, each of which is attracted to any region of an opposing bare silica object. At the conditions of interest, the PLL chains are relatively isolated[31] and act as individual weak stickers.[106] Thus the PLL-functionalized surface, either the particles or the wall is rate limiting, while the other surface acts, effectively, in excess. (Recall that the adsorbed PLL chains also are immobile and lie relatively flat to the surface,[156] as expected for polyelectrolytes adsorbing sparsely on surfaces of opposite charge).[158,166,167,173] The weak per-PLL attractions produce adhesion thresholds, since a particle must be trapped by the simultaneous influence of several PLL chains.[106,122]

While surface charge dominates the interactions of the current microparticles, the system serves a model for adhesive control by surfaces carrying relatively sparse discrete functionality (here the surface carrying the PLL) interacting with opposing surfaces that are abundant in complimentary adhesive functionality (here the uniformly negative silica surfaces). Such a scenario can occur with engineered particles for targeted selective delivery, or for engineered collecting surfaces, for instance, in microfluidic diagnostics. The key material feature in this study is that, with an abundance of negative charge on bare

silica, the PLL functionalization on the complimentary surface controls the particle capture rates. This is seen in Figure 10 and Figure 15 where the capture efficiencies are dependent on PLL loading of either the particles or the wall, on the x-axis.

The adhesion threshold features in Figure 10 and Figure 15 is a behavior seen for the capture of flowing microparticles on walls that were fundamentally repulsive towards the particles but which were functionalized with low levels of discrete adhesive functionality including acrylic polycations or nanoparticles.[122,157] The observation of the adhesion threshold in this work with PLL as the polycation is therefore expected. The threshold results from the weak attraction between individual polycationic species and the flowing particles, with a single polycation insufficient to capture a flowing particle. When the PLL loading on the wall is sufficient that particles encounter multiple PLL chains at once, then particles may be captured, producing the threshold. In this way the adhesion threshold results from a requisite multivalency in the species responsible for the capture.[158] Relevant here is that similar thresholds occur with the wall or the particles are independently PLL-functionalized.

2.5.1 Why Does PLL Placement Matter?

Surface forces must be included in an explanation for the different capture efficiencies seen in systems having either a PLL-functionalized wall or PLL-functionalized particles. Figure 18 illustrates the particle-wall gap region for the two scenarios, focusing on the area on the two surfaces that are within range of electrostatic interactions, the "zone of influence".[106,122] This circular area on either surface has a radius $R_{zoi} \sim (\kappa^{-1}a)^{1/2}$. Simulations and theory demonstrate that 99% of electrostatic interactions arise from the surface regions within the zone of influence.[121,159]

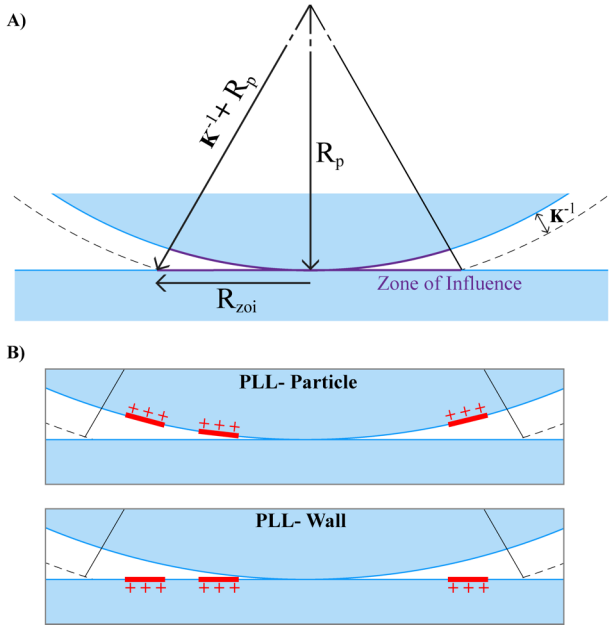

Figure 18. A) Definition of the zone of influence. B) Close-up schematic of the gap between a silica particle and a flat wall, showing equivalent positions of surface patches on the particle or the wall.

For the a given randomly-distributed PLL pattern on either the particle or the wall, an equivalent pattern of PLL placement can be imagined on the opposing surface, shown conceptually in Figure 18. Because the electrostatic interactions depend on the particle-wall distances, the net interaction cannot depend on whether the curved or flat side of the gap carries the adhesive pattern. Thus, it follows that placement of functionality on the curved or flat surface should make no difference to the interactions. This interchangeability is the basis for theory and experiments in colloid science including the use of crossed cylinders as equivalent to sphere-sphere or sphere plate interactions.[41] The Derjaguin approximation[6] and more precise integration methods[118,159,160] are also quantitatively consistent with this interchangeability.

In this work we have worked to develop a symmetric system, where the silica spheres are chemically matched by the silica wall, and where both are as smooth as one can practically achieve. However, even with some differences in silica chemistry or roughness between the sphere and the wall, Figure 18 argues that the interaction between a PLL-functionalized sphere with a bare wall should be equivalent to that between a plain sphere and a PLL-functionalized wall. The bare silica interactions across the gaps in the two scenarios are identical and, further, the nature of an adsorbed patch on one surface or other should be very nearly similar. Indeed, the saturated coverage of PLL on the wall, measured by reflectometry is similar to the beginning of the zeta potential plateau for the adsorption of PLL on silica spheres in Figure 8.

Therefore, in experiments where the PLL loading is the same on one or other surface and its distribution is random, the principles of colloidal science predict that the surface forces in the two systems should be equivalent. Thus, the observations in the Figure 10 - Figure 17 are not explained by surface forces alone.

2.5.2 Particle Motion

With sufficient particle-wall attractions, found to be the case for PLL loadings exceeding ~0.15 mg/m^2 on either the particles or the wall, particles adhere to the wall at the diffusion-limited rate, for instance, described by the Leveque equation.[105,106] Diffusion controls particle capture in this way even though the Peclet number, $\frac{6\pi\eta a^3\gamma}{kT}$, is order unity throughout this study.

When particle capture is limited, not by diffusion, but by the interaction of relatively sparse surface features, particles near a surface (within reach of electrostatic interactions) are not immediately captured. The rate at which a particle encounters a sticky region of a functionalized wall differs from the rate at which functional particles turn over and expose a sticky region to the wall. Thus, placement of the functionality on the wall or the particles produces different capture rates and efficiencies.

Near-wall particles flow along the wall for some time, until they diffuse away or are captured.[121,122,159] During this movement, the PLL-functionalized surface is sampled by the opposing uniform silica surface.[118,159,174] At each instant in time, a surface region no larger than radius R_{zoi} interacts and, as the particle moves, R_{zoi} shifts to different material points on the PLL-functional surface. Not all regions of size R_{zoi} on the PLL-functionalized surface can be adhesive when PLL chains are distributed randomly and sparsely.[159] This is especially true in the surface-dominated kinetic regime: Some regions of the surface will produce net repulsions while other may produce net attractions, causing the particle to fluctuate in height as it flows.[118,159,174] Capture occurs only once a sufficiently adhesive region on the PLL-functionalized surface, or "hot spot", is encountered.[122,159] Height fluctuations during particle flow and particle capture on "hot spots" (surface regions of size R_{zoi} having statistically high numbers of cationic chains) are behaviors established in simulations for uniform negative particles flowing over a wall presenting random nanoscopic cationic patches in the concentration range on the walls in Figure 10.[122,159]

The probability of a bare flowing particle encountering a "hot spot" on a PLL-functionalized wall should be proportional to the particle's translational velocity. Faster

moving particles cover more wall surface in the period that they reside near the wall. (This is a diffusion time.) Likewise, particle rotations expose new material points on the particle's surface towards the wall, at a velocity $V_r = R\Omega$, where Ω is the rate of particle rotation. Thus, the probability that the bare wall encounters a hot spot on a rotating PLL-functionalized particle is proportional on the particle's rotational velocity. In shear, particles both translate and rotate. For a microparticle within nanometers of the wall, the translational velocity is about twice rotational velocity, with only a slight dependence on particle-wall separation.[161] Thus, a PLL-functionalized wall is "scanned by a bare particle at about two times the rate that, in a separate experiment, a PLL-functionalized particle is scanned by the wall. For identical patterns of PLL functionality on the wall or the particle (in Figure 18), an adhesive region of the PLL will be encountered sooner when it is placed on the wall. The same features on the particle will take longer to reach the zone of influence through particle rotations. This effect will cause particles to be captured, in shear flow, more quickly on a functional wall than through placement of functionality on the particles.

A factor of two difference in capture rates is approached in experiments at $\kappa^{-1} = 1$ nm. The presence of adhesion thresholds at higher Debye lengths produces an even greater difference between systems in which the particles or the wall containing the limiting adhesive functionality. Potentially complicating the description of particle-surface interactions is the height dependence of the electrostatic interactions: the zone of influence decreases with increased particle-surface separation.[159] When particle capture depends on adhesive encounters of sparsely populated surfaces, however, the sampling rate of the functionalized surface is apparently the dominant effect.

2.5.3 Influence of Flow

Increases in flow produced complicated behavior, a result of competing effects. The transport-limited rate of particle capture, at high PLL loadings on the particle or wall increased as would be expected, in Figure 15A. At the same time, increases in flow were seen, in Figure 15B, to reduce the difference between particle capture rates driven by functionalization of the particles versus the wall. This, however, was a smaller effect than the impact of flow on the adhesion thresholds. With increases of flow, the particle capture became more difficult, requiring greater PLL loadings overall. Both observations are best understood in the context of the particle fluctuations that are driven by attractions and repulsions when near-surface particles experience different numbers of PLL chains within the zone of influence. Simulations by Duffadar and Davis, and later by Bendersky, demonstrated that these fluctuations are suppressed with increased flow, making particle capture more difficult and diminishing the effective impact of wall or particle heterogeneities.[121,174]

2.5.4 Ruling Out Alternative Mechanisms

We considered other potential reasons for the differences observed for placement of polycations on the particles or the wall. First was the possibility that the particles were less densely functionalized than reported. Our control studies, however, establish that this is not the case. Fluorescent labeling experiments, described earlier, demonstrated that, for the fabrication of particles containing less than saturated levels (0.4 mg/m^2) of PLL, all the detectible PLL was adsorbed from solution well-within the processing period of less than 4 hours and that the PLL was retained on the particles after dilution in buffer. By taking wall area into account in formulations, we were able to obtain the same particle capture rates when particle batches were formulated at 250 ppm or 1000 ppm. This provided

confidence in our ability to produce particles with targeted PLL loadings and confirmed the quantitative reporting of PLL coverage. Finally, the zeta potentials of the functionalized particles increased, with incremental PLL functionalization, as expected, in Figure 8, in further agreement with the reported levels of PLL functionalization. The leveling off-of the zeta potential at PLL amounts corresponding to 0.4 mg/m^2 in Figure 8 was consistent with the 0.4 mg/m^2 plateau coverages measured by reflectometry on the chamber wall.[156] This served as an independent check of our ability to quantitatively load target amounts of PLL onto the particles or wall.

A second potential source of artifacts in these studies is the possibility of non-uniform PLL distribution among the different particles in a sample. While it is not clear that this potential problem would explain results such as a higher adhesion threshold for the PLL-functionalized particles compared with a PLL-functionalized wall in Figure 10, procedures targeted a uniformly random distribution of PLL among the particles in a sample. For instance, the PLL solution was added incrementally to the particle suspension to avoid producing a particle population with a high PLL loading. Confirming a single population of functionalized particles rather than subpopulations with high and low charge, zeta potential characterization produced single peaks.

Finally, we considered the possibility that a random distribution of PLL chains adsorbed on the surfaces of microparticles, which is what we aimed to achieve, could itself be responsible for our observations. A random distribution of adsorbed species (following a Gaussian or Poisson distribution) will always produce some particles having more chains and some particles having fewer chains than the average. Thus, some particles will be less

adhesive than others. This effect, for a truly random distribution, turns out to be small: For instance, we considered a PLL loading of 0.06 mg/m^2 corresponds to an average 5650 chains per 1 μm diameter particle. (This PLL loading was observed at the adhesion threshold for PLL-containing particles in a buffer having a 2 nm Debye length.) If a random distribution is achieved, then ~1% of particles will have 5490 or fewer chains per particle. Far fewer than 1% of the particles will, in a Gaussian distribution, have greater deviations from the average (reported) PLL loadings. Thus, a random distribution of chains on the particles produces very minor differences (less than a percent) in the numbers of chains per particle and cannot produce particle subpopulations which might explain the observations.

2.5.5 Significance

The findings reported here, summarized in the form of state space diagrams, form an initial basis for the design of targeted particles whose adhesion could be tuned through rotations driven by hydrodynamics or other fields. Such effects could form the basis for targeted delivery packages whose adhesion is controlled not only by surface features but also by the flow environment. Understanding the role of particle rotations in their capture by discrete adhesive moieties may also aid in the design of devices that capture and manipulate rare cancer cells or specialized immune cells.

2.6 Conclusions

We presented engineered particles whose capture was controlled by their sparse surface features, producing adhesive capture that was substantially slower than particle capture by the same level of functionalization of an adhesive wall. The more efficient capture for the

PLL functionalized wall occurred over a broad range of PLL surface loadings and ionic strengths at moderate shear rates, here near 20 s^{-1}.

The observed differences in particle capture were attributed to particle motions in shearing flow. When flowing microparticles are within a few nanometers of a wall, sufficient for surface interactions, their rotational velocity, driven by the vorticity of the shearing flow, is about half that of their translational velocity. As a result, new material points on a particle's surface rotate into interactive range of the wall at about half the rate that new material points on a wall translate within range of the particle. This distinction becomes important when particle capture occurs through the engagement of sparse features on one or the other surface. Then, particle movement can determine the rate at which adhesive regions on the functionalized surface have the opportunity to interact. In shearing flow in our systems, the PLL-functionalized wall was sampled by silica particles at about half the rate that PLL-functionalized particles were effectively sampled by the bare wall.

The functionalized particles in this study, with their rate-limiting discrete adhesive features, comprise a model system in which hydrodynamic and surface design considerations can be tuned for precise control of capture and adhesion. The current study employed electrostatically attractive surface features, enabling the strength and range of the attractions to be tuned through ionic strength. The observed rotation-control of particle adhesion, over a range of salt concentrations, demonstrates that the influence of rotation is not limited to a narrow range of adhesive strengths. Our best proposed explanation for the reduction of the effect at higher flow rates was the suppression of fluctuations driven by spatially varying electrostatic interactions.

CHAPTER 3

SWIMMING BEHAVIOR OF BACTERIA INCREASES NUMBER AND DURATION OF BACTERIAL-SURFACE ENGAGEMENTS

3.1 Introduction

Because motility is associated with bacterial pathogenesis,[175] there is general interest in studying the interactions of swimming bacteria with biomaterial surfaces. *E. coli*, a bacterial type associated with disease[176–178] and biomaterial infections,[179,180] includes motile phenotypes that swim using a bundle of several flagella. With flagella bundled, bacteria travel in nearly straight trajectories; however, occasionally when one or more flagella motors reverse, unbundling of flagella interrupts this straight swimming, resulting in a redirection termed "tumbling" that facilitates chemotaxis. [181,182] During straight swimming, cell motion is described as pushing, and a hydrodynamic force dipole pushes out at the front and back of the cell while a hydrodynamic inward force occurs along its sides. These hydrodynamic interactions are considered long range, for instance having interactions with a surface that scale as $1/h^3$ where h is the separation distance between the bacteria and the surface.[63,76] *E. coli* are classified as "pushers," as are many other important types of bacteria.[63,183,184] *Bacullus subtilis,* with dimensions (4-10 μm in length and 0.25-1 μm in diameter) slightly larger than *E. coli* (2 μm in length and 0.5 μm in diameter) represents another important model bacteria exhibiting pushing behavior. Seminal studies employing model strains of both *E. coli* and *B. subtilis* have established swimming behaviors potentially relevant to the biomaterial interactions studied here.

Run and tumble bacteria chemotax, that is swim progressively towards surfaces that produce gradients of dissolved nutrients in solution.[72] In the absence of chemical gradients and even for straight swimming pusher strains, there is the perception that bacteria swim towards surfaces in quiescent solution due to very long-range hydrodynamic attractions. In fact, bacteria in quiescent suspension swim in all directions. When a cell happens to encounter a surface, hydrodynamic repulsions (pushing) at the front of the cell cause it to rotate during a surface encounter, allowing a long-range hydrodynamic attraction between the sides of the cell and the surface to retain the cell in the vicinity of a surface. A result of these interactions, non-tumbling *E. coli* cells have been shown to be concentrated by about a factor of 5, in a region 10-20 μm from the rigid walls bounding fluid gaps that are 100 or 200 μm deep.[76] Also for *Caulobacter crescentus*, cell-surface collisions and subsequent hydrodynamic attractions are reported to produce elevated cell concentrations in sub-micron near-surface region while the cell concentration approach that of the bulk suspension by 10 μm from the surface.[185] The near-surface cells exhibit further interesting behaviors such as swimming in circles as a result of torque from the flagella bundle.[75] Confined bacteria, such as those in quiescent microfluidic channels selectively swim along one wall as a result of the same chiral flagellar action,[186] though the potential to interact with multiple walls through long range hydrodynamic interactions is complex. These types of long range hydrodynamic interactions are not unique to microbial swimmers, the wall accumulation behavior has also been seen for synthetic particle swimmers indicating that it is a functionality of motility and not just of microrganisms.[187]

While most studies of swimming bacteria have been conducted in quiescent conditions, the coupling of swimming dynamics with a flow field reveals further fascinating complexities.

For instance in Poiselle flow, a depletion region is reported for both wild type and smooth swimming *B. subtilis*, and wild type *P. aeuginosa* as a result of "trapping" of pusher cells in regions of greater shear.[83] For the appropriate geometries and ranges of flow rates, this effect can reduce the cell concentration at the center of a channel by as much as 30% relative to the situation without flow.[83] Notably, this effect concentrates cells in regions more near the walls than the center of the chamber but is not a wall effect. It would occur in the absence of hydrodynamic attractions to the wall. Instead, coupling of swimming hydrodynamics and flow traps cells away from the centerline where the shear rate vanishes, in favor of the sharper velocity gradients. The extent to which this effect increases wall collisions and physical interactions between cells and surfaces is not known. Also interesting, cells oriented by shear gradients can swim against the flow; however the extent to which this produces net cell travel against the flow direction depends on the flow conditions.[82,84] Indeed, in high shear, retention of *E. coli* in corners and sidewalls of channels produces clear upstream migration of cells.[85]

The growing literature on the interactions of swimming bacteria with surfaces however, has now uncovered the basic aspects of cell-surface hydrodynamic interactions; the connection of these behaviors to those of biomaterial interactions, for instance relevant to biofilm formation, is an important open area. For instance, it is evident in models of steady state cell concentration profiles,[76,185] that the residence of time near-surface cells is finite as cells move about. While cells are observed to leave the near- wall region,[76,80,185] the steady state fluxes and other dynamic features such as effective cell-surface residence times of these systems are not yet quantified. Near surface residence time at the level of individual cells is, for instance critical, because the opportunity for adhesion events

increases with residence and because the restriction of flagellar motion is known to trigger cell-level changes that facilitate biofilm formation.[188]

The study in this chapter aims to reveal the fundamental interactions between a swimming bacterium and a single wall in flow, using a large chamber in which the bacteria are unconfined, in sharp contrast with current studies which take place either in confined environments or with little to no imposed flow.[82,83,189,190] In the studies that do impose flow, the majority are performed in confined channels and moderate shear rates that allow for the geometric properties of the channel to dominate the interactions.[85] This chapter reports a study of the impact of swimming motility and the presence of flagella on the dynamic interactions between a bacterium and a non-adhering surface in shear flow. Non-adhering is defined to mean that bacteria are not captured and retained. In contrast with studies reporting directional swimming in microfluidic channels, the fundamental question of hydrodynamic and biomaterial interactions are probed here at a single surface (bounding a thick 0.7 mm flow chamber).

To fully explore this issue, we compared the behavior of *E. coli* cells of a parent strain to three genetically modified phenotypes: “Super Swimmers” or bacteria that have extra flagella and are able to swim faster than their parent strain; a version of the Super Swimmers engineered to have non-functioning flagella termed “No Motors”; and bacteria with no flagella termed “No Flagella”. Within these four types of bacteria studied there are two classifications of bacteria: active swimmers and diffusers. As illustrated in the schematic of Figure 19 the Super Swimmers exhibit their own independent motion towards and along the surface. By contrast, the diffusers rely only on diffusive transport

mechanisms. This study compares the differences in interactions between these types of bacteria and a non-adhesive PEG surface.

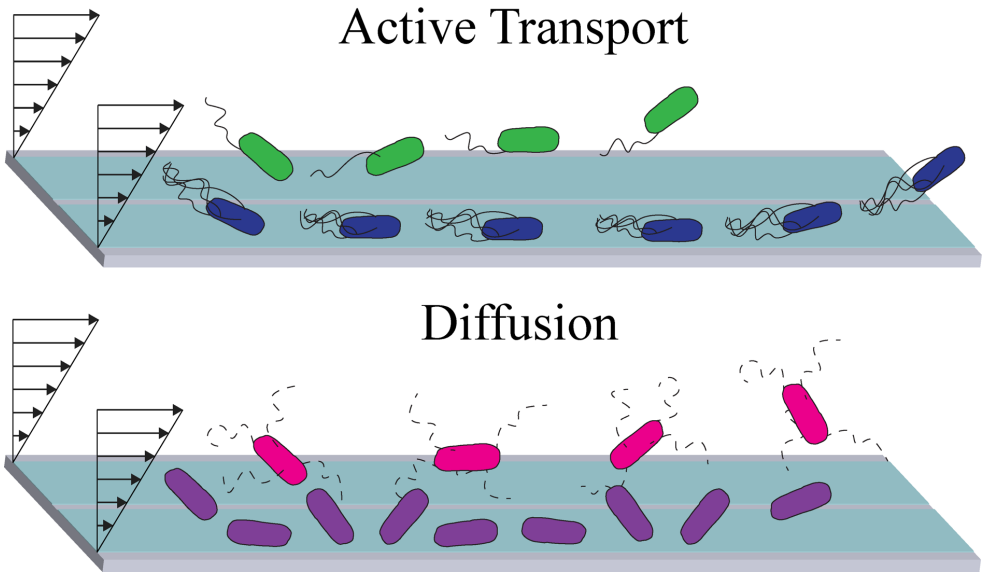

Figure 19. Schematic of different types of bacteria-surface engagements, A) Active transport along surface by Parent Strain (green) and Super Swimmer (Blue). B) Diffusive engagements by non-motile "No Motor" (magenta) and "No Flagella" (purple).

By laterally mounting the chamber, bacterial-surface interactions were studied without the influence of gravity, providing a model system more similar to what would be found in nature. The flowing system also allows for surface interactions to be studied on a much faster time scale (smaller contact time) then possible with time-dependent settling studies.[191] A potential mechanism in *E. coli* for this rapid type of catch-release bond is the Fim-H that forms pili on the surface of *E. coli*.[192] These types of bonds have been shown to be sensitive to shear rate.[193,194]

3.1.1 Effect of Motility

In both bacteria and synthetic particles, motility has a large impact on how a colloid or a living colloid behaves. Work on synthetic particle systems has shown that particles that can swim initially exhibit random walk type motion and collision but then begin to aggregate and form 'living crystals.' These ordered regions can break apart and reform, and if the swimming ability of the synthetic particles is turned off, the 'living crystals' break up and return to random walk and diffusion behavior.[60,195] This motility-induced phase separation is believed to be caused by a pressure difference due to the swimming.[196] This behavior also causes particles to swim towards the wall of their container.[187,197] This phenomenon of active colloids swimming towards the walls and forming aggregates is also seen in bacteria systems.[185] In flowing systems the bacteria accumulate near the walls of the flow cell leaving a region in the center of the channel with significantly less bacteria then the surrounding walls.[82,83]

3.1.2 Design of Model *E.coli.* System

E. coli is currently the most studied bacteria and the most used model organism for use though out many different types of academic and commercial reseach.[198] As a result of its extensive use, considerable effort has been made in sequencing the genome of many common laboratory and pathogenic strains. A summary schematic of the genetic modifications and strains used in the design of our model *E. coli* system is shown in Figure 20. The Kieo collection was used as the basis for the model *E. coli* system due to the availability of isogenic mutants.[199] *E. coli* BW25113, *E. coli* JW1881 and *E. coli* JW1879 were purchased from the Coli Genetic Stock Center (New Haven, CT). *E. coli* BW25113 (Parent Strain) is the parent stain of the Keio collection. *E. coli* JW1881 (No Flagella) is a modified strain with a genetic knockout of the flhD gene which is critical for the growth

of flagella.[200] *E. coli* JW1879 is contains a genetic knockout of the motA gene that is necessary for proton-conducting in the flagella motor, yet does not effect flagella synthesis.[201] In order to upregulate the growth of flagella, in both isogenic mutant strains, a pflhDC plasmid (details of plasmid design and procedures is found in section 3.2.2.2) was cloned into the isogenic mutant strains. In the No Flagella strain this plasmid restores and upregulates the motility of the bacteria, producing a Super Swimmer strain. By cloning the same plasmid into the motor mutant strain flagella growth were upregulated without restoring motility. This strain called the "No Motor" strain has a similar number of flagella as the Super Swimmers, but lacked the ability to swim.

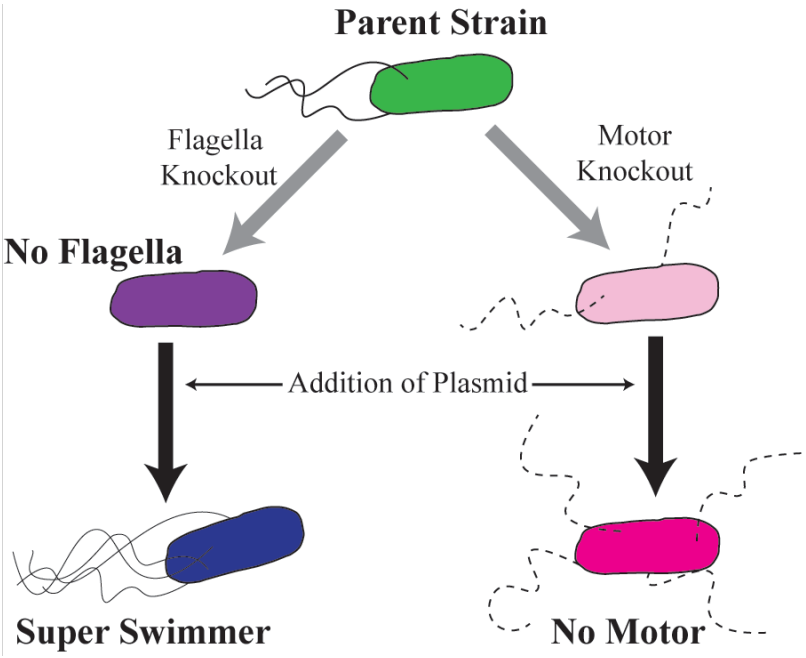

Figure 20. Design of model *E. coli* system. The Keio collection was chosen due to the availability of single gene knockout mutants. Two mutants, one for flagella and one for flagella motors were chosen. These strains were further modified with the constructed pflhDC+EGFP plasmid to upregulate the growth of flagella.

3.2 Materials and Methods

3.2.1 Materials

Tryptone, sodium chloride, and yeast extract were purchased from Sigma-Aldrich (St. Louis, MO). Agar, Na_2HPO_4, and KH_2PO_4 were purchased from Fisher Scientific (Fair Lawn, NJ).

3.2.1.1 Polyethylene glycol

Polyethylene glycol (PEG) (Figure 21) is currently the commercial gold standard for resistance to biofouling. PEG has been shown to be resistant to protein adhesion through two different mechanisms. The first mechanism is steric hindrance where the PEG chains from a steric barrier that prevents the protein from being able to encounter the surface.[202] The second method is a hydration layer where in addition to the steric hindrance, PEG chains will swell and hydrogen bond with water when in an aqueous environment. This creates an osmotic pressure gradient that prevents proteins and bacteria from encountering the surface.[203] While PEG is the commercial gold standard, it is not perfect. Over long time scales bacteria and protein can adhere due to the ability of PEG to hydrogen bond, and PEG will eventually break down in high salt conditions like those found within the body.[204]

Figure 21. Molecular structure of PEG, the current commercial gold standard for resistance to biofouling.

3.2.1.2 PLL-PEG Brushes

Poly-L-lysine-g-PEG copolymer (PLL-PEG) brushes (Figure 22) were used as the model PEG surface. PLL-PEG brushes were synthesized and characterized as previously described.[205–208] Briefly, PLL with a molecular weight of 15,000-30,000 Da was dissolved in a pH 9.1 sodium borate buffer. PLL was then reacted with a sodium valeric acid terminated 5,000 MW PEG (Laysen Bio Inc, Arab, AL). The amount of PEG molecules added to the reaction was adjusted to allow approximately one third of the amine groups on the PLL to be functionalized. After the reaction was complete product was purified by dialysis, lyophilized and stored at -20°C until use. Extent of functionalization was determined by comparing the relative areas of side chain peaks (-CH_2-CH_2-) to (-CH_2-N-) in ^{1}H NMR (Brunker 400MHz).

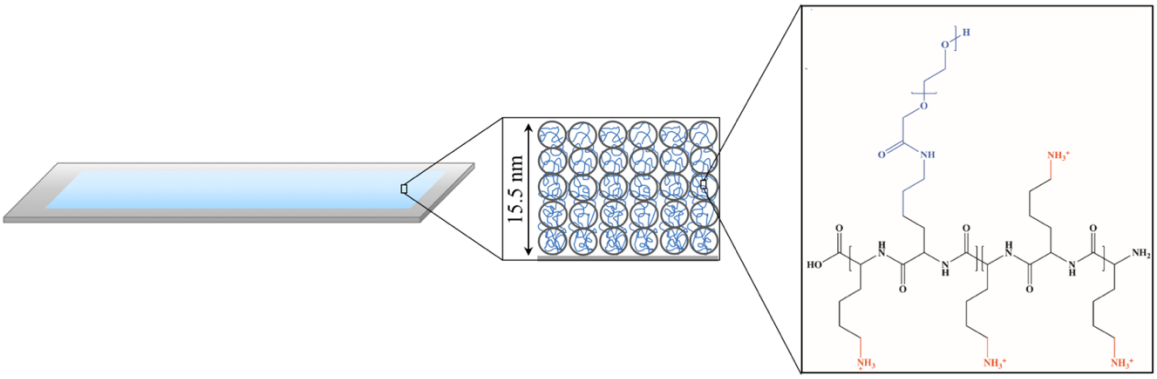

Figure 22. Molecular structure and schematic of PLL-PEG brushes. PLL portion of brushes adsorbs flat on glass substrate leaving a PEG brush coming up from the surface.

In order to functionalize the surfaces for testing, glass slides (Fishers Finest) were etched overnight concentrated sulfuric acid. This treatment has been shown to produce a pure silica surface.[163] Slides were functionalized by flowing a 100 ppm PLL-PEG solution in pH 7.4 phosphate buffer (0.008 M Na_2HPO_4 and 0.002 M KH_2PO_4) over the glass surface at a shear rate of 15 s^{-1} for 10 minutes followed by 10 minutes of buffer. Finally, the flow

cell was flushed for 10 minutes with the PBS prior to introducing bacteria into the flow chamber. The flow cell was not opened or exposed to air between adsorption of the brush on the surface. The brush system has been shown to be protein resistant and does not degrade in the salt concentrations used in these experiments.[156,191,209] When adsorbing to the surface the PLL backbone adsorbs to the surface leaving the PEG side chains to come off the surface to form the brushy layer (Figure 22). The brush architecture used in this study has an approximate brush height of 15.5 nm.

3.2.2 Methods

3.2.2.1 Bacteria Growth

Bacteria were grown in overnight at 37°C in Luria- Bertani broth (LB) with antibiotics as required: no antibiotics for the Parent Strain, 50 µg/mL kanamycin for the No Flagella strain, or 50 µg/mL kanamycin and 100µg/mL carbenicillin for the Super Swimmer and No Motor strains. After overnight growth, liquid cultures were restarted using 200 µL of overnight culture in 5 mL of LB and same antibiotics. Additionally, in the restarted cultures 50 µL of 20% wt/vol arabinose solution was added to the Super Swimmer and No Motor Strains to induce the flhDC plasmid. These cultures were grown for 4 hours and harvested in the log growth phase.

Bacteria cultures were then washed 3 times (centrifuged at 3500 rpm for 2 min) in pH 7.4 Phosphate Buffer Saline (PBS) (0.008 M Na_2HPO_4, 0.002 M KH_2PO_4, and 0.15 M NaCl) and resuspended in the same buffer at a concentration of approximately $1x10^8$ cells/mL. This concentration is below that were bacteria-bacteria interactions were found relevant at surfaces.[210] The concentration was determined using OD600 measurements.

3.2.2.2 Design of pflhDC Plasmid

The plasmid design and genetic modification in this section was done by Vishnu Raman in the Forbes lab. To upregulate flagella growth the flhDC gene was amplified using PCR from the Salmonella (SL1344) genomic DNA using the following primers: Forward aaaaaaCCATGGgtTAATAAaaggaggaatatatATGCATACATCCGAGTTGCTAAAACA Reverse-aaaaaaCTCGAGaaaaaTTAAACAGCCTGTTCGATCTGTTCAT (Invitrogen). The PCR product was digested with NcoI-HF and XhoI-HF (New England Biolabs). The PBAD-his-myc A plasmid (Invitrogen) was also digested with NcoI-HF and XhoI-HF (NEB). The digested vector and PCR product were mixed together at a ratio of 50 nanograms of plasmid backbone to 500 nanograms of PCR product and ligated together with T4 DNA ligase in ligase buffer. The resulting plasmid (pflhDC) was transformed into DH5alpha E. Coli (CGSC). To allow fluorescent detection of bacteria, the plasmid also contained a green fluorescent protein expression cassette. The GFPmut3 protein was amplified through PCR using the following primers: Forward: aaaaaaGCGGCCGCTTTACACTTTATGCTTCCGGCTCGTATAATGAATTCAAAAA AAAGGAGGAAAAAAAATGAGTAAAGGAGAAGAACTTTTCA and reverse: aaaaaaGCGGCCGCTTATTTGTATAGTTCATCCATGCCAT (Invitrogen). The pflhDC plasmid and EGFP PCR product were digested with NotI-HF (NEB). After using a PCR cleanup column (Zymo Research), the NotI-HF digested PCR product and pflhDC plasmid were ligated together with T4 DNA ligase in ligase buffer to create the pflhDC+EGFP plasmid. The resulting plasmid was transformed into DH5alpha.

The pflhDC+EGFP plasmid was transformed into the JW1879 and JW1881 strains as seen in Figure 20. Briefly, JW1879 or JW1881 was grown in Luria broth (LB Media) to an OD

of .5, washed twice with ice cold deionized water and transformed with 100 ng of plasmid DNA using electroporation. (#FB101, Fisher Scientific). Bacteria were recovered in LB Media for 30 minutes and plated on carbenicillin plates (Chem Impex international) overnight for subsequent studies.

3.2.2.3 SEM Characterization

After the final growth step described above, bacteria were washed by centrifugation at 3500 rpm for 2 minutes in deionized (DI) water 3 times and then fixed in 2.5% Glyceraldehyde solution in DI water for 2 hours followed 3 additional washes in DI water. 20 µL of resuspended bacteria solution was pipetted onto the center of a piece of a clean silicon wafer and allowed to air dry overnight. Samples were sputter coated (Cressington Sputter Coater 108) with gold for 60 seconds prior to imaging with a FEI Magellan 400 XHR-SEM.

3.2.2.4 Plate Motility Assay

In order to test the motility of the bacteria strains soft hydrogel plates with 0.4% agar in LB Media, in 10 cm petri dishes were made immediately before beginning assay. 2 µL of liquid culture was pipetted into the center of the plate and location marked. Plates were then incubated at 37ºC for 72 hours. In order to determine relative motility between strains the distance that the bacteria growth front traveled was marked and measured every 24 hours. This is a generally accepted assay used to confirm motility of bacteria.[211]

3.2.2.5 Bacteria-Surface Interaction Studies

Studies of interactions between flowing bacteria and a PEG brush were conducted in a custom-built flow cell system in which the test surface comprised one wall of the flow chamber. Both the microscope was oriented horizontally on an optical bench to few the

test surface which was oriented perpendicular to the floor, to prevent gravity from affecting cell-surface interactions. The objective used for these studies was a Nikon Plan Fluor 20x objective with a numerical aperture of 0.5. This gave a depth of field of approximately 3.5 μm. Bacteria were flowed across the surface at a shear rate of 15 s^{-1} for approximately 10 minutes. Data was recorded on DVDs and framed at a rate of 5 frames per second using FFmpeg software. Manual tracking was done using *FIJI is just ImageJ*.

3.3 Results

3.3.1 Characterization of Bacteria Modifications

Studies were conducted to establish that the genetic modifications described in the Experimental Methods Section (Section 3.2.2) produced the intended morphological features and dynamic behaviors.

3.3.1.1 SEM of *E. coli* and Their Flagella

Representative scanning electron micrographs in Figure 23, confirm the presence and absence of flagella in the four strains. The interpretation of the micrographs is limited to a qualitative assessment of the relative numbers of flagella between strains, as we found evidence that specimen preparation breaks many others that were much shorter then typically seen and much shorter than a single helix length. The majority of the flagella in the Super Swimmers seen are well over 5 μm in length and have a defined helical pattern. A few however, are significantly shorter (~1 μm) and end in the middle of a helix. Both of these are shown in image in Figure 24. In both the Super Swimmer and No Motor strains, which contained the flhDC plasmid, a large number of flagella are seen in all micrographs. Many cells had several flagella, though some had a single flagellum. By contrast, with the flhD gene knocked out in the No-Flagella strain, no evidence of any flagella was found in

any micrograph. The micrograph of the Parent Strain shows few flagella attached to cells. Most of parent strain cells did not possess flagella after the completion of sample SEM preparation steps. The few cells that did retain their flagella generally only had one visible flagellum, as shown. The results indicate that the pflhDC plasmid does upregulate the growth of flagella when compared to the Parent Strain. Additional micrographs of all strains are shown in Figure 25.

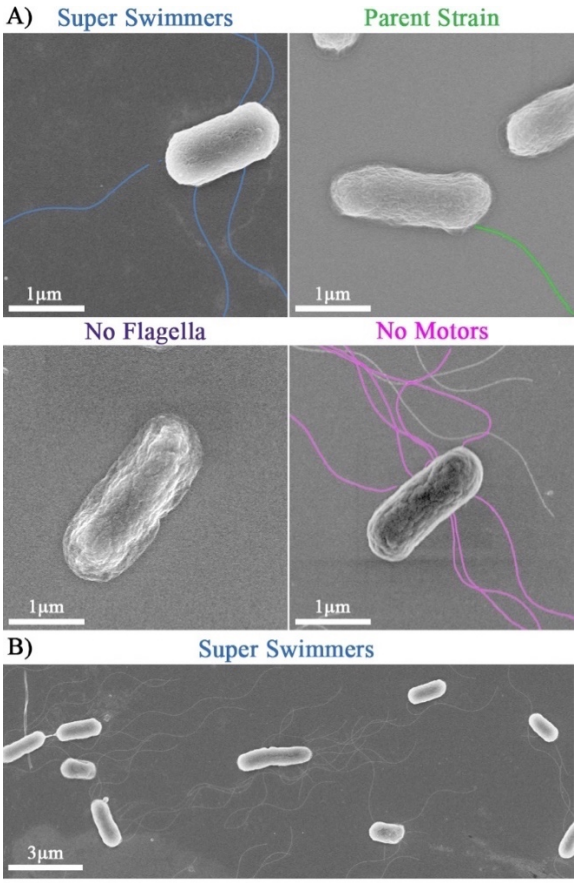

Figure 23. A) Scanning electron micrographs confirming the presence (or absence) of flagella on each of the strains. Flagella attached to cells are highlighted. B) Typical image with many Super Swimming cells.

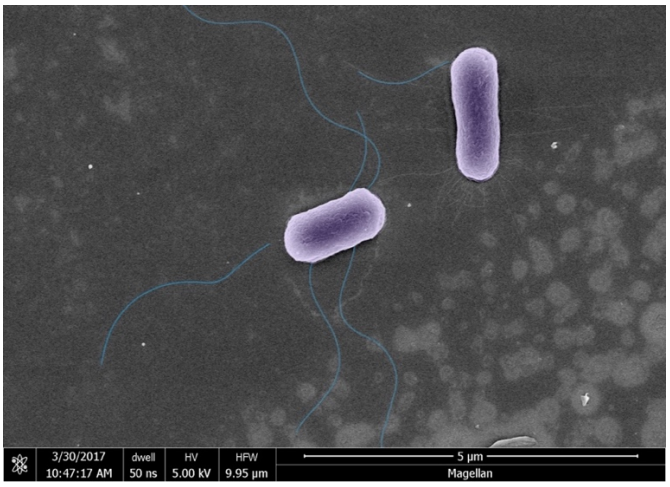

Figure 24. SEM showing evidence of flagella breakage. Both bacteria contain flagella shorter then typically seen and the left most flagella on the left bacteria is broken off from the cell.

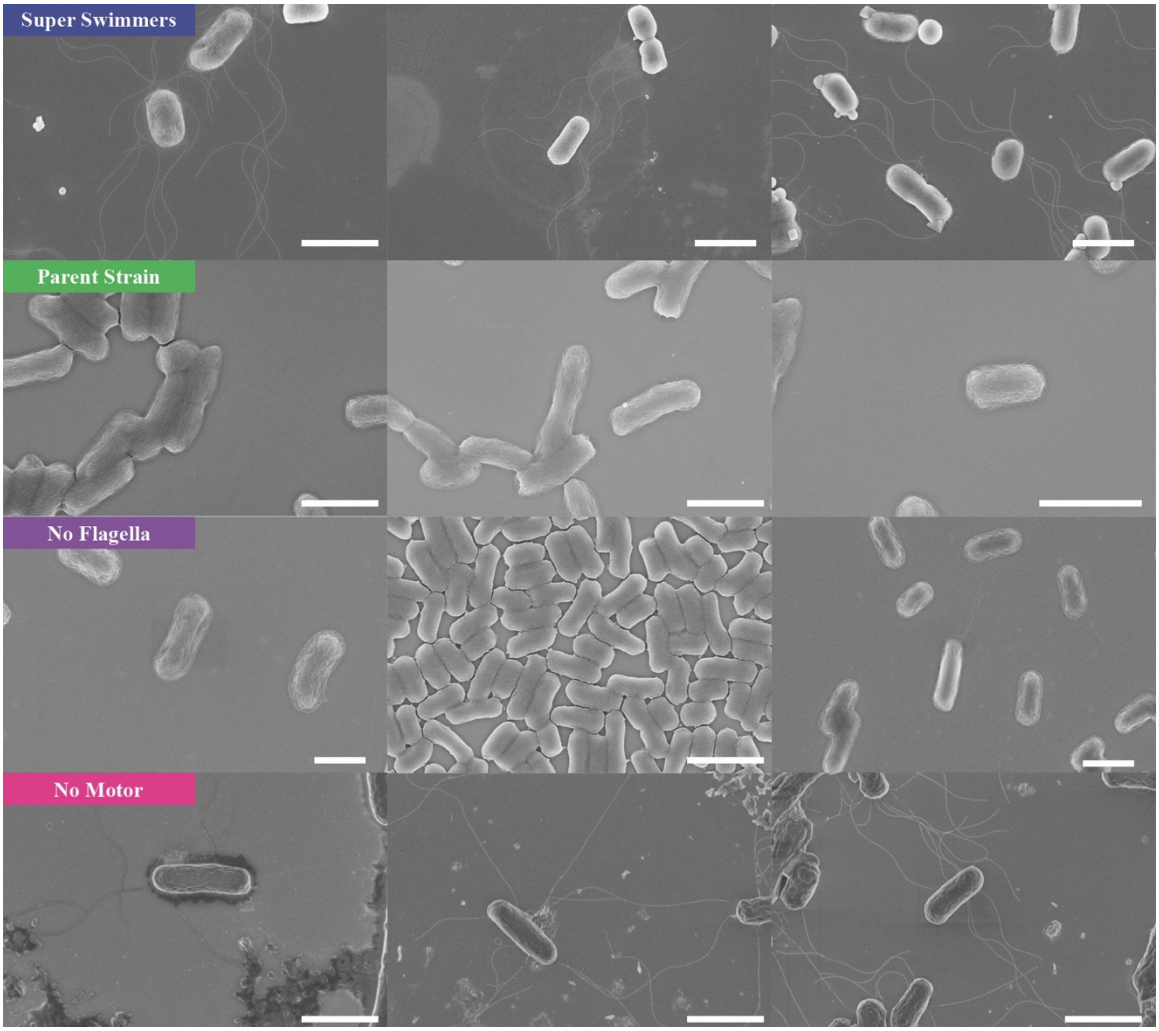

Figure 25. Additional SEM of all strains studied. Scale bars are all 2um.

3.3.1.2 Verification of Motility of Bacteria

A plate motility assay was used to confirm the motility of the different strains. This assay establishes bacterial motility based on the observed colony expansion as a result of cells swimming or swarming outward from an inoculated region at the center of an agar plate.[212,213] Figure 26A presents images of the plates 72 hours after inoculation. The Super Swimmers and the Parent strain exhibit substantial mobility with the Super Swimmers reaching the edge of the plate more rapidly, as summarized in Figure 26B. Conversely, the persistently small size of the No-Flagella and No-Motor colonies, with only slight colony expansion due to crowding, is consistent with the intended lack of mobility in these strains. The combined micrographs and motility results demonstrate that the No-Motor strain lacks motility despite its multiple numbers of flagella per cell, consistent with the intended non-functioning motors at the base of each flagellum. [214] Worth noting, the plate motility assay confirms general swimming activity but does not address the sizes of motile and non-motile populations within a batch.

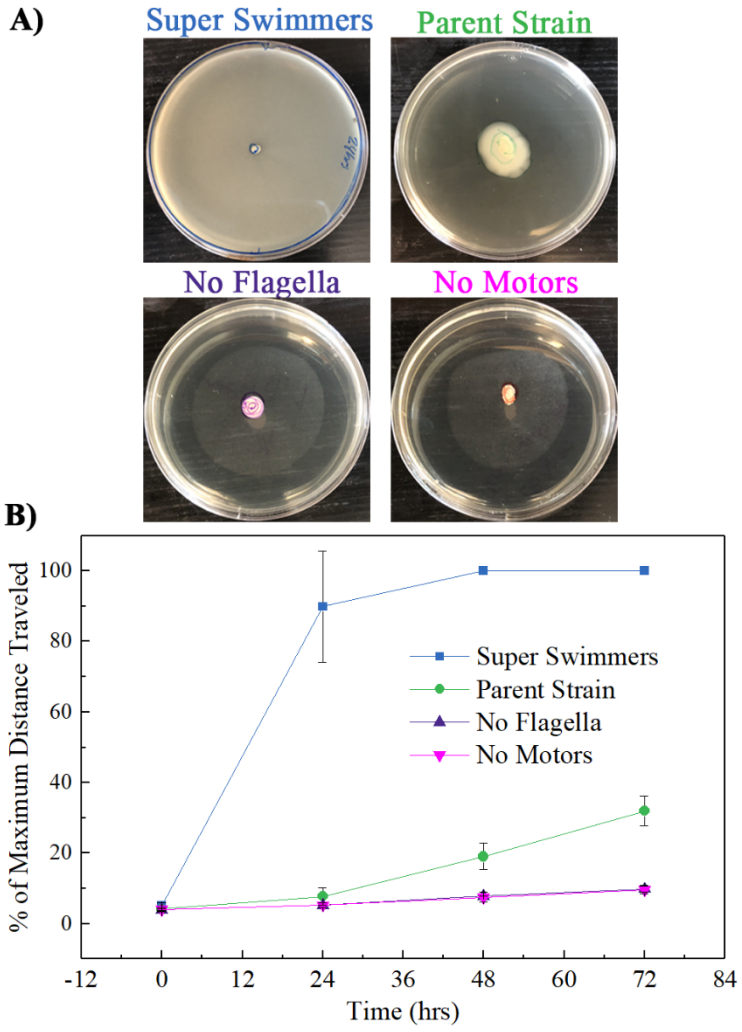

Figure 26. A) Motility plates showing the colony sizes at 72 hours for the four strains. B) Relative colony size, normalized on plate radius, as a function of time.

3.3.2 Near-Surface Cell Engagement and Tracking

Coating flow chamber surfaces with a PEG brush rendered them negligibly adhesive, unable to capture or arrest flowing *E. coli* cells. Cells of the different strains, did, however, exhibit distinctive near-wall motion signatures, influenced by their cell morphology and motility, potentially combined with strain-dependent hydrodynamic and weak reversible adhesive interactions, at the focus of this study. Of the millions of cells flowing through the 700 µm- thick chamber, only a subset of those approaching the brush-modified test

surface within the ~1.5 μm depth of field of the microscope had the chance to interact with the surface and these were tracked, as described in the example below.

As an example of how we quantified the near-surface motion of flowing cells, Figure 27 shows the results of manually tracking a typical No-Flagella *E. coli* cell. The cell enters the field of view traveling quickly. After about 2 seconds the cell slows down and travels at a velocity of about 8.3 μm/s for a period of 1.2 seconds. It then travels more quickly for about 2.8 seconds before briefly encountering the surface and then traveling quickly once again. After an additional 3 seconds, the cell exhibits a period of protracted slow movement, at about 7.9 μm/s to the edge of the visible field and then it exits. The differences in cell velocity indicate that the cell is moving perpendicular to the surface, sampling streamlines of different speeds, potentially changing its orientation and experiencing viscous drag and reversible adhesion when it is close to the surface. When the cell engages the surface through reversible adhesive interactions or viscous drag against the ~10 nm thick PEG brush, its velocity is reduced below what it would be, moving freely on the same streamline at the same orientation. (With a particle Reynolds number of $\sim 10^{-4}$, cells are dominated by viscous rather than inertial effects, and so bouncing and rebounding is not a suitable explanation for periods of slow movement.) Figure 27 demonstrates that some interactions between a cell and a surface can produce protracted periods of relatively slow near-surface travel. As seen in Figure 27, it was generally the case that when a cell was moving slowly, it exhibited smaller velocity fluctuations than it experienced when it was moving quickly, further evidence of interactions with the PEG brush.

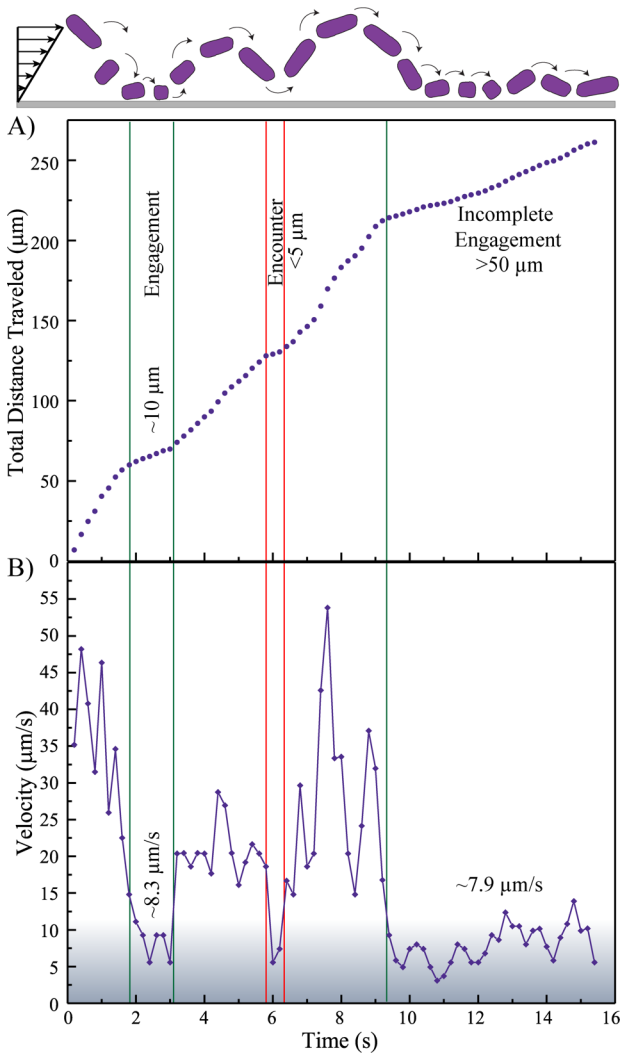

Figure 27. Total distance traveled (A) and instantaneous velocity (B) as a function of time for a typical No Flagella *E. coli* cell traveling near the surface in laminar shear flow with a shear rate of 15 s^{-1}.

For the purposes of this chapter, and without arrest of cells on these surfaces, we sought a working guideline to distinguish cells with surface interactions from those moving freely. Then for surface-interacting cells we compared the behaviors of different strains. With flowing near-surface cells interacting intermittently and reversibly with the surface, we identified dynamic adhesive interactions and protracted hydrodynamic interactions, terming them "surface engagements." During engagements, the rate of cell travel along

the surface was substantially reduced from what it would be without engagement. In identifying cells moving slower than the free stream velocity, we were guided, in part by Brenner's treatment of a sphere flowing over a wall in in shear flow. For a sphere diameter of 2.5 μm with its surface just nanometers from the wall, the sphere's velocity is about 9.7 μm/s. Though the present cells are not spherical, and without a better model we considered this velocity as one measure of the minimum free cell travel velocity, below which cells must be interacting with the surface. Also taken into consideration, for a wall shear rate of 15 s^{-1}, the streamline velocity 2 μm from a surface is 30 μm/s or, 1 μm from the surface the free stream velocity is 15 μm/s, values similar to typical straight swimming velocities of 20 μm/s.[215,216] Thus even for straight swimmers, the near-surface flow is strong enough to dominate bacterial movement via swimming, and more than a few microns from the wall, bacterial travel is entirely dominated by the flow. These considerations motivated our categorization of slow-moving cells, traveling less than 9.3 μm/s for a distance of at least 5μm (approximately two body lengths) as being engaged with the surface. Thus, we analyzed cells having runs of dynamic adhesion that persisted for at least 0.6 s. While some cells may have engaged dynamically, for instance by reversible adhesion, for shorter times these engagements were not trackable with our framing rate and with magnification of our experiment. The 5 μm travel requirement ensures that slight errors in manual tracking did not produce erroneous engagements. This work employs this working definition to distinguish cells that are freely moving from those whose interactions with the surface have influenced and reduced their motion. In this way we consistently identified populations of engaging cells for further study.

Based on this definition of an engagement, the cell shown in Figure 27 experiences two engagements plus a shorter encounter that does not qualify as an engagement. The second of the two full engagements extend beyond the field of view and can be counted in the numbers of engagements but could not be included in other analyses such as engagement lengths or average engagement velocity.

While the ~9 μm/s criterion to define an engagement appears arbitrary, we find that moderate variations in the choice of cut off velocity had minimal impact on the statistics and conclusions reported here. The effect of choosing a larger cutoff is that there are more engaged cells per unit time and area and somewhat longer engagements; however, the effect is small. For instance, choosing a velocity of 11 μm/s rather than 9 μm/s, in the sample run shown in Figure 27 the additional encounter that previously did not qualify as an engagement would qualify as a short engagement with a length of 5.9 μm. There is no effect on the length of the other complete engagements. The choice of cut off is additionally consistent with the observation that during engagement, we find velocity fluctuations reduced compared to that during cell motion away from the wall. As an example, for the run in Figure 27, the variances of the velocities for the two engagements were 4.2 and 6.2 $\mu m^2/s^2$, while for the periods of time between engagements it was 93 $\mu m^2/s^2$. This difference in variance between the engaged and non-engaged velocities is seen across all the runs. Thus, we proceeded with this working criterion for cells that were adhesively or frictionally engaged with the surface, warranting further analysis and enabling comparisons between the different strains.

3.3.3 Effective Surface Engagement Flux

A first measure of the differences between the near-surface dynamics of the four strains is the numbers of cells per unit area engaging the surface in a given time. This flux of engaging cells, shown in Figure 28, counts the numbers of cells having at least one engagement in the field of view and is corrected to account for slight batch to batch variability in cell concentration near the working concentration of 1.0 $x10^8$ cell/ml. This engagement flux is, for the dynamic adhesion of engagements, analogous to the classical capture rate of adhering cells, particles, or adsorbing molecules per unit area of wall in shear flow. In the classical case where diffusing species adhere rapidly to a wall from shear flow, the Leveque treatment predicts the maximum or diffusion-limited accumulation. The engagements of nonmotile cells like those in Figure 27 also require diffusive approach to a surface. A fraction of the cells reaching the surface engage reversibly through physicochemical or hydrodynamic interactions. The maximum flux of engaging non-motile cells is expected to be diffusion-limited, as described by the Leveque treatment. Here a dilute solution diffusivity is typically employed and, additionally, the near-surface interaction of cells is assumed not to influence cell behavior. For the capture and accumulation of bacterial cells at these bulk solution concentrations and flow rates[217], and for *S. aureus* near an interactive surface that does not trap cells,[191] such cell-cell interactions were confirmed to be negligible.

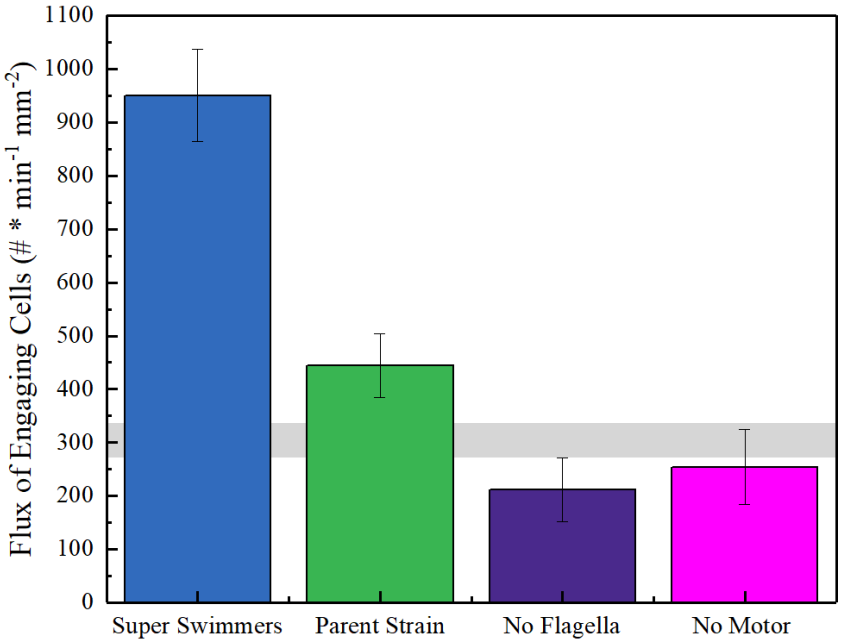

Figure 28 Flux for engaging cells of different bacterial strains, defined as the number of cells having at least one engagement in the field of view. Data are based on the analysis of 30 s segments of video. Analysis of multiple sections (minimum of 3 per strain) of video gave identical fluxes within error bars shown.

The Leveque treatment predicts a diffusion-limited cell accumulation rate (or maximum flux of engaging non-motile cells) of approximately 305 ± 35 cells per min per mm^2 This estimate employed a free solution diffusion coefficient of approximately $4 \pm 0.5 \times 10^{-9}$ cm^2/s for the cells, which were modeled as rods having a length of 2 ± 0.25 μm and a diameter of 0.5 ± 0.1 μm[218]. (This estimate also neglects any near-wall shear effects on the diffusion, which may be important for rod-shaped particles.) In Figure 28 this estimated upper limit exceeds the flux observed for the non-motile No-Flagella and No-Motor strains by a modest amount, as expected, since not all surface encounters might produce engagements. Thus, the effective engagement efficiency is less than one. The two motile strains exhibit a higher flux of engaging cells then is seen for passively diffusing cells. Indeed, the diffusive flux of the Super Swimmers and Parent strains exceeds the estimated diffusion-limited rate for cells of these size, an indication that cell motility or swimming,

contributes to the numbers of cells dynamically engaging the surface. For the motile cells the engagement process involves both swimming-enhanced transport to the surface and hydrodynamic or reversible physicochemical binding. Important to note is that non-motile populations within batches of the Super Swimmer and Parent cells are not distinguished in the engagement fluxes of Figure 28. Non-motile fractions will encounter the surface through diffusion and would likely contribute fluxes similar to those of the No-Flagella and No-Motor strains. To the extent that the fluxes in Figure 28 contain some fraction of non-motile cells, the reported fluxes in Figure 28 represent a lower limit for the behavior of motile cells.

3.3.4 Number of Engagements per Cell

Distinct from the numbers of cells that reach the surface to dynamically engage, reversible capture allows the same cell to engage the surface multiple times, as shown in the example of Figure 27. The distribution of the numbers of engagements per cell is presented in Figure 29 for the different strains. The Super Swimming cells had higher numbers of repeat surface engagements when compared with the other strains. While the other strains had less than 10% of bacteria having 4 or more engagements 30% of the Super Swimmers had more than 4 engagements. About 90% of Super Swimmers have multiple engagements while for the other 3 strains approximately half of the bacteria had only one engagement. While the exact statistics apply to the 260 μm-long field of view, the effective decay function in the repeat engagements is conceptually similar to a correlation function.

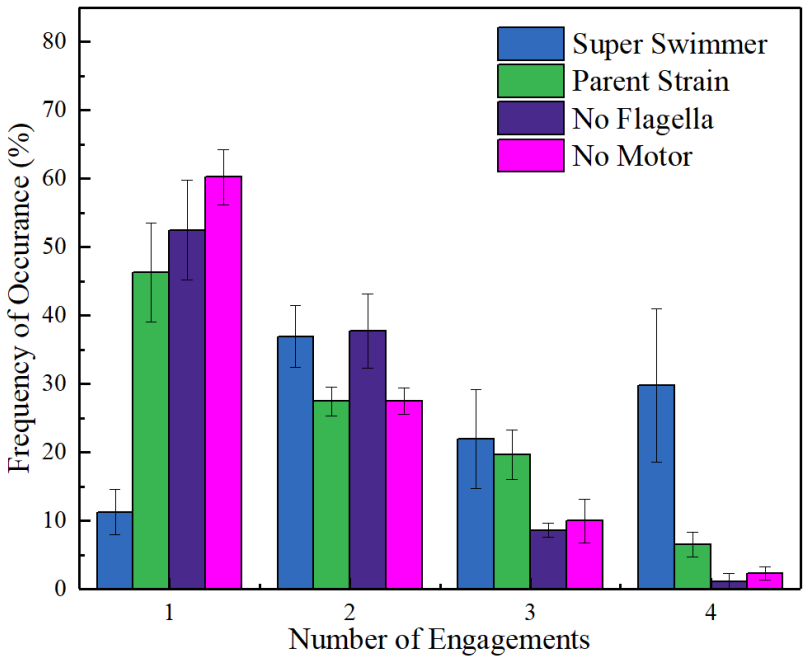

Figure 29. Number of engagements per cell within the 260 µm length of the viewing field. 25-35 bacteria per run were tracked for three runs with each strain. Error bars are standard deviations.

It is expected that even cells of the non-motile strains (along with synthetic particles) will have at a least a small number of repeat surface engagements. In order for the first surface engagement to occur, a bacterium must diffuse from the faster moving bulk stream lines to the slower moving near-surface streamlines where surface contact and engagement can occur. A recently disengaged cell in the near surface streamlines may diffuse further from the surface or it may re-engage. Even cells that have diffused some distance from the surface have a finite probability of returning to the interface where they can re-engage. An observed characteristic of diffusion-controlled repeat surface engagements is a decrease in frequency of occurrence with the increased engagement numbers, as is seen for both the No Flagella and the No Motor strains. The distribution for Parent Strain also shows this characteristic but exhibits a more gradual decay. The Super Swimmers on the other hand displayed very different behavior. Figure 29 demonstrates that once an engaged Super

Swimmer cell disengaged the surface, there was a ~90% chance that it would return to the surface at least once more within the observation distance of the flow cell. Indeed, cells of both motile strains have a statically higher average number of surface encounters per cell when compared to the diffusing strains.

Table 2. Average Numbers of Engagements per Cell, for Cells that Engage

Strain	Number of Engagements in Field of View	Expected Engagements per cm	Distance between Engagements (μm)
Super Swimmer	2.79	10.7	47.8
Parent Strain	1.89	7.2	37.5
No Flagella	1.50	5.7	51.6
No Motor	1.58	6.0	40.6

*Error bars are not reported here, as the full distributions are appearing in Figure 29.

3.3.5 Engagement Length and Time

In addition to the influence of bacterial strain on the flux to the surface and the numbers of engagements per cell, the strain also affects the character of the individual cell-surface engagements. The distribution of travel distances during individual cell-surface engagements is strain-dependent, as shown in Figure 30. The residence time per engagement, related to the travel distance, is also strain-dependent with Super Swimmers and the No Flagella cells having statistically longer residence times than the other strains and No Motor cells having the shortest residence time, in Figure 31. Average and median values are summarized in Table 2. Evident and statistically significant in the data are that longer (duration and distance) engagements of No Flagella and Super Swimmer cells compared with those of the No Motor and Parent Strains. Standing out in Figure 30 is a peak in the travel distances of the No-Flagella cells around 10-15 μm, and a more gradual

decay of the travel distance during engagement by the Super Swimmer cells. These data reflect substantial influence of flagella and, separately, motility, on the near-surface travel of bacterial cells.

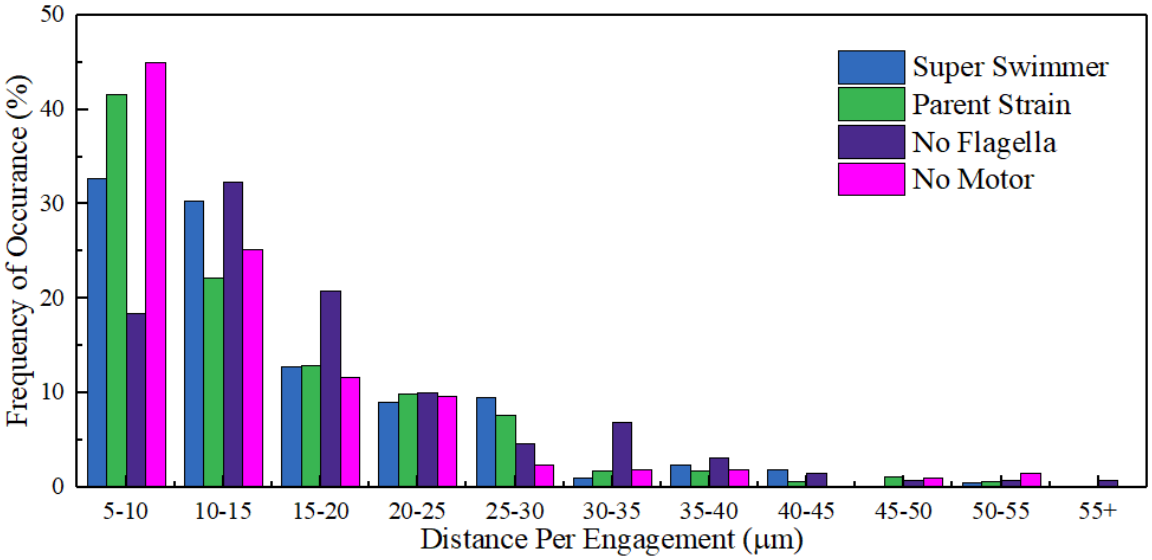

Figure 30. Distribution of Distance Per Engagement. 25-35 bacteria per run with 3 runs per strain. Only full engagements are included.

Table 3. Statistics of lengths of engagements.

Strain	Average Engagement Distance (µm)	Median Engagement Distance (µm)	Average Residence Time per Engagement (s)	Median Residence time per Engagement (s)
Super Swimmer	15.0	12.2	2.1	1.8
Parent Strain	14.8	11.6	1.7	1.4
No Flagella	16.7	14.4	2	1.7
No Motor	14.4	11.1	1.6	1.2

* Standard deviation is not provided, as the full distance distribution is presented in in Figure 30 and the distribution of Residence Times per engagement is included in Figure 31.

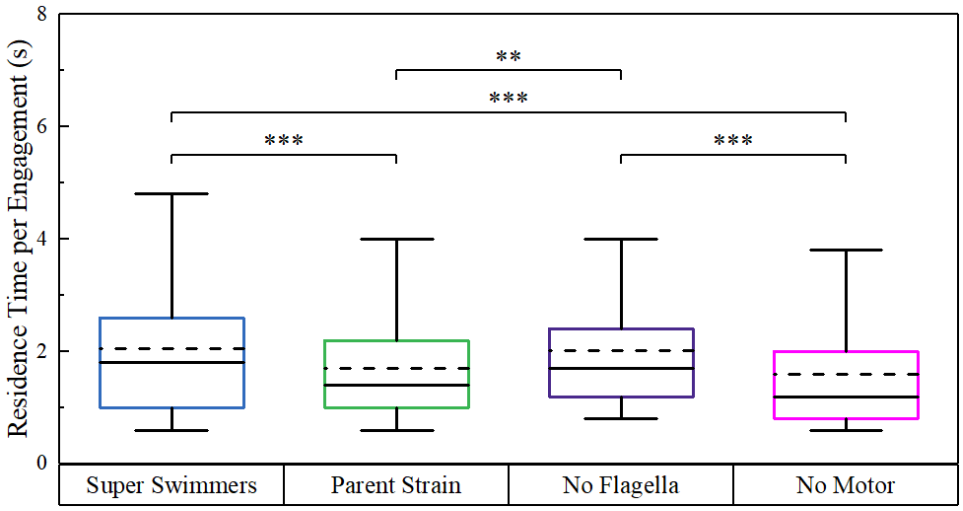

Figure 31. Residence Time per Engagement. Solid lines are the median value with dashed lines for the mean values. Whiskers are for range of data minus outliers. *** indicates $p<0.01$, ** indicates $p<0.05$

3.3.6 Average Engagement Velocity

Engaged cells moved more slowly than those in free solution, often exhibiting relatively constant velocities with small variance, in the example of Figure 27. Figure 32 shows the distribution cell velocities averaged during individual engagements, with one average velocity determined for each engagement as indicated in the example of Figure 27 and tallied for the different strains. Engagements with overall travel distances below 15 μm are not included in Figure 32 due for the potential for averages to be skewed by the incoming and exiting velocities for engagements of short run length. We generally observed no correlation between engagement length and velocity, justifying this approach. The key finding in Figure 32 is that average engagement velocity is much slower for the Super Swimmer cells than any of the other strains. This slowing down of engaged Super Swimming cells upon engagement is particularly dramatic because the same cells traveled

more quickly, compared with the cells of other strains, in near surface streamlines, for instance prior to and after engagement.

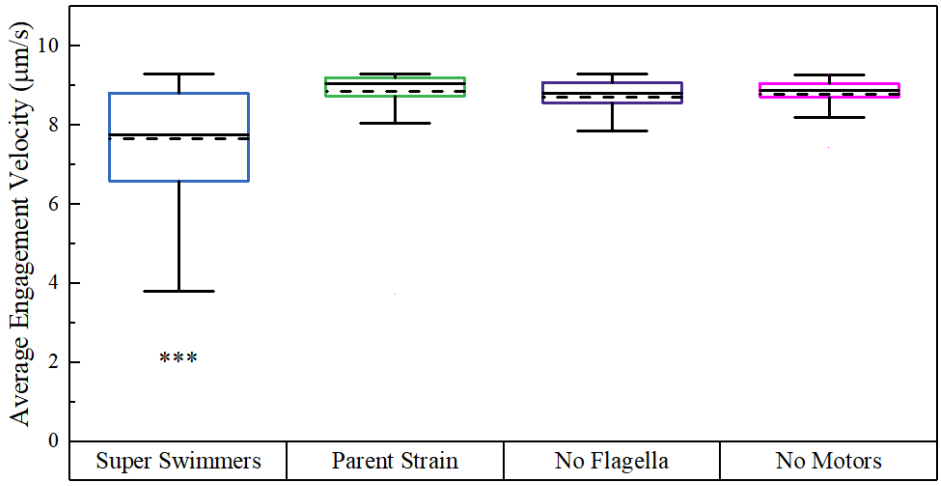

Figure 32. Average velocity per engagement for engagements longer than 15 µm. Median lines are solid, and mean are dashed

3.3.7 Instantaneous Velocity

The distributions of instantaneous velocities, measured from point to point (every 0.2 s) for cells having least one engagement, are summarized in Figure 33. The velocity distributions include non-engaged movements of these cells while they are in the field of view, providing additional perspective. Figure 33 shows distinctly slower velocities for the Super Swimmers compared with the other strains, in parallel with the per-engagement velocity in Figure 32 and a result of inclusion of the engaged cells. This is the opposite trend in the motility assay of Figure 26 where Super Swimmers exhibit the greatest overall travel velocity.

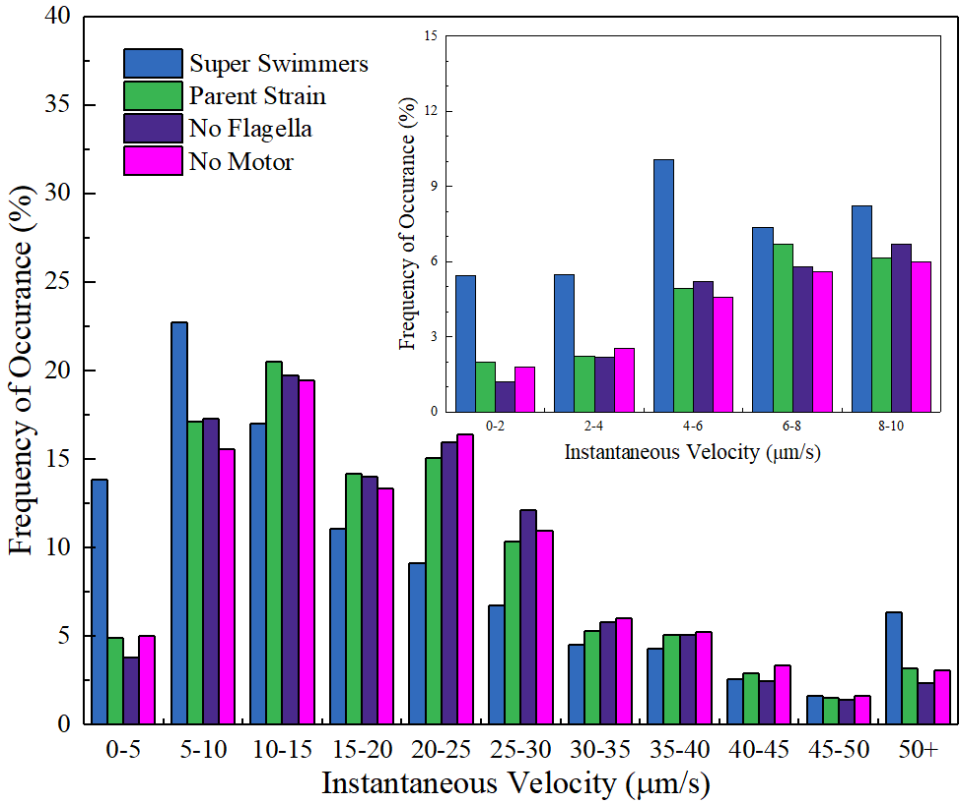

Figure 33. Distribution of instantaneous cell velocities for cells having at least one surface engagement. The main graph includes the full range of velocities (measured every 0.2s) including those for free cell motion while the inset summarizes instantaneous velocities during engagements.

3.3.8 Overall Residence Time

The overall surface residence time of cells engaging the surface in the 260 μm field of observation, summing over the times of any multiple engagements, is shown in Figure 34. This metric provides a measure of the times the cells spend in contact with the surface, having an opportunity to sense an impenetrable barrier. A bacterium that was engaged with the surface for the entire length of the observable flow cell would be have an overall residence time of at least 29 seconds. Figure 34 shows that the Super Swimmer cells have longer integrated contact times with the surface by a significant amount, for instance with more than twice as much contact time per cell compared with the No Motor strain.

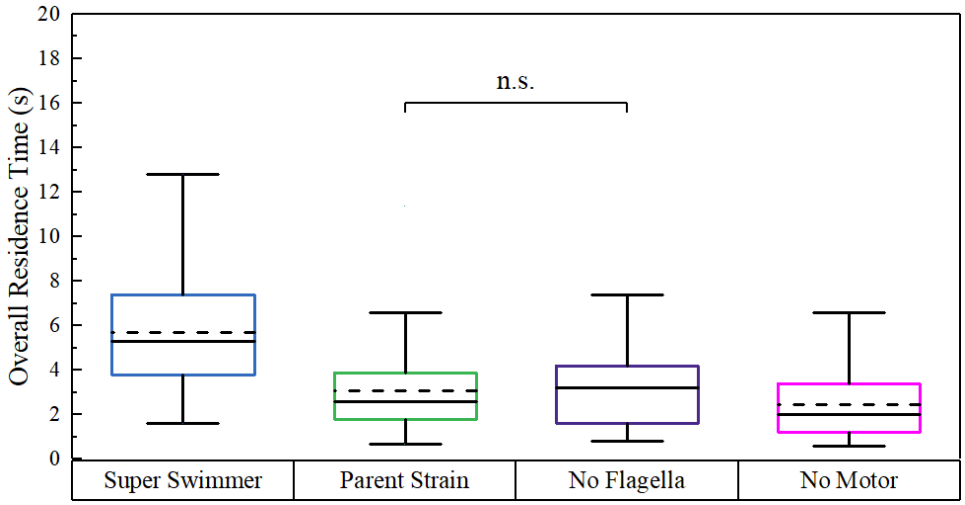

Figure 34. Overall Residence time. Solid lines are the median value with dashed lines for the mean values. Unless otherwise noted all data has $p<0.01$. Partial engagements (bacteria leaves or enters the field of view while engaged) were included in this analysis.

3.4 Discussion

This chapter reports strain-dependent differences in the numbers of cells per unit time reaching a biorepellant surface in shearing flow, the numbers of engagements events per cell, and differences in the character of the dynamic engagements. In further discussion, each engagement is conceived as a three-step process in Figure 35: the initial encounter, the near surface progression, and finally the disengagement from the surface.

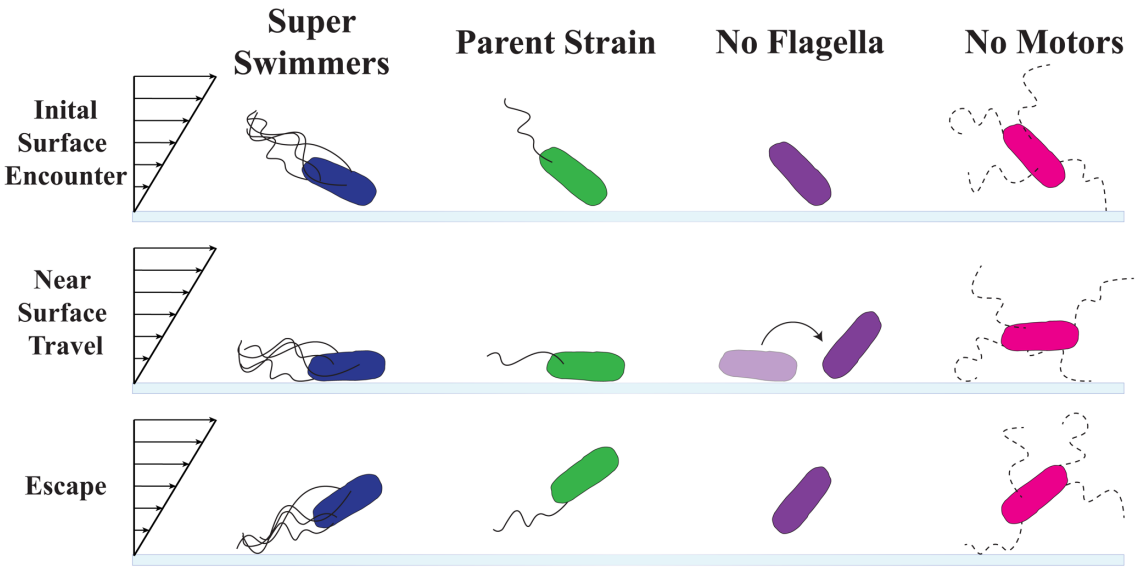

Figure 35. Schematic of different stages of bacteria engagements. Initial encounters, near surface travel and escape. Flagella bundling reflects the literature models of *E. coli* swimming.

3.4.1 Initial Engagement

Before a bacterium can engage the surface, it must first travel from the fast-moving bulk suspension to interfacial region where it may encounter the surface. Some cell-surface encounters are too fast to measure on video while others result in quantifiably slowed cell motion or "engagement", a result of hydrodynamic attractions with the wall, viscous interactions with the PEG brush, and /or reversible dynamic adhesion, for instance due to hydrogen bonds. As only a fraction of cell-wall encounters produce engagements, the engagement efficiency is typically unity or less. The maximum engagement flux, in which all cells encountering a surface area in a given time produce adhesive engagement, is well-described for non-motile cells in Figure 28 by the Leveque treatment[100] for diffusion-limited adhesion of a diffusing species. We have successfully employed the Leveque treatment to describe the capture of flowing 1 μm spheres on adhesive surfaces,[8,51,104–106,219] indicating that, even with a Peclet number of 1.1 as calculated in Chapter 2, 1 μm spheres

travel by diffusion. Use of the same approach to describe slightly larger non-motile *E. coli* cells appears adequate in Figure 28, employing an estimate for the diffusion coefficient of a rod-shaped particle. Notably for the nonmotile strains, the approach of the engagement flux to that estimated using the Leveque treatment suggests a relatively high capture efficiency.

In Figure 28, the active approach of Super Swimmer cells to the interface produces an engagement flux greater than that possible by diffusive transport. Since we cannot measure short encounters or know the overall encounter frequency, we cannot quantify the engagement efficiency of Super Swimmer cells. A greater number of swimming attempts (encounters) will increase the engagement flux of the Super Swimmers; however, a greater efficiency for successful engagement, will also increase the numbers of observed engagements. The net effect is that highly motile cells not only reach the interface more readily than non-motile cells, they engage the surface in greater numbers per unit area.

The apparent swimming of motile bacteria towards surfaces has been documented previously in quiescent[76,77] and flowing systems.[83] Bacteria are observed at higher concentrations near a chamber's compared with the bulk solution. One possible mechanism for this behavior, Rusconi, Guasto and Stocker report a cell-depleted region at the center of a flow chamber (with maximum depletion at shear rates between 2.5 and 10 s^{-1} [83]), as motile cells swim off-center towards the steeper velocity gradient. This is a separate mechanism than seen in the quiescent conditions when a hydrodynamic dipole-dipole interaction due to flagella motion produces a cell-wall attraction having a range on the order of the cell size.[76] The high engagement flux of Super Swimmer cells in the current

study likely includes both of these mechanisms. New in the current study, a flux variable rather than a static concentration is developed to quantify dynamic aspects of bacterial approach and engagement with a surface. Indeed, the shifting of a steady state concentration gradient of bacteria towards steep velocity gradients, described by Rusconi et al[83] produced a maximum of a 15% increase in cell concentration near the wall, relative the overall bulk solution value. Based on our shear rates and larger channel it is expected that we would have a smaller effect. Dynamic aspects of the bacterial motion are therefore key in explaining our findings, including almost a 3x greater Super Swimmer engagement flux compared with than that of control cells. Once in the near-surface regions, hydrodynamic attractions of the swimming bacteria may increase cell-brush contact increasing the engagement efficiency, for instance through more efficient hydrogen bonding. Such physicochemical interactions, if they involve the bacterial body, are possible for all four strains but may be enhanced in the Super Swimmers if these cells press into the brush.

3.4.2 Near Surface Travel

Once engaged, a bacterium travels along the surface with a velocity and velocity variance smaller than those of near-surface cells that move freely. The engagement velocity may be reduced relative to the free velocity by reversible physicochemical bonds between the bacteria and the PEG brush, for instance hydrogen bonding, by viscous drag at the brush surface, or in the case of motile cells, by swimming opposite the direction of flow (rheotaxis). The No Flagella cells likely experience intermittent tumbling or torpedo-like motion involving viscous or physicochemical interactions between the cell body and the PEG brush (not resolvable here at the low magnifications that facilitate tracking long distances). The similar near-surface velocities (in Figure 32 and Figure 33) of the No

Motor and Parent cells with the No Flagella cells suggest that during engagement, the flagella contribute minimally to physicochemical or viscous interactions and, additionally, that active swimming of the Parent strain has a negligible impact relative to the flow. (Indeed the motility and SEM characterization in Figure 23 and Figure 26 suggest that cells of the Parent Strain are weak swimmers and contain few flagella). Thus, even with the No Motor and Parent strains, cell bodies might interact with the surface of the PEG brush during engagement.

The Super Swimming bacteria on the other hand exhibit engagement velocities that are significantly slower than the other strains, a behavior that is unanticipated in light of the faster velocity of Super Swimmers away from a surface. There are two potential mechanisms for the slow engagement velocity of Super Swimming cells. The first is that swimming action and hydrodynamic dipole attractions push cells deeper into the PEG brush (compared with non-swimmers) where Super Swimmer cells experience greater viscous drag and physicochemical interactions with the brush. Indeed synthetic janus spheres undergoing self diffusiophoresis in quiescent conditions are known to travel slower in the presence of a wall and without flow.[220,221] The second possibility is that Super Swimmer cells are oriented by the shear field to swim against the flow. This upstream movement, known as rheotaxis, has been shown in to be possible in both biological and synthetic systems based solely on the physical mechanism caused by the hydrodynamic torque on the bacterium or particle.[61,84] At the shear rate studied we did not observe any net bacterial travel opposing the flow direction but we did observe a modest fraction of cells having velocity components perpendicular to the direction of flow.

3.4.3 Escape Frequency and Duration of Engagement

An engaged bacterium will travel along the surface until a disengagement event, such as a Brownian or flagella kick or a tumble that fails to bond, allows the cell to escape the surface. No Flagella cells exhibit relatively long engagement residence times in Table 3 potentially because a Brownian fluctuation or a missed bonding opportunity are the primary mechanisms for disbonding. (Compared with spheres which can readily roll along the surface, the 1 x 3 μm rod shape of *E. coli* may increase the chances of missed bonding during tumbling, through stabilization of surface-parallel orientations.[99]) By contrast No Motor cells exhibit statistically shorter residence times of engagement, likely due to the additional contribution of flagella to provide a steric kick that ends the engagement. Cells of Parent Strain exhibit engagement times similar to those of the No Motor strains, perhaps because the Parent Strain cells do not swim strongly enough overcome steric interactions of their flagella. Indeed, the Parent Strain exhibits established run-and-tumble dynamics[222] and so flagellar disengagement may kick these cells from the surface.

The Super Swimmer cells exhibit engagement times, in Table 3, that are statistically longer than the No Motor and Parent Strains, suggesting that potential disengagement events occur less frequently for these cells. Swimming may stabilize these cells near the surface, reducing disengagement by tumbling. Additionally, steric kicks from the flagella, which are bundled during swimming, occur less frequently or less effectively than with the No Motor or Parent strains. Worth mentioning, the Super Swimmer strain has the potential to unbundle its flagella and tumble, but tumbling may not occur as frequently or effectively as with the Parent Strain. This may be because large numbers of flagella remained bundled

and driving motion even when some flagella unbundle. We put this for the as a potential explanation and not a conclusion of this work.

While the apparent net tendency of motile bacteria and synthetic swimmers to swim towards walls is generally accepted, we know of no quantitation of swimming bacteria cells leaving an interface. The current report of finite surface engagement time for individual cells is therefore significant. Indeed, in descriptions of the swimming of bacteria towards surfaces,[76,185] there is no mention continued long time cell accumulation, suggesting that bacteria do indeed have a finite residence time. The longer residence times, in the flow of the current study against a minimally adhesive PEG surface therefore constitute an important new finding.

The significance of the bacterial residence time is borne out in the distance cells travel along a surface, with the engagement length being the product of the engagement time and the average engagement velocity for each cell. Longer engagement times result in the longer distances per encounter seen in the No Flagella strains in Figure 30 and Table 3. The No Flagella bacteria remain engaged with the surface for an average of 16.7 μm or about 3 end-over-end tumbles with over 18% of the bacteria having engagement lengths of over 25 μm. By contrast the No Motor and Parent Strains exhibit shorter surface residence or engagement times, likely a result of steric repulsions from pendant flagella. The shorter engagement times correlate with shorter engagement distances for these two strains with only 10.4% for the No Motor and 13.5% of the Parent Strain bacteria having engagements longer then 25 μm.

3.4.4 Repeat Engagements

Once a bacterium disengages from the surface the possibility exists for it to return to the surface within the field of view. For diffusive strains this repetitive nature of engagements is based on the statistics of the bacteria escaping the surface and remaining in the slower moving streamlines. It is more likely to diffuse back into the surface when it is already in the slower moving streamlines then when it is in the bulk. We see this behavior in Figure 29 for the No Flagella, No Motor and Parent Strains. The Super Swimmers are unique in that this behavior is not seen. Instead we find that if a Super Swimmer has one engagement it has about a 90% chance of returning to the surface for an additional engagement. This is likely due to a combination of the initial mechanisms that bring the super swimmers to the surface at a higher rate than the other strains in addition to the bacteria being already in the intermediate streamlines. Long range hydrodynamic swimming attractions to the wall may still have an effect in these intermediate streamlines which drive the bacteria to return to the surface.

3.4.5 Overall Interactions and Significance

Both motility and morphology substantially influence the net interactions of Super Swimmer and control cell lines with minimally adhesive PEG brush surfaces. As a result of longer residence times per engagement and repeat engagements per cell with 90% of Super swimmer cells experiencing multiple surface engagements, individual Super Swimmer cells spend more than double the time in contact with the wall than do the other strains, with some cells exhibiting contact times approaching 15 s in a distance of 260 μm. Though they may not travel as far as the no-flagella cells along the surface, during their slow near-surface travel, Super Swimmer cells experience to viscous or physicochemical interactions at the PEG-coated wall that may include forces on flagella. The duration of

this restriction, easily 10 seconds for each 260 μm length of surface, might ultimately initiate mechanosensory pathways such as a flagellar dynomometer cascade associated with early biofilm formation.[223] While it is established that adherent cells experience forces associated with mechanosensation, our findings of extended exposure of dynamically adhered cells to the surface environment suggests that cells might be stimulated/triggered on surfaces that are biopassivated, and travel to other sites to initiate infection.

3.5 Conclusions

Both the motility and the morphology of the bacteria play a significant role in the bacterial-surface interactions. Without flagella the No Flagella bacteria are able to approach the surface and dynamically interact with the surface for longer distances than any other strain. This is likely due to the lack of steric kicks from flagella interactions. On the other extreme the Super Swimmers are able to use their motility to stay engaged with the surface for longer periods of time. Their lower velocity however makes the overall distance traveled per engagement less than that of the No Flagella bacteria. Swimming also allows bacteria to actively transport to the surface increasing their number of interactions. Overall the Super Swimmers spend the most time engaging with the surface.

CHAPTER 4

SOFTER HYDROGEL SURFACES LEAD TO SHORTER BACTERIAL-SURFACE ENGAGEMENTS

4.1 Introduction

The initial interactions that lead to the capture of bacteria on a surface are key to understanding the formation of biofilms. The ability to tune these initial physical and chemical interactions enables the rational design of bio-resistant surfaces. In addition to the motility of the bacteria discussed previously it is extremely important to study the effect of the surface. It has been shown previously that the mechanical properties of a surface can be a critical component of bacterial-surface interations.[191,224,225] In this work, we study bacteria interactions with surfaces having different mechanical properties. Poly(ethylene glycol) (PEG) based surface coatings are known to be protein resistant due to their hydrophilicity, though their ability to hydrogen bond allows for some chemical interactions with the bacteria, depending on bacterial dynamics relative to the kinetics of bond formation.

Three PEG based surfaces: a poly-(L-lysine) (PLL)-PEG random graft co-polymer brush adsorbed to a glass, a soft 10% PEG hydrogel (310 kPa) and a stiff 50% PEG hydrogel (6500 kPa) are studied to probe how bacteria capture from flow is sensitive to the mechanical and chemical interfacial properties of a collecting surface. The current the commercial gold standard for resistance to biofouling, PEG, has been shown to be resistant to protein adhesion through two different mechanisms. The first mechanism is steric hindrance where the PEG chains form a steric barrier that prevents the protein from being

able to encounter the surface.[202] All three of the surfaces studies in this chapter provide a steric boundary between a bacterium and the underlying glass substrate.

The second mechanism is a hydration layer where in addition to the steric hindrance, PEG chains will swell and hydrogen bond with water when in an aqueous environment. This creates an osmotic pressure gradient that prevents proteins and bacteria from encountering the surface.[203] The amount of water in each of the surfaces varies, since the stiffer gel only contains approximately 50% water and the softer hydrogel contains 90% water, and when fully swelled the brush contains roughly 94% water. While PEG is the commercial gold standard, it is not perfect. Over long time scales bacteria and protein can adhere due to the ability of PEG to hydrogen bond, and PEG will eventually break down in high salt conditions like those found within the body.[204]

4.1.1 Biofilm Associated Infections

The adhesion and growth of bacteria on surfaces is a significant problem in many industries including healthcare. The ability of bacteria to form biofilms on medical devices is a pressing challenge in the medical field.[226] Intravascular and urinary catheters are two of the most commonly infected medical devices.[180] One of the most widely used techniques currently to prevent infections on these devices is the use of antibiotic eluting coatings. Although this can successfully reduce the number of infections, it also leads to the faster development of drug resistant bacteria.[227] This project aims to study the fundamental dynamic interactions between bacteria with different motility and morphological characteristics and surfaces of different mechanical properties to probe the earliest stages of interactions. This will ultimately lead to the design of more effective bio resistant materials.

4.1.2 Initial Bacteria Adhesion

Before a biofilm can begin to grow, the bacteria must adhere to a surface. The size scale of a bacteria (0.5-5 μm) allows bacteria to be treated as living colloids and be described, at least in part, (with some modifications) by the same theories that are used to describe colloidal interactions.[228] Bacterial-surface adhesion can be conceptualized into two steps. The first physicochemical step of the bacteria adhesion is reversible, while the second step is regarded as irreversible and time-dependent.[228,229] Reversible bacterial adhesion is driven by physicochemical interactions and can be modeled by classical colloidal DLVO theory. Given sufficient time, the second step of irreversible adhesion is dominated by specific binding interactions[228,230] The two-step framework fails to account for the observation that hydrophilic bacteria tend to adhere more to hydrophilic surfaces, while hydrophobic bacteria exhibit a preference for adhering to hydrophobic surfaces.[228] Thermodynamic approaches to model bacteria-surface interactions have been used to more accurately model these interactions, and an extended DLVO theory has been proposed that includes a term for hydrophilic/hydrophobic interations.[231,232] Once surface engagement occurs, extracellular organelles including, flagella and type IV pili are able to sense the surface.[233] Bacteria have been found to respond to many different properties of surfaces including surface roughness, hydrophobicity, surface chemistry and mechanical properties.[224,234–241]

4.1.3 Effects of Mechanical Proprieties on Bacteria-Surface Interactions

It has been previously shown that bacteria in static conditions are retained on surfaces depending the stiffness of the underlying substrate beneath the hydrogel coating. For PEG and Agar hydrogels, it has been reported that bacteria adhere less to thicker and softer hydrogels.[224,242] However this trend is reversed in the case of hydrophobic PDMS

(polydimethylsiloxane) surfaces with more bacteria irreversibly retained on softer PDMS surfaces.[225,243] In this study we examined PEG based hydrogels and brush surface coatings. This was done to compare the hydrogels to a model brush system and to study the influence of the mechanical properties. A PEG based system was chosen instead of a potentially more bio resistant zwitterion-based hydrogel system,[244] because of the wide spread commercial use of PEG and chemistry that allows us to compare the hydrogels with the previously characterized brush system.

4.2 Material and Methods

4.2.1 Materials

All chemicals were used as received. Irgacure 2959 was obtained from BASF (Ludwigshafen, Germany). 3-(trimethoxysilyl)propyl methacrylate and polyethylene glycol dimethacrylate (PEGDMA M_n = 750 Da) were purchased from Sigma-Aldrich (St. Louis, MO). Phosphate buffered saline with a Debye length of 1 nm and a pH of 7.4 (0.008 M Na_2HPO_4, 0.002 M KH_2PO_4 and 0.15 M NaCl) was used for all studies. PLL-PEG brush surfaces were prepared as previously described in Section 3.2.1.2.

4.2.2 Methods

4.2.2.1 PEG Surfaces

The PEG brush surfaces described and used in Chapter 3 were employed as a control surface in these studies. Polyethylene glycol dimethacrylate (PEG-DMA), hydrogels (Figure 36) were prepared on microscope slides substrates to fit the flow cell system based on established protocols.[245,246] Briefly, PEGDMA precursor solutions were prepared at 10 and 50 vol% PEGDMA (M_N 750) in PBS, and then degassed with nitrogen gas. 0.8 wt%

Irgacure 2959 was added as a UV initiator. Precursor solutions were pipetted onto a 3-(trimethoxysilyl)propyl methacrylate functionalized glass slide and sandwiched with a 24 × 40 mm glass coverslip to ensure uniform thickness during curing. The coverslip also helps limit oxygen exposure. Hydrogels were cured under UV light at 365 nm for 10 min or until cured. Coverslips were then removed, and hydrogels were swelled in PBS with a Debye length of 1 nm overnight. After swelling hydrogels were cut to fit the flow chamber using a sterile razor blade.

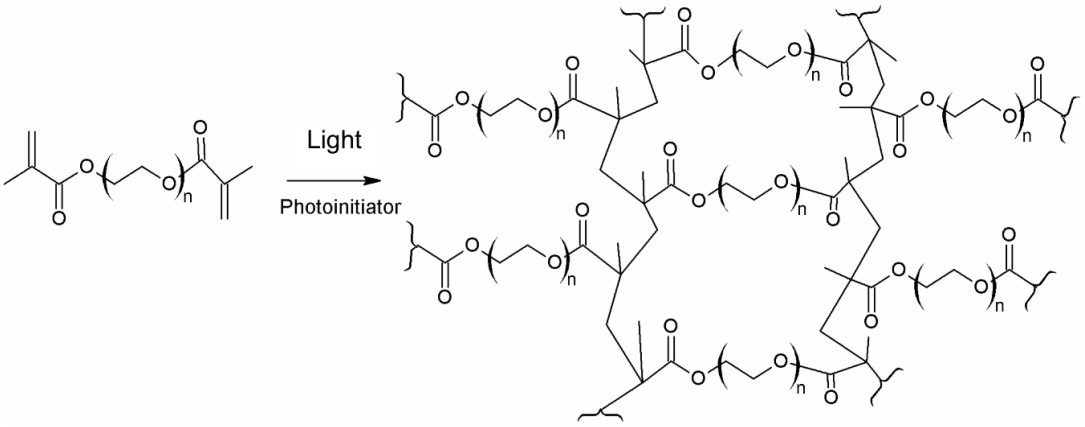

Figure 36. Schematic of PEG-DMA Hydrogel Structure. Each PEG-DMA monomer is able to react with 4 other monomers forming a hydrogel structure. For the system studied n =12-14. Figure modified from Bächström *et al*[247]

4.2.2.2 *E. coli* Strains

The *E. coli* strains described in Chapter 3 were also studied here. Briefly, *E. coli* BW25113, *E. coli* JW1881 and *E. coli* JW1879 were purchased from the Coli Genetic Stock Center (New Haven, CT). *E. coli* BW25113 (Parent Strain) is the parent stain of the Keio collection. *E. coli* JW1881 (No Flagella) is a modified strain with a genetic knockout of the flhD gene which is critical for the growth of flagella.[200] *E. coli* JW1879 is contains a genetic knockout of the motA gene that is necessary for proton-conducting in the flagella

motor, yet does not affect flagella synthesis.[201] A plasmid to upregulate the flagella growth was cloned into the isogenic mutant strains. In the No Flagella strain this plasmid restores and upregulates the motility of the bacteria, producing a Super Swimmer strain. By cloning the same plasmid into the motor mutant strain, flagella growth was upregulated without restoring motility. This strain called the "No Motor" strain has a similar number of flagella as the Super Swimmers, but lacked the ability to swim.

Bacteria were grown and washed using the same methods described in Chapter 3. Briefly bacteria were grown in overnight at 37°C in Luria- Bertani broth (LB) with antibiotics as required: no antibiotics for the Parent Strain, 50 µg/mL kanamycin for the No Flagella strain, or 50 µg/mL kanamycin and 100µg/mL carbenicillin for the Super Swimmer and No Motor strains. After overnight growth, liquid cultures were restarted using 200 µL of overnight culture in 5 mL of LB and same antibiotics. Additionally, in the restarted cultures 50 µL of 20% wt/vol arabinose solution was added to the Super Swimmer and No Motor Strains to induce the flhDC plasmid. These cultures were grown for 4 hours and harvested in the log growth phase. Bacteria cultures were then washed 3 times (centrifuged at 3500 rpm for 2 min) in pH 7.4 Phosphate Buffer Saline (PBS) (0.008 M Na_2HPO_4, 0.002 M KH_2PO_4, and 0.15 M NaCl) and resuspended in the same buffer at a concentration of approximately $1x10^8$ cells/mL. This concentration is below that were bacteria-bacteria interactions were found relevant at surfaces.[210] The concentration was determined using OD600 measurements.

4.2.2.3 *E. coli* - Surface Interaction Studies

Flow cell studies were conducted in the same laterally mounted flow chamber described in Section 3.2.2.5. Interactions between flowing bacteria and PEG surface coatings were conducted in a custom-built flow cell system in which the test surface comprised of one wall of the flow chamber. The microscope was oriented horizontally on an optical bench to view the test surface which was oriented perpendicular to the floor, to prevent gravity from affecting cell-surface interactions. The objective used for these studies was a Nikon Plan Fluor 20x objective with a numerical aperture of 0.5. This gave a depth of field of approximately 3.5 μm. Bacteria were flowed across the surface at a shear rate of 15 s^{-1} for approximately 10 minutes. The shear rate was held constant for all studies with the pump settings being adjusted to account for the thickness of the hydrogel. Data were recorded, at 30 fps on DVDs and analyzed at a rate of 5 fps using FFmpeg software. Manual tracking was done using *FIJI is just ImageJ*.

4.2.2.4 Cell Tracking and Engagement Analysis

Here, as in Chapter 3 we quantified dynamic adhesion in terms of dynamic cell engagements. We employed the same quantitative criteria as before that a cell must travel at a velocity of under 9.3 μm/s for a distance of at least 5 μm. 30 engaging cells were tracked in each 10 min run. On each surface three runs were completed with each bacteria strain. This method of tracking was identical to that employed in Chapter 3. Tracking cells on hydrogels was, however, more difficult than on brushes due to the requirement that the microscope be focused through the 100 μm thick hydrogel. The bubbles and defects in the body of the hydrogel made focusing more difficult. There was also a lot more background defects that made obtaining flux measurements not possible. While exact quantification

and confirmation was not possible, due to features in the hydrogel on the same order of magnitude as the bacteria the hydrogels, did not appear to permanently arrest bacteria.

4.3 Results and Discussion

4.3.1 PEG Coating Characterization

The material properties of the PEG surfaces used in this study are shown in Table 4. The PEG and hydrogel coatings used in this study were characterizations previously by Kolewe et al.[191]

Table 4. Properties of PEG based surfaces used in this study. Table adapted from Kolewe, et al.[191]

Name	PEG Content (wt%)	G' (kPa)	Mesh Size (nm)	Thickness	Fibrinogen Adsorption (mg/m^2)
PLL-PEG Brush	6	450	2.9 ± 0.2	15-17 nm	< 0.01
Stiff Hydrogel	46 ± 1	1300	1.0 ± 0.1	105 ± 5 μm	< 0.01
Soft Hydrogel	8.6 ± 2	9.5	2.7 ± 0.1	110 ± 5 μm	< 0.01

4.3.2 Number of Engagements

One easily quantified metric of bacteria-surface interactions was the number of engagements that each tracked bacteria, having at least one engagement, experiences over the course of the 260 μm field of view. This metric considers repeat surface encounters, when a bacterium has a second surface encounter after disengaging from the surface. Figure 37 compares the number of engagements per cell in the 260 μm field of view for cells which had at least one engagement. The average total number of surface engagements per cell within the field of view is shown in Table 5.

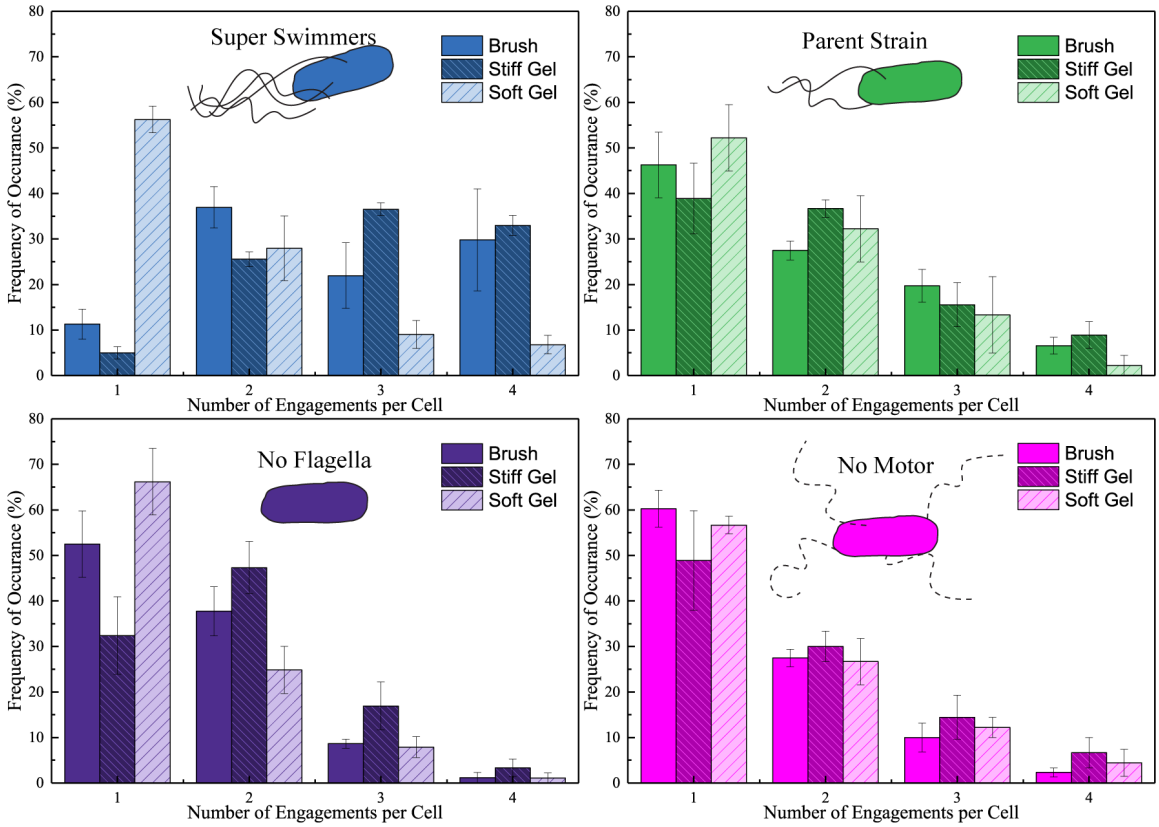

Figure 37. Number of Engagements for each bacterium on various surfaces, for cells having at least one engagement

Table 5. Average number of surface engagements per cell in the 260 μm field of view.

	Brush	Stiff Hydrogel	Soft Hydrogel
Super Swimmers	2.8	3.0	1.6
Parent Strain	1.9	2.0	1.7
No Flagella	1.5	1.9	1.4
No Motors	1.6	1.8	1.6

The Super Swimmers exhibited interesting near-surface dynamics in flow, that were qualitatively different from the behaviors of the other cells and highly statistically significant. On both the brush and the stiff hydrogel the Super Swimmer cells (<85%) that engaged the surface returned to the surface for at least one additional engagement. Often

engaging Super Swimmer cells returned to the surface for two or three additional engagements within the 260 μm field of view. The tendency for Super Swimmer Cells to return to the surface was not observed on the soft hydrogel surfaces. Indeed, the Super Swimmer cells had the same increasingly small tendency to return to the soft hydrogel as the other strains, shown in Figure 38.

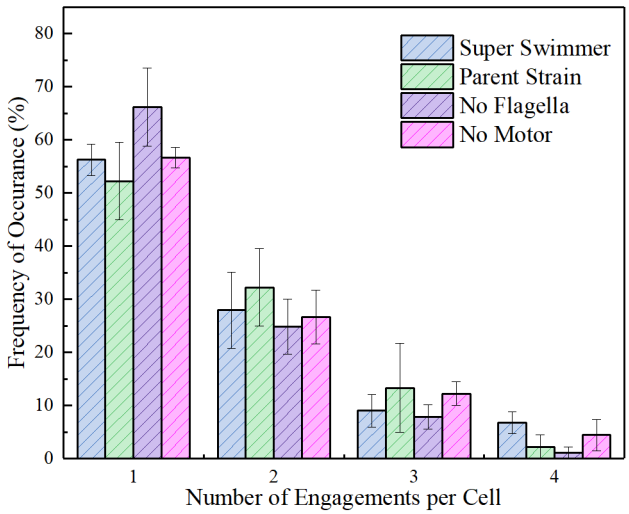

Figure 38. Number of Engagements per cell in the 260 μm field of view, for different bacterial strains with the surface of a soft hydrogel.

4.3.3 Engagement Velocity

Engaged bacterial cells were observed to travel along the surface at relatively constant velocities (when compared to the velocity of bacteria in the bulk). The particular PEG surface, hydrogels or brush, had only a modest impact on the velocity of engaged bacteria for the Parent Strain, No Motor and No Flagella strains. Differences between the travel velocities of engaged non-motile cells likely arose from variations in the hydrodynamic cell size, the ability of cells to approach the surface and occupy slow-moving streamlines, viscous drag from cells closest to the PEG coatings, and reversible physicochemical bonds between cells and coating molecules. These factors appear to have a similar impact on the

No Flagella, Parent Strain, and No Motor cells. Compared with cells of the other strains, Super Swimmers exhibited slower engagement velocities, (though all were positive.) All Super Swimmer cells traveled in the direction of the flow. For the Super Swimmers however the brush surfaces produced a significantly lower engagement velocity than both of the hydrogels. The lower velocity is likely due to swimming bringing the bacteria closer to the surface. At the shear rates studied we do not observe bacteria traveling upstream; however, the bacteria may still be swimming against the flow, just not strongly enough to overcome the velocity of the fluid. The ability of the bacteria to exhibit this behavior may be limited on the hydrogel surfaces.

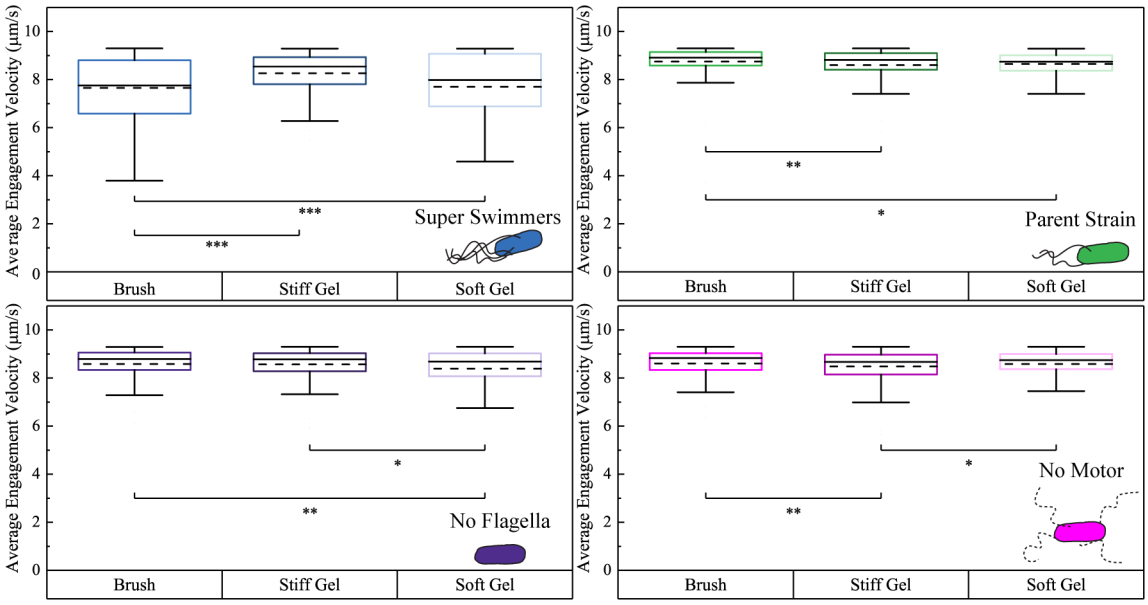

Figure 39. Engagement velocity distributions for each bacterium on the different surfaces. Includes all engagements used in other measures including short engagements. All differences between surfaces for a given bacteria, are not significant unless marked. *** indicates $p<0.01$, ** indicates $p<0.05$ and * indicates $p<0.1$ Solid lines represent median values and dashed lines represent averages.

4.3.4 Length and Duration of Individual Engagements

Engaged cells travel along the surface for some time, before they disengage. Each cell therefore is in contact with a particular length or distance of surface during its engagement

and further, there is a surface residence time, albeit dynamic, associated with each engagement. The distribution of travel distances per individual cell engagements for each strain is shown in Figure 40. The average distance traveled and residence time per engagement for each strain is summarized in Table 6.

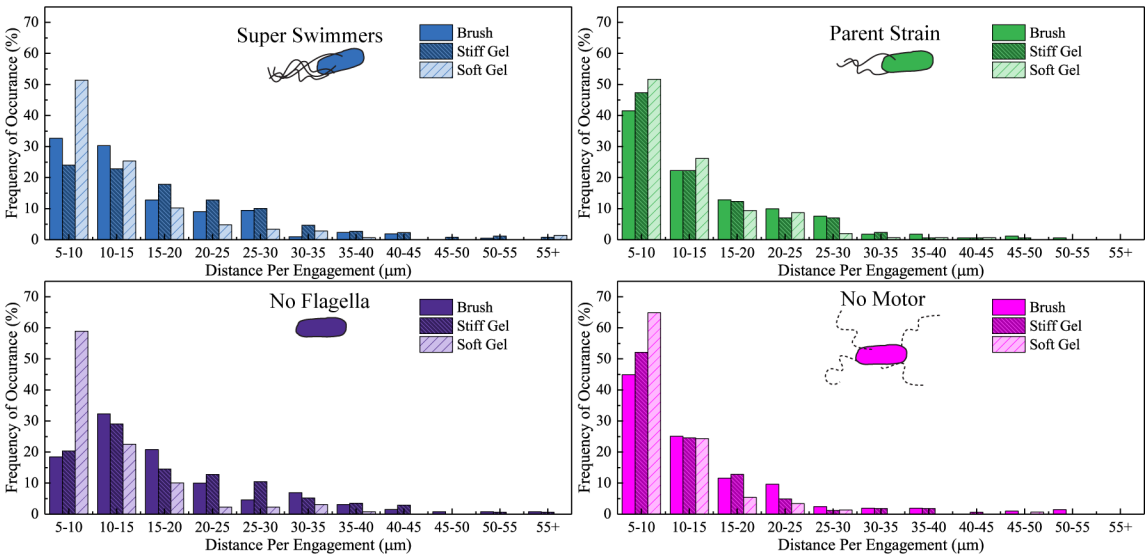

Figure 40. Distance Per Engagement distributions for each type of bacteria-surface interactions

Table 6. Average distance and residence time per engagement for bacteria on each surface.

	Brush		Stiff Hydrogel		Soft Hydrogel	
	Distance (μm)	Residence Time (s)	Distance (μm)	Residence Time (s)	Distance (μm)	Residence Time (s)
Super Swimmers	15.0	2.05	19.0	2.30	12.7	1.62
Parent Strain	14.8	1.71	13.8	1.66	11.6	1.36
No Flagella	16.7	2.02	18.9	2.19	11.1	1.38
No Motors	14.4	1.59	11.6	1.38	9.7	1.12

*Error is not given due to full distributions being showed in Figure 40 and Figure 41

It was found that, for all strains, the distribution of engagement distances of cells on the stiff hydrogels were similar to those on the brush surfaces, however there are slight statistical differences between these two surfaces. For both the Super Swimmers and the

No Flagella bacteria the engagements with the stiff hydrogel surface are of statistically greater duration than on the brush. This could be due to the greater G' of the stiff hydrogel than the brush surface. Additionally, it could be due to interactions with unreacted methacrylate groups present on the surface of the hydrogel, though the hydrogels did not adsorb fibrinogen from solution, which suggests that these groups were not accessible to bacteria in solution. This trend however is reversed for the Parent Strain and the No Motor strain with the shorter durations of engagements on the stiff hydrogel then the brush. This result suggests that the flagella interactions that cause a steric kick from the surface are increased on the stiff hydrogel surface as these steric kicks are not present with the No Flagella strain and are not believed to be the main disengagement mechanism for the Super Swimming strain. The steric kicks come from the flagella on the bacteria, not the surface, but may be more effective on some surfaces compared to others.

Additionally, similar comparisons can be made for the residence time per engagement. For many cells in a run on a given surface, and for three runs with each surface, distributions engagement residence times are shown in Figure 41. Similar to the travel distance of engagement the Super Swimmers and the No Flagella exhibit a greater residence time per engagement on the stiff hydrogel compared to the brush and soft hydrogel while the No Motor and Parent Strain show a shorter residence time per engagement on the stiff hydrogel compared to the brush but a longer time compared to the soft hydrogel. The soft hydrogel has the shortest residence times per engagement for all the strains.

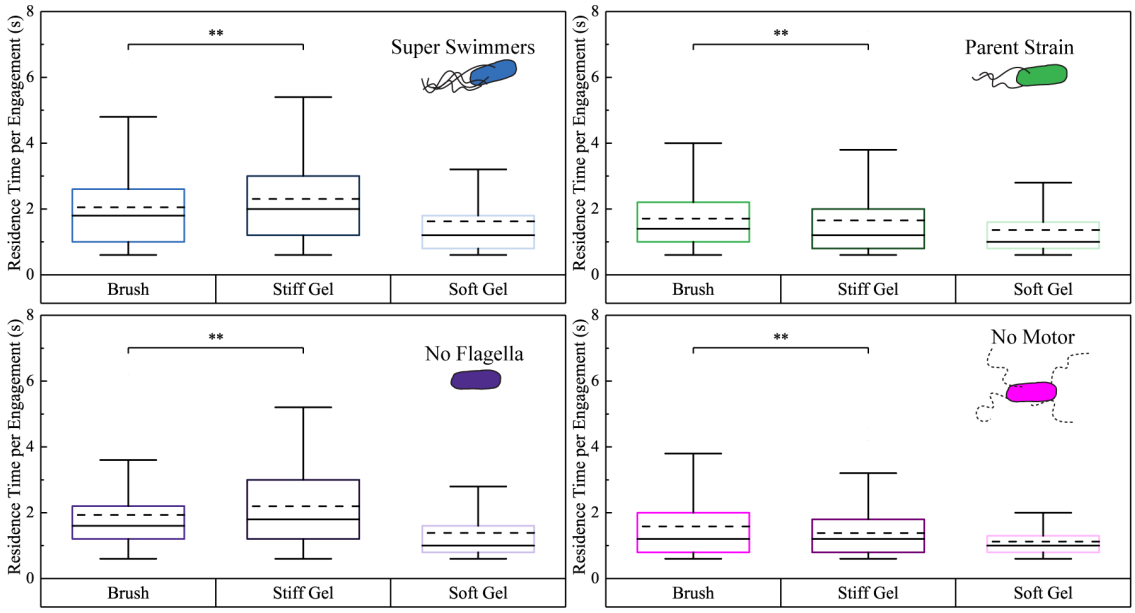

Figure 41. Residence Time per engagement for individual cells. All differences between materials are *** ($p<0.01$) unless noted. Solid line represents the average residence time per engagement. Dashed line indicates the median residence time per engagement.

The measures of distance and residence time per engagement are very closely related. For both of these measures the soft hydrogel surface significantly reduces the differences between strains. A comparison of the engagement lengths and residence times strains on the soft hydrogel (seen in Figure 42 and Figure 43) shows very similar lengths (in distance and time) for all the strains with the No Motors having a statistically shorter travel distance and time then all the other strains which are statistically the same.

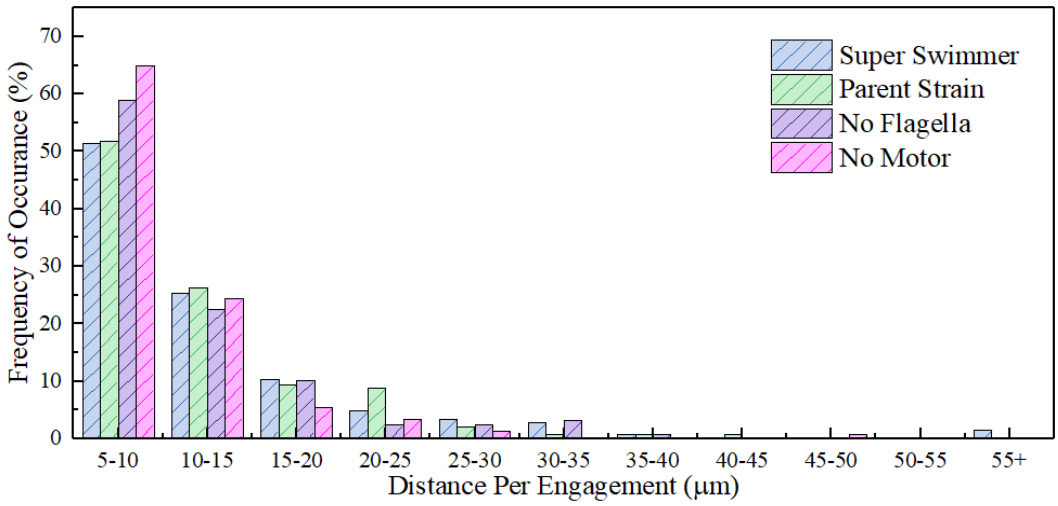

Figure 42. Distance per Engagement for all strains on the soft hydrogel surface

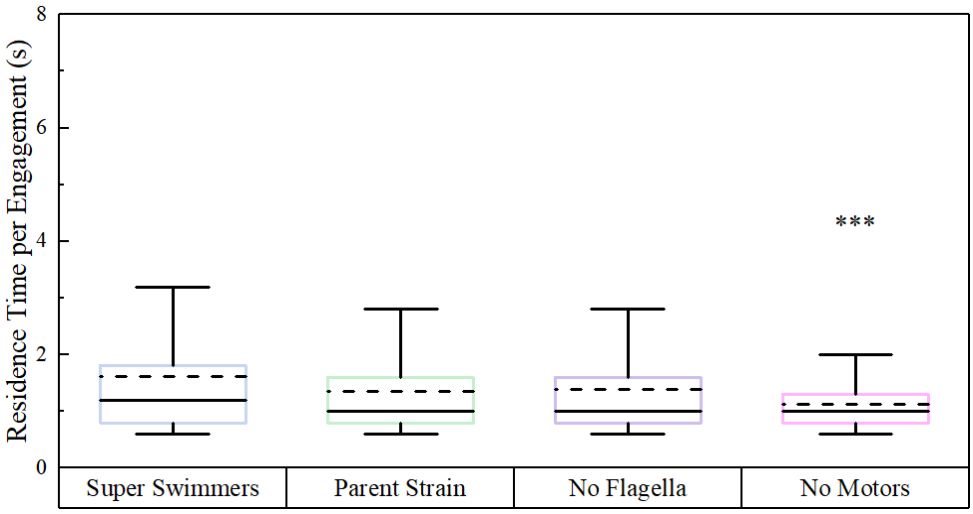

Figure 43. Residence time per engagement for all bacteria on the soft hydrogel surface. There are no statistical differences between the Super Swimmers, Parent Strain and No Flagella strains. The No Motors are different than the other 3 strains. *** indicated $p<0.01$

Overall the differences in residence time and, ultimately the travel distance, are due to differences in the frequencies of events that produce escape. In order for an escape event to occur and to end the engagement, some sort of random event must occur to trigger an escape event. Individual cells from all of the bacteria strains can have a Brownian kick that either breaks a physical bond or displaces the cell from the region nearest the surface. The

bacteria having flagella (whether motile or not) can also have a steric kick involving one of its flagella and, finally, the Super Swimmers can also have a flagella repulsion that is triggered by the unbundling of the flagella or a fluctuation in bacterial orientation that allows the flagella bunding to interact repulsively with the coating. All of these mechanisms are possibly increased on the soft hydrogel surface due to differences in mechanical interactions between the flagella and the softer substrate. Due to the shorter engagement distances and residence times for all the strains on the soft hydrogel, it may be the case that the soft hydrogel produces weaker dynamic bonds with the bacterial cells. This might increase the effectiveness of Brownian fluctuations or steric events to end a cell-surface engagement.

4.3.5 Overall Residence Time

The overall residence time is shown in Figure 44. This quantity is the total time that a cell was in dynamic contact with the surface while in the 260 μm window of observation and is the sum of the residence times for all the engagements of that cell while it was visible. Figure 10 shows that for all four strains, cells have the shortest overall residence times on the soft hydrogel surfaces compared with the brush or stiff hydrogel surface. For the Parent Strain and the No Motor strains there is no difference in the overall residence times observed on the stiff hydrogel and the brush. The Super Swimmers and the No Flagella strains however have a longer overall residence time on the stiff hydrogel compared with that on the brush.

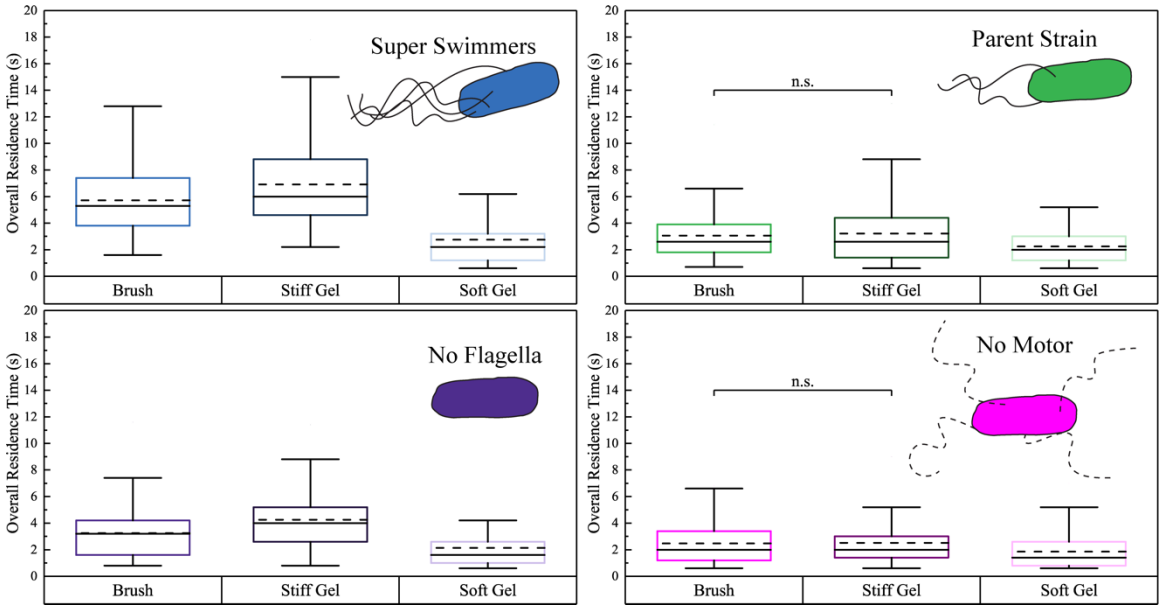

Figure 44. Overall residence time within the 260 μm field of view for individual bacteria cells. Solid lines represent the mean of the distributions and the dashed lines represent the median. For each bacteria and surface combination 3 runs of 30 cells per run are tracked. All are $p<0.01$ unless indicated.

Similar to the other metrics studied, in terms of the overall residence time the soft hydrogel surface significantly reduces the differences between strains. This is highlighted in Figure 45. The only statically significant difference in the strains on the soft hydrogel surface is between the Super Swimmers and the No Motor strains. On the brush surface (Figure 34) there were statistical differences between all sets of strains except the Parent Strain and No Flagella strain.

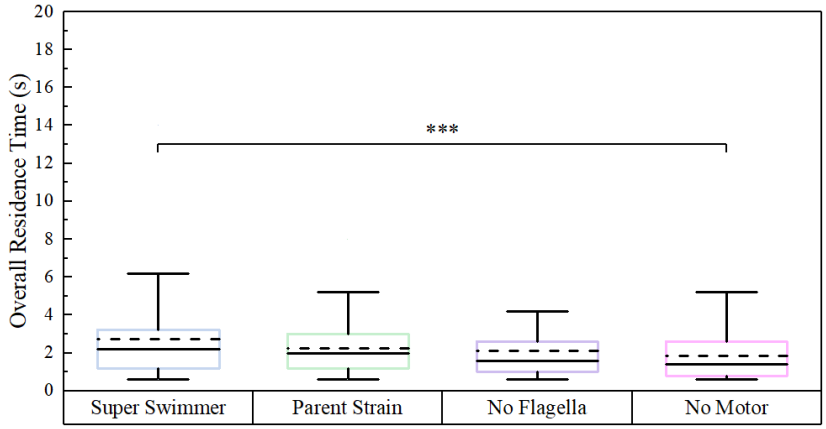

Figure 45. Overall residence time distributions within the 260 µm field of view for individual bacteria cells on the soft hydrogel. Solid lines represent the mean and the dashed lines represent the median. The only significant difference is between the Super Swimmers and the No Motor Strains. *** indicates $p < 0.01$

4.4 Conclusions

The interactions between the bacteria and the surface in the presence of flow depend on the motility and morphology of the bacteria and on the physical and chemical properties of the surface. Overall the body of the bacterium will stay engaged to the surface until it undergoes some sort of critical fluctuation caused by a steric or diffusive kick. These kicks are often caused by the presence of flagella, when they either create a steric boundary that prevents the body of the bacterium from remaining engaged with the surface or when they unbundle. When a bacterium is actively swimming the hydrodynamic forces keep it near the surface. The study in this chapter showed that the surface also plays a role in these interactions. On the brush and stiff hydrogel surfaces the differences in bacteria strains are significant and overall longer both in time and distance than on the soft hydrogel surface. On the soft hydrogel surfaces the effect of the motility and the morphology of the bacteria is significantly reduced with all of the strains having fewer and shorter interactions.

CHAPTER 5

ROD SHAPED MICROPARTICLES DELIVER MORE MATERIAL TO SURFACE THAN SPHERICAL MICROPARTICLES

The work in this chapter was done in collaboration with Aiste Balciunaite. She synthesized the silica spheres and 2 of the 4 rod samples and ran the majority of the flow cell runs. Both of us assisted with data analysis and intellectual contributions were shared.

5.1 Introduction

5.1.1 Why study rods?

The behavior of particles in flow is a topic of key interest within the medical field, relevant to questions spanning from how best to prevent bacteria adhering in small tubes such as catheters to targeting drug delivery. Chapter 3 focused exclusively on spherical particles. In practice, though, many particles (including the *E. coli* studied in Chapter 4 and 5) both in biological and industrial systems are not spherical. Recent literature has suggested that particle shape is an exploitable factor in the design of particles for drug delivery.[248,249] The motion of non-spherical particles in flow can be significantly more complex than spherical particles due to tumbling behaviors. These behaviors could potentially be used in controlling the distribution of drug carrying particles within the body.[90] Carrier shape has also been shown to affect the ability of a particle to be internalized into cells.[250] These shape effects have led to an increase in different shaped particles being studied for drug delivery applications.[94,251,252]

In addition to drug delivery applications, there are situations where it is necessary to understand the transport behavior of non-spherical colloids. In water filtration many contaminants are non-spherical in shape. These contaminants such as bacteria cells, polymers or clay aggregates, and fiber fragments such as asbestos are often modeled as spheres of an effective hydrodynamic size, though these models have been found ineffective for describing the behaviors, such as the transport and capture of these types of particles.[253–256]

5.1.2 Rods in Drug Delivery Applications

Two significant challenges of drug delivery are avoiding degradation of the drug molecules within the body and the selective delivery of a drug to target cells. Encasing drugs in microparticle carriers has been shown to be a potential solution to these problems,[257] and additionally makes it possible to deliver hydrophobic drugs.[258] Rod shaped particle carriers have been shown to have advantages over spherical microcarriers. For instance, elongated rod-shaped particles are less likely to trigger an immune system response, leading to a higher proportion of the drug being able to reach the targeted cells instead of being cleared from the bloodstream.[94,259]

Additionally, the two different length scales on rod or ellipsoid particles, one short and one long, allow non-spherical particles to better diffuse through small spaces, such as pores between cells.[259] This feature has led to recent studies that suggest that non-spherical particles have different biodistribution behavior than spherical particles.[96,259,260] These behavioral differences could be used when designing a delivery package to target a specific cell type, which could greatly increase the efficacy of a drug.

Overall the largest advantage of non-spherical particles is expected to be their adhesion as compared to spherical particles. Oblate spheroids (M&M shaped particles) of the same volume as a sphere are predicted to adhere more strongly to a surface, allowing for delivery of a larger volume of drug.[261] Multiple studies have predicted that non-spherical particles such as rods and disks adhere to a surface from blood flow at a higher rate than spheres.[86–88,261]

One of the greatest challenges in the design of non-spherical particles for drug delivery applications is the lack of systematic research showing the differences between spherical and rod-shaped particles in flow. Due to their complex flow behaviors rods pose a potential risk for use that must be further studied. For example Doshi et al. showed the behavior of rod-shaped particles in microvasculature with bifurcation and found that at the point of bifurcation rod shaped particles were more likely than spherical particles to both stick to the wall and each other, which could be harmful in microvascular networks.[97]

In addition to the flow behavior of the microparticles it is important to consider the strength of adhesion when designing potential drug carriers. A certain amount of time may be necessary for the drug to be able to diffuse out of the drug carrier into the desired target or to be engulfed by a cell. For different drugs, longer or short adhesion times could be advantageous, which could be fine-tuned based on the shape of the drug carrier and the purpose of the drug. Decuzzi and Ferrari,[261] showed that for a given ellipsoidal aspect ratio there is an optimal particle volume for adhesive strength. Additionally, they predict that a oblate spheroid with an aspect ratio of 2 and the same probability of adhesion as a 500 nm sphere would have about 50 times the particle volume.[261] The use of a drug carrier with a

larger volume results in the delivery of a larger quantity of drugs, another potential advantage to the use of non-spherical particles as drug carriers.

Current research has mainly focused on the behavior of spherical particles in flow. Due to their symmetric nature they are much easier to model. It has been found that the diameter of spherical particles has an effect on their adhesion, with smaller particles adhering to a surface via receptor -ligand mediated adhesion, more effectively than larger particles in the presence of high shear rates. This particle size effect is diminished at lower shear rates. Additionally, it was found that once adhered, larger particles require a lower shear rate to dislodge from the surface.[262] On surfaces with low adhesive properties, spherical particles may roll on the surface, or more particles escape than permanently adhere to the surface.[49] No similar conclusions exist for synthetic rod-shaped particles, (rod shaped *E. coli* have shown rolling behavior caused by shear-activated FimH catch-bonds[263]) and the studies that have been conducted are varied and inconsistent with their experimental conditions, making direct comparison impossible.

5.2 Materials and Methods

5.2.1 Materials

All materials were used as purchased. 1-pentanol, polyvinylpyrrolidone (PVP) (MW 40,000), Sodium Citrate dihydrate and tetra-ethyl orthosilicate (TEOS) were purchased from Sigma Aldrich. Ammonia Solution 25% in Water was purchased from EMD Millipore. 200 proof ethanol was purchased from Fisher Scientific. Poly-L-lysine hydrobromide (PLL), having nominal molecular weight of 15,000 -30,000 g/mol, was purchased from Sigma Aldrich, Phosphate buffer with a pH of 7.4 (0.008 M Na_2HPO_4 and

0.002 M KH_2PO_4), having a Debye length of κ^{-1} = 2 nm was employed in most studies unless otherwise noted. Variations in ionic strength, having different Debye lengths, were achieved either by diluting this buffer with deionized (DI) water or by adding buffer salts at the same ratio of Na_2HPO_4 and KH_2PO_4.

5.2.2 Particle Synthesis

5.2.2.1 Synthesis of Silica Rods

Rod shaped silica particles were synthesized using the methods described by Kuijk et al[264,265]. The approach has been used by additional groups to produce size and aspect ratio controlled rod-shaped silica particles.[266–272] Briefly, water, ethanol, and ammonia were added to a solution of (PVP) in 1-pentanol. Recipes for each rod sample are given in Table 7. Particle names (MKS1, MKS2, AB6 and AB4) correspond to who completed the synthesis (MKS: Molly Shave, AB: Aiste Balciunaite) and order of particle synthesis and don't correspond to particle characterization or size. Sodium citrate was then added which forms emulsion droplets in the solution. When tetra-ethyl orthosilicate (TEOS) was then added to the solution silica rods grow from the droplets. Additional TEOS additions increase the length of the rods while having little to no effect on the diameter. After initial synthesis particles were centrifuged at 1500g for 1 hr to remove particles from reaction solution. Particles were then dispersed in ethanol using vortexing and sonication. 2 additional washes, centrifuging at 1500g for 15 min, were done dispersing in ethanol followed by 3 washes in DI Water and finally in DI water. After these high-speed washes, additional washes were performed at lower speeds to reduced polydispersity. 700g for 15min was used as a starting point for these washes. The speed was then lowered every 1-

2 washes as long as a distinct pellet formed. Polydispersity was checked during this process by SEM, an example of this washing progress is shown in Figure 46.

Table 7. Details of Rod Synthesis

	Sample Name	MKS1	MKS2	AB6	AB4
	Final Aspect Ratio	1.35	1.63	2.48	3.17
Core Synthesis	1- Pentanol (mL)	750	750	250	250
	PVP (g)	75	75	25	25
	Ethanol (mL)	75	75	25	25
	Ammonia (mL)	20.1	20.1	6.7	6.7
	DI Water (mL)	21	21	7	7
	0.18 M Sodium Citrate Solution (mL)	5	5	1.2	1.2
	TEOS (mL) (per addition)	7.5	7.5	2.5	3
	Number of TEOS Additions	1	3	1	2
	Number of Washes	9	9	10	13
Shell Synthesis	Ethanol (mL)	100	100	125	200
	Ammonia (mL)	12	12	15	24
	Water	10	10	12.5	20
	TEOS (mL)	1	1	0.25	1
	Number of TEOS Additions	2	4	1	1
	Number of Washes	30	35	20	40

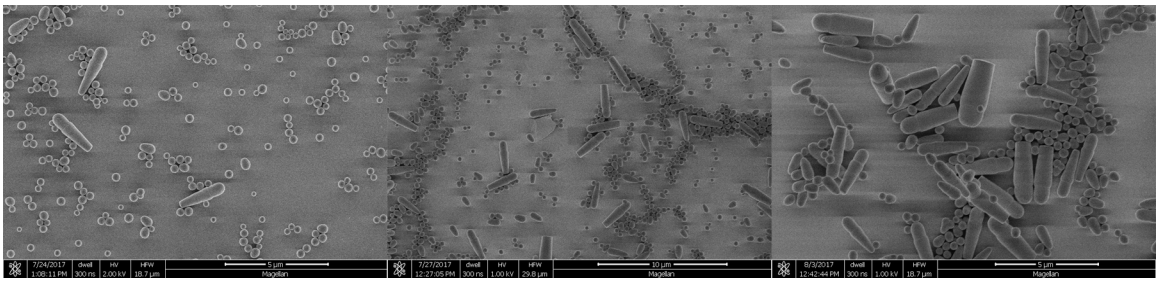

Figure 46. Rods with final (after shell) aspect ratio of 3.17 at different stages of core cleaning process. Washes were continued to remove small particles prior to core synthesis

After core washing, shells of Stöber silica were then grown on the outsides of the rods to control the surface chemistry and eliminate the porosity caused by the presence of PVP in the rods[273]. Briefly, cores were dispersed in ethanol and placed on stir plate. Ammonia solution and water were added to solution. TEOS was added to solution while stirring, for

a thicker Stöber silica layer additional TEOS was added after a period of at least 2 hrs. The same washing process was followed after the shell synthesis to remove small particles and improve polydispersity.

5.2.2.2 Synthesis of Silica Spheres

Spheres were synthesized using a modified Stöber method. Briefly, ethanol, water and ammonia were mixed and placed on a stir plate. TEOS was then added while stirring. For larger particles additional aliquots of TEOS and DI water were added. Details are shown in Table 8. Particles were then washed by centrifuging at 700 g for 15 min, dispersing in ethanol 3 times, followed by 3 washes in DI Water and 3 washes in pH 4 Phosphate Buffer with a Debye length of 4 nm (0.0018 M Na_2HPO_4, 0.00046 M KH_2PO_4). Spheres are named by their particle diameter.

Table 8. Recipes for silica spheres

	Particle Diameter (nm)	**565**	**720**	**965**
Initial Synthesis	Ethanol (mL)	147.6	147.6	147.6
	Ammonia (mL)	22.8	22.8	22.8
	DI Water (mL)	18.4	18.4	18.4
	Initial TEOS (mL)	11.2	11.2	11.2
TEOS Additions	Number of TEOS Additions	0	1	4
	TEOS Per addition (mL)	N/A	11.2	11.2
	DI Water per TEOS Addition (mL)	N/A	1.8	1.8

5.2.3 Particle Characterization

Prior to study in the flow cell both the rod and spherical particles were characterized to determine size and surface characteristics of the samples. Scanning Electron Microscopy

(SEM) (FEI Magellan 400 XHR-SEM) and Dynamic Light Scattering (DLS) (Malvern Zetasizer nano) were employed for size analysis and Zeta potential to confirm that surface chemistry is similar to most silica spheres.

5.2.3.1 Rod Imaging and Sizing

Samples of rod and sphere –shaped particles were suspended in DI water and the solution was dropped on to cut silicon wafers at approximately 50°C and allowed to dry creating a monolayer of particles. The concentration of particles was adjusted based on sample but always less than 500 ppm. If samples were too concentrated to produce a monolayer of particles, they were further diluted. The dried samples were mounted on to SEM stubs and sputter coated (Sputter Coater) in gold for 200 seconds prior to imaging with FEI Magellan 400 XHR-SEM.

Rod particle dimensions were determined by analysis of SEM Micrographs using FIJI is Just ImageJ software. Only images in which rods lie flat on the wafer surface were included quantified. All particles within a given image were measured unless particles in portions of images were clearly stacked or standing upright.

5.2.3.2 DLS/Zeta Potential

Particles were dispersed in phosphate buffer (0.008 M Na_2HPO_4, 0.002 M KH_2PO_4) at concentrations of approximately 100ppm. Concentration was varied for optimal light scattering in instrument. Samples were tested using a Malvern Zetasizer Nano at 25°C.

5.2.4 Surface Adhesion Experiments

Particle capture was studied using the same flow cell system previously described in Chapter 2. In order to functionalize the surfaces for testing glass slides (Fishers Finest)

were etched overnight concentrated sulfuric acid. This treatment has been shown to produce a pure silica surface.[163] Slides were functionalized by flowing a 100 ppm PLL solution in pH 7.4 phosphate buffer (0.008 M Na_2HPO_4 and 0.002 M KH_2PO_4) over the glass surface at a shear rate of 5 s^{-1} for 10 minutes followed by 10 minutes of buffer. The flow cell was not opened or exposed to air between adsorption of the PLL and particles on the surface. The functionalization of the surface was done with a peristaltic pump while adhesion studies were done using a syringe pump. Process flow diagrams of the flow cell set ups are shown in Figure 47. The entry line before the flow cell was changed for each sample to ensure that only the particle sample of interest was present in the flow cell. For each run, first the surface was functionalized with PLL. Then, after the PLL was fully rinsed from the surface, a particle solution was introduced at a shear rate of 22s^{-1} for approximately 10 min. Particle interactions were recorded on DVDs using optical microscopy.

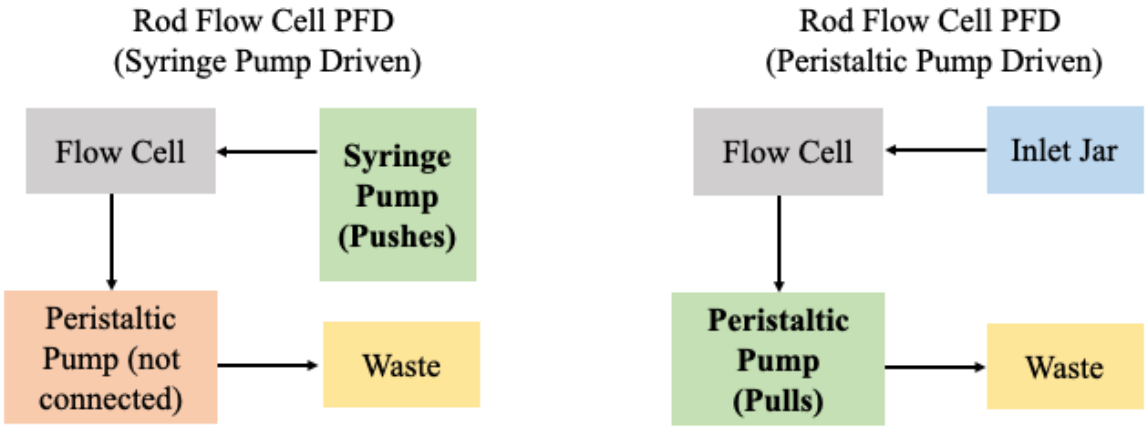

Figure 47. Process Flow Diagrams of systems used in this study. The Syringe pump driven flow was used during the adhesion studies and the peristaltic pump set up is used for the functionalization the chamber and the washing after runs.

The majority of the studies employed a 20x phase contrast objective. In some cases (mainly with the largest particles) a 10x phase contrast objective was used due to the slower

accumulation rate of particles, warranting a larger field of view to collect relevant statistics. Additionally, orientation studies employed a Nikon Plan Flour 40x objective, capturing photos of adhered particles after the completion of the run. The field of view for the, 10x objective is (480 μm by 340 μm), 20x is (260 μm by 177 μm) and 40x objective is (120 μm by 90 μm). Video data of particle adhesion was fist exported into stacks of TIFF files using FFmpeg software. These image stacks were analyzed using manual tracking in *FIJI is just ImageJ*. Orientation was determined by measuring the angle of particles adhered on surface after rinsing.

5.3 Results and Discussion

5.3.1 Particle Characterization

Particle characterization established which samples fell within acceptable limits of polydispersity and surface chemistry for use in particle capture experiments. In addition to the four rod samples summarized in Table 9, 2 additional rod samples were synthesized and determined to be too polydisperse for current study, and a third longer rod sample was saved for potential future work on the near surface orientation behavior of large rods.

Table 9. Characterization of Rod and Spherical Particles.

	Aspect Ratio	Diameter by SEM (nm)	Length by SEM (nm)	Hydrodynamic Diameter by DLS (nm)	Zeta Potential (mV)
MKS1	1.35 ± 0.09	755 ± 55	1023 ± 40	799 ± 15	-56.1 ± 2.4
MKS2	1.63 ± 0.19	836 ± 70	1364 ± 200	972 ± 60*	-55.9 ± 1.8
AB6	2.48 ± 0.25	555 ± 81	1362 ± 117	490 ± 2.2*	--
AB4	3.17 ± 0.32	836 ± 125	2639 ± 345	854.5 ± 106*	--
565	Sphere	565 ± 17		--	-64.9 ± 3
720	Sphere	720 ± 32		--	-72.9 ± 4
965	Sphere	965 ± 40		--	--

* next to value indicates that results did not meet instrument quality criteria.

5.3.1.1 Particle SEM and Sizing

Figure 48A shows example SEM micrographs from the 4 samples of rod-shaped particles. Their dimensions and aspect ratios are summarized in Table 9. Sizing statistics for these rod samples is seen in Figure 48B. Additionally 3 samples of Stöber silica spheres of varied diameter were also synthesized to employ as control. The SEM and size distributions of these samples and the control GelTech particles studied in Chapter 2 are shown in Figure 49 and included in Table 9.

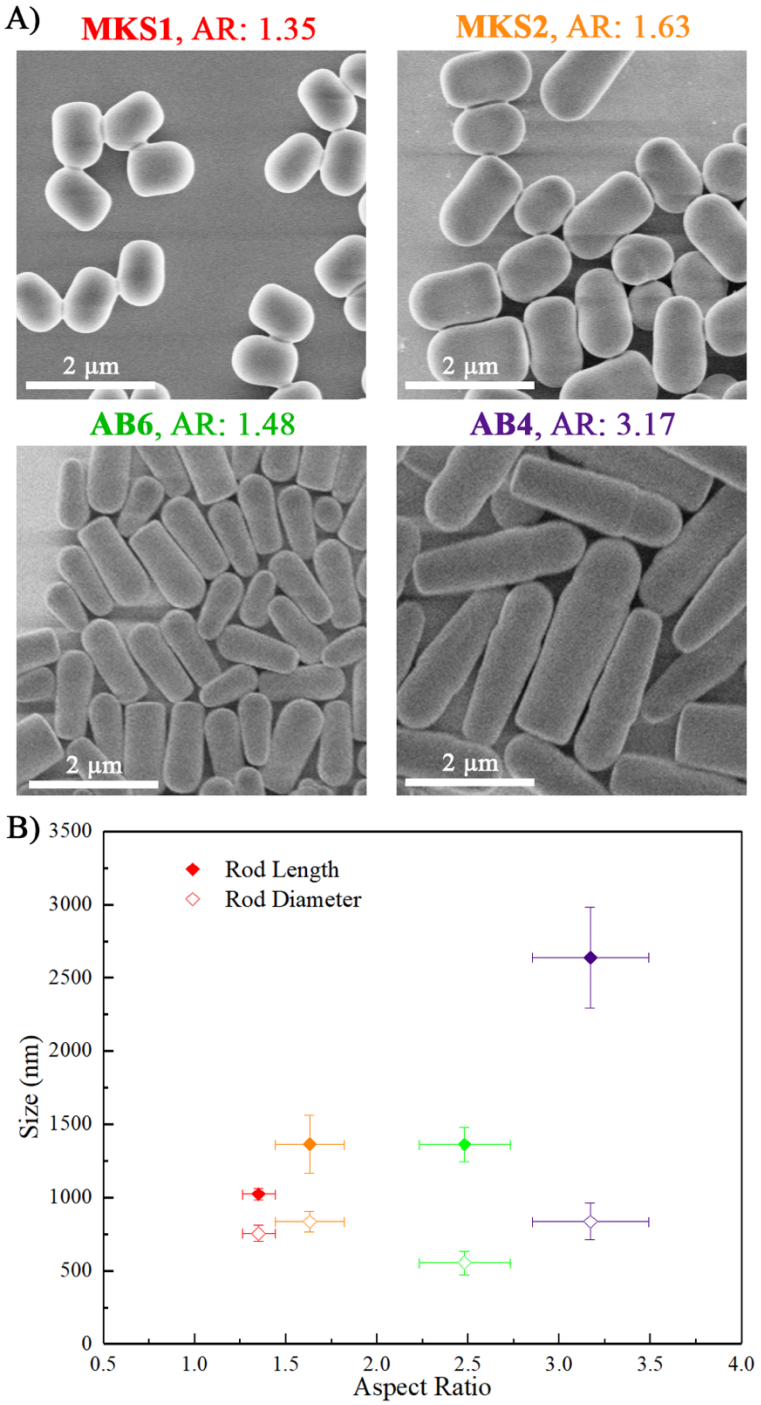

Figure 48. Rod SEM and Sizing. A) SEM of each particle sample, B) Plot of particle size vs aspect ratio. Colors on graph correspond with colors of text on SEM labels

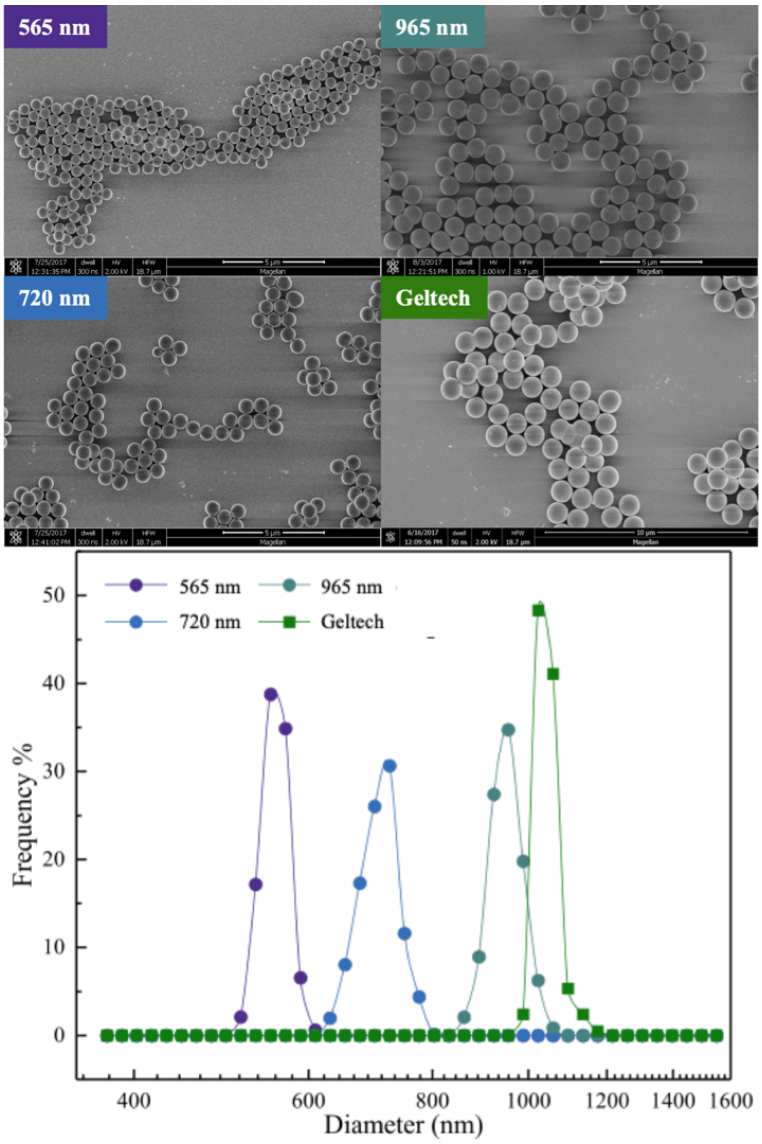

Figure 49. SEM and size characterization of silica spheres. All particles are imaged at same size scale.

5.3.1.2 Dynamic Light Scattering and Zeta Potential

Due to instrument limitations, zeta potential measurements could be completed on only the two rod samples with the smallest aspect ratio. Sizing and zeta potential (both done in phosphate buffer having a Debye length of 2nm) data for rod samples used in flow cell studies can be found in Table 9.

5.3.1.3 Particle Diffusion Coefficients

Due to the instrument imprecision in determining the hydrodynamic diameter and diffusion coefficient of the rod-shaped particles we used two models developed by Ortega and Garcia de la Torre.[218] The model for rod shaped particles with aspect ratios between 2 and 20 is shown in Equation 5.1 and 5.2

$$D_t = \frac{1}{3}\frac{kT(\ln p + C_t)}{\pi\eta_0 L} \quad (5.1)^{218}$$

$$C_t = 0.312 + \frac{0.565}{p} - \frac{0.100}{p^2} \quad (5.2)^{218}$$

Where D_t is the translational, diffusion coefficient, p is the aspect ratio, L is the particle length, $\eta_0$is the solvent viscosity and C_t is an aspect ratio constant described in Equation 5.2, because of the mathematical approximations used in deriving this model it is accurate within the limits of aspect ratio 2-20. Ortega and Garcia de la Torre[218] also use a friction coefficient model, in Equation 5.3, that applies for aspect ratios greater than 0.1 (aspect ratios below 1 are disk shaped particles).

$$D_t = \frac{kT}{f} \quad (5.3)^{218}$$

Where f the translational friction coefficient derived from Equations 5.4 and 5.5.

$$\frac{f}{f_0} = 1.009 + 1.395 \times 10^{-2} \ln p + 7.88 \times 10^{-2}(\ln p)^2 + 6.040 \times 10^{-3}(\ln p)^3 \quad (5.4)^{218}$$

$$f_0 = 6\pi\eta_0 L\left(\frac{3}{16}p^2\right)^{1/3} \quad (5.5)^{218}$$

Using these two methods of calculations on the rod samples studied the calculated diffusion coefficients are seen in Table 10.

Table 10. Diffusion Coefficients as calculated by Calculation 1 (Equations 5.1 and 5.2) and Calculation 2 (Equations 5.3-5.5).

				Calculation 1		Calculation 2	
	Aspect Ratio	Length (nm)	Diameter (nm)	Diffusion coefficient (m^2/s)	Hydrodynamic diameter (nm)	Diffusion coefficient (m^2/s)	Hydrodynamic diameter (nm)
MKS1	1.35	1023	755	4.11 E-13	1046	4.40 E-13	976
MKS2	1.63	1364	836	3.49 E-13	1229	3.68 E-13	1167
AB6	2.48	1362	555	4.49 E-13	967	4.60 E-13	934
AB4	3.17	2639	836	2.65 E-13	1619	2.69 E-13	1598

* Hydrodynamic diameter assumes a spherical particle following the Stokes-Einstein Equation.

5.3.1.4 Determination of Stock Particle Concentration

After synthesis particles were not dried prior to testing. Two concentration values, mass and number of particles, were used to describe the concentration of the stock solutions. The first method is by weight, where the mass concentration of solution was determined by weighing a sample before and after drying. The second method, particle number concentration, was determined by flow cytometry. Stock solutions were first diluted 1:1000 in DI water, then 200uL of diluted sample was mixed with 50uL of CountBright Absolute Counting Beads, for flow cytometry (Thermo Fisher). This dispersion was then tested using flow cytometry (BD DUAL LSRFortessa, 5 Excitation Lasers: 355 nm, 405 nm, 488 nm 561 nm, and 640 nm). The known concentration of counting beads allows for the number concentration of the stock solution to be calculated. Flow cytometry studies were done by Amy Burnside in the UMass IALS Flow Cytometry center.

5.3.2 Particle Capture Data and Pseudo-steady state character of accumulation kinetics

Studies of particle capture from flow were conducted in a shear flow chamber in which one wall presented dense positive charge. A suspension of particles in phosphate buffer with a Debye length of 2nm, was flowed over the surface. Studies at three concentrations for each sample of rod particles enabled consistency checks and comparison with the Leveque equation, in particular the linear pseudo steady state character of the capture. Studies at the one concentration for each sample were done in at least triplicate, while studies at the other two conditions were done in single or duplicate to conserve the very limited particle sample. Examples of particle accumulation for each sample and 3 concentrations are shown in Figure 50. Concentrations were determined by dilution of a known stock suspension, while the concentration of the "stock" concentrated suspension was determined to a precision limited by analytical methods, the relative concentrations of the solutions studied was known to greater precision.

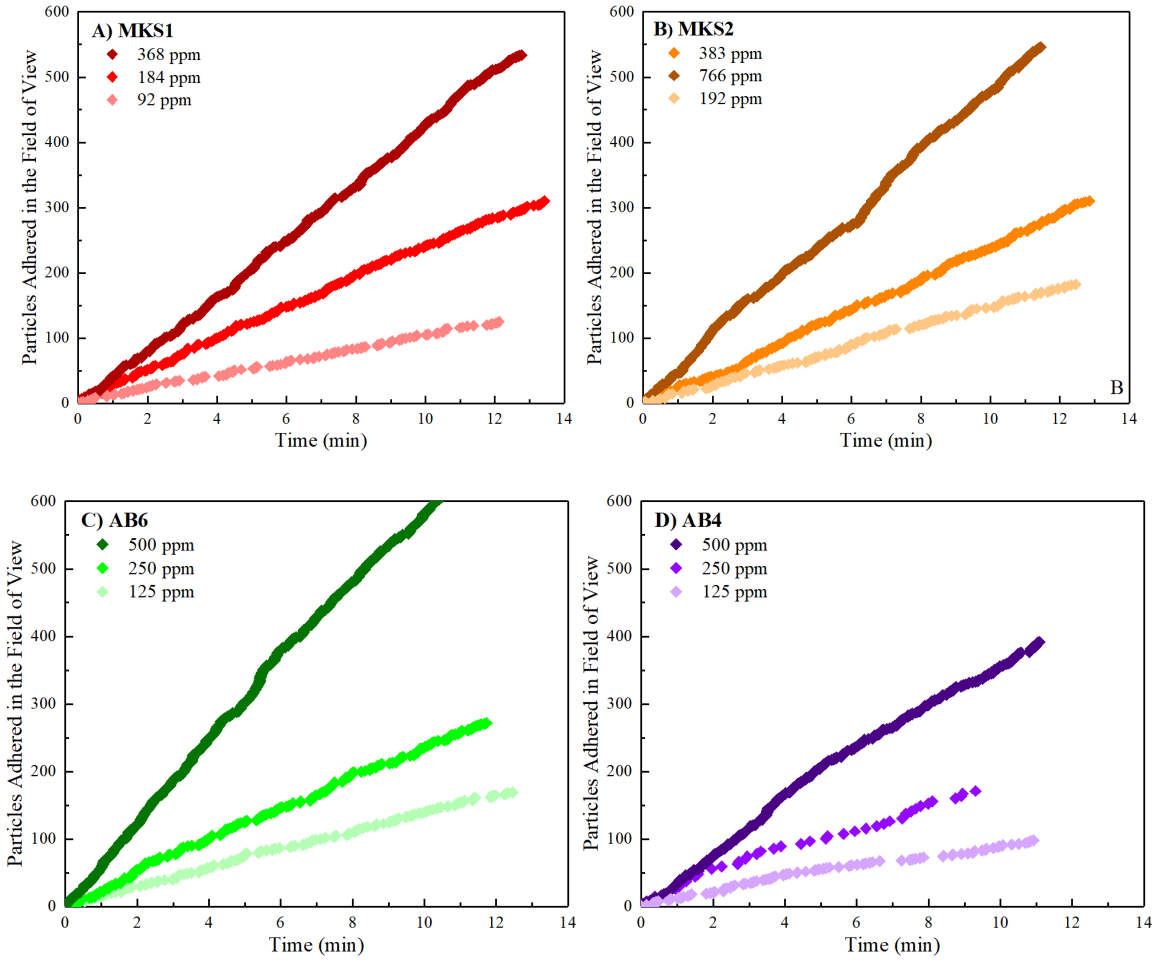

Figure 50. Particles adhered in the 260 x 178 µm field of view (A) MKS1, (B) MKS2, (C) AB6, and (D) AB4. All rods exhibit a linear trend in capture rate.

For runs with dispersions of rod particles, it was found that the number of particles captured was mostly linear with respect to time, independent of particle concentration and for numbers of particles sometimes exceeding 400 per in the field of view or 8.6 x10^5 per cm^2. This indicated that for the particle of interest, the flow conditions, and the densities of particles on the surface, the particle capture kinetics, were not influenced by particles already on the surface. Additionally, linearity in the numbers of particles on the surface as a function of time is consistent with a transport-limited capture, with a fully-established near-surface concentration boundary layer of particles in the flowing suspension. This boundary layer is in fact a particle-depleted region of fluid.

5.3.3 Surface Adhesion Rate

The raw data in Figure 50 demonstrate that the particle accumulation kinetics are linear in time. Figure 51 demonstrates the linear proportionality between the particle accumulation rate and the bulk solution particle concentration. This is shown for rods and for two spherical particle samples in Figure 51. The spheres were used as a control to confirm that the observed rate follows that predicted by the Leveque equation (Equation 6.3).[100]

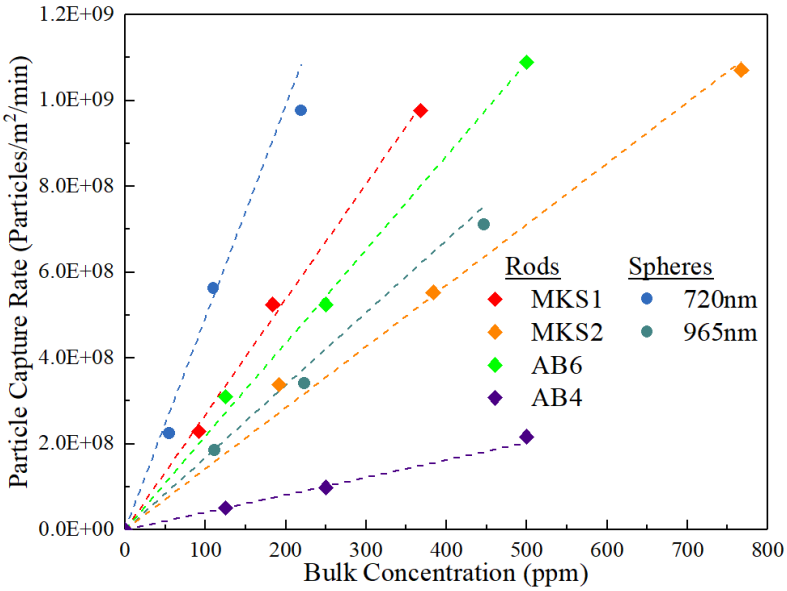

Figure 51. Particle capture rate as a function of concentration for the rods and spheres studies. Y-axis is based on died particle weights, x- axis is based on particles counted in the fields of view.

These data shows that for all the samples studied the particle capture rate is a linear in concentrations. That is when there are more particles in the solution the more will diffuse to the surface. The slopes of these lines are proportional to the diffusion coefficient to the two thirds power and a coefficient dependent on the particle mass density.

5.3.4 Comparison to Predicted Rates

Capture of rod-shaped particles was interpreted in the context of transport-limited capture of a diffusing species with a translational diffusivity in bulk solution, as described by Leveque.[100] Comparison was also made to the capture of equivalent spherical particles. In order to interpret the particle accumulation rates, the measure of the particles in free solution and on the surface must have the same units, either mass or number concentration and areal density.

5.3.4.1 Conversion of Number Density to Mass Density

The conversion of observed particle number density on the surface, on the y-axis of Figure 51 to a mass density on the surface in Figure 52 is accomplished by using the average particle size and an estimated particle density. A shell and core model was used to obtain a mass per particle, including a core and shell of different silica densities. Based on measured on particles synthesized using the same methods a core density of 1.9 g/cm^3 was assumed for the core[265] and the density of 2.2 g/cm^3 was assumed for the shell.

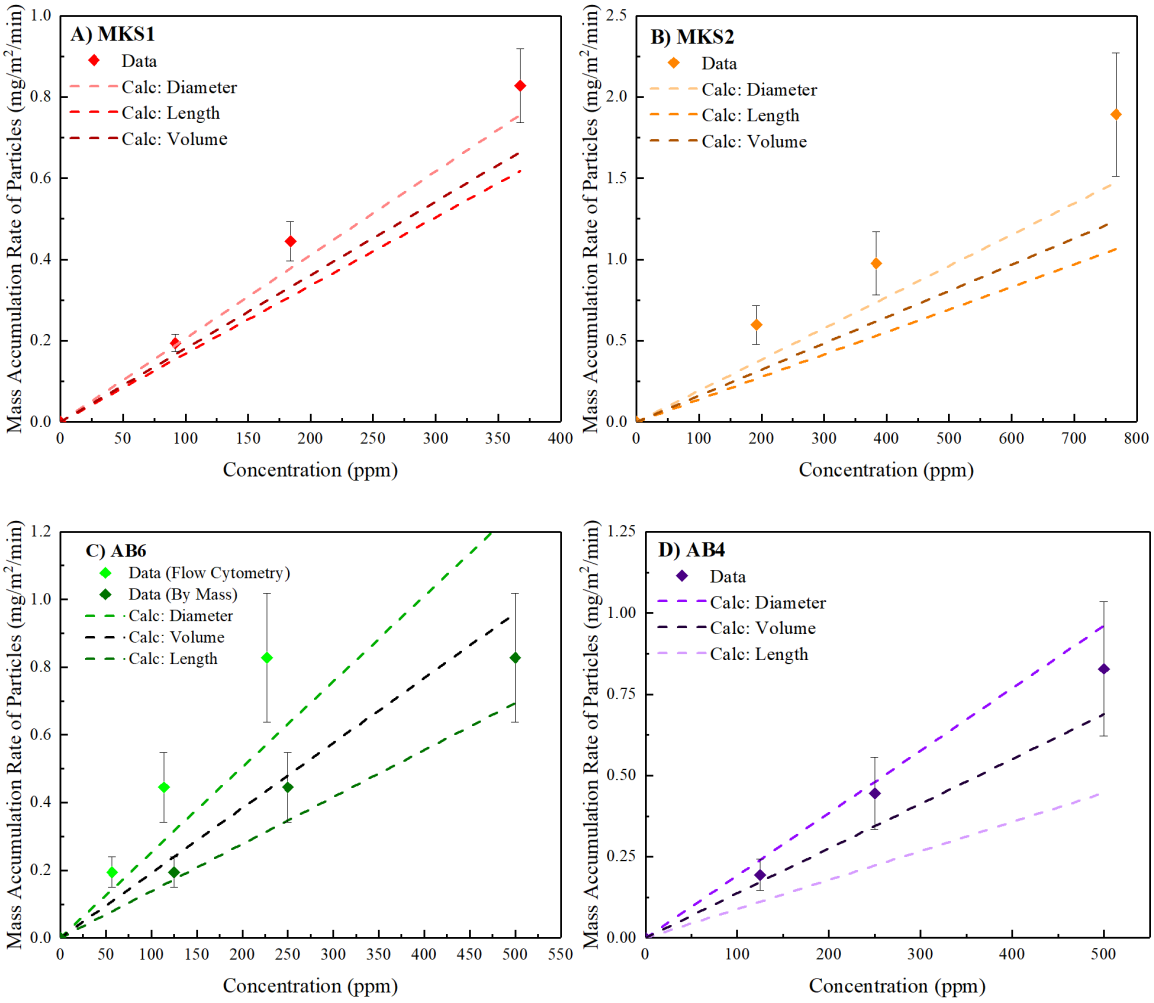

Figure 52. Comparison of experimental mass surface adhesion rates to theoretical mass surface adhesion rates calculated using the Leveque equation[100] for spheres with the same diameter, length, and volume as each rod particle. (A) MKS1, (B) MKS2, (C) AB6, and (D) AB4. All rods except for the AB4 rods have mass surface adhesion rates greater than that of a sphere with an equivalent diameter. The y-axis of all figures presents a mass accumulation rate that was calculated from the observed number accumulation rate by multiplying by the calculated mass per particle. The x-axis in parts A, B, D and the dark green points in C are based on the mass concentration determined by dried sample mass. The x-axis for the light green points in part C is based on the counted particles per volume from flow cytometry, multiplied by the calculated particle mass. Error bars are based on the imprecision in the particle size calculation.

To look at the effect of using different density values for this conversion in the Leveque model, we compared the effect of using different densities in calculating the particle density from the mass density. This effect is shown for the two spherical samples studied,

720 nm and 965 nm in Figure 53. The spherical particles were used for this comparison because they have significantly less polydispersity then the rods. Overall, the difference in particle density of 1.8 – 2.3 g/cm^3 results in a difference in the calculation of the adhesion rate of ~10%. This 0.5 g/cm^3 range is significantly larger than the actual error in our density which we predict is closer to 0.1, so the error from silica density does not have a significant effect on the results.

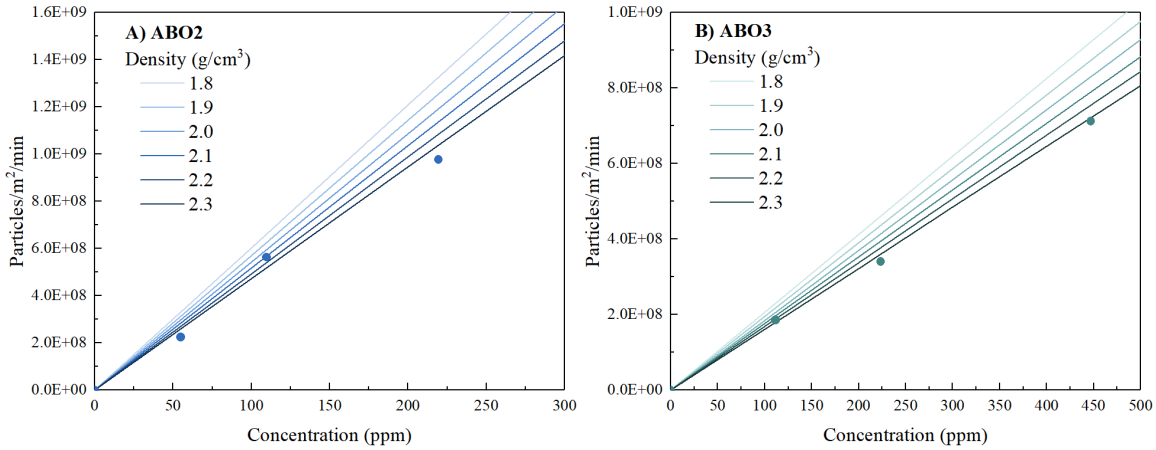

Figure 53. Difference in Leveque equation predictions for different spherical densities. For the lines the predicted particle adhesion rate was calculated the using the Leveque equation and density given. Data points are comparison to data from Figure 51. A) 720 nm Spheres, B) 965 nm Spheres.

An additional potential source for error is the uncertainty in the particle number concentration. Two methods were used to determine sample concentration of the rod suspension. A comparison of the concentrations by dried rod particle suspension weight vs flow cytometry is seen in Figure 54. Here the number concentration from flow cytometry is reported on the x-axis while the y-axis reports a number concentration calculated the dried weight of aliquots of the suspension. The two AB4 concentration measurements matched within 3%. For the MKS1, MKS2 the two concentration measurements are within

15%. For AB6 however there is a 50% difference between the two concentrations. This sample is unique because it is the smallest overall particle size. This particle is very close to the limit or detectability with our flow cell system at the 20x magnification. When these particles adhere on their end it is likely they are not visible in our instrument. To account for this and possible fines (though no evidence of fines was seen in the SEM) the flow cytometry concentration was used in further calculations.

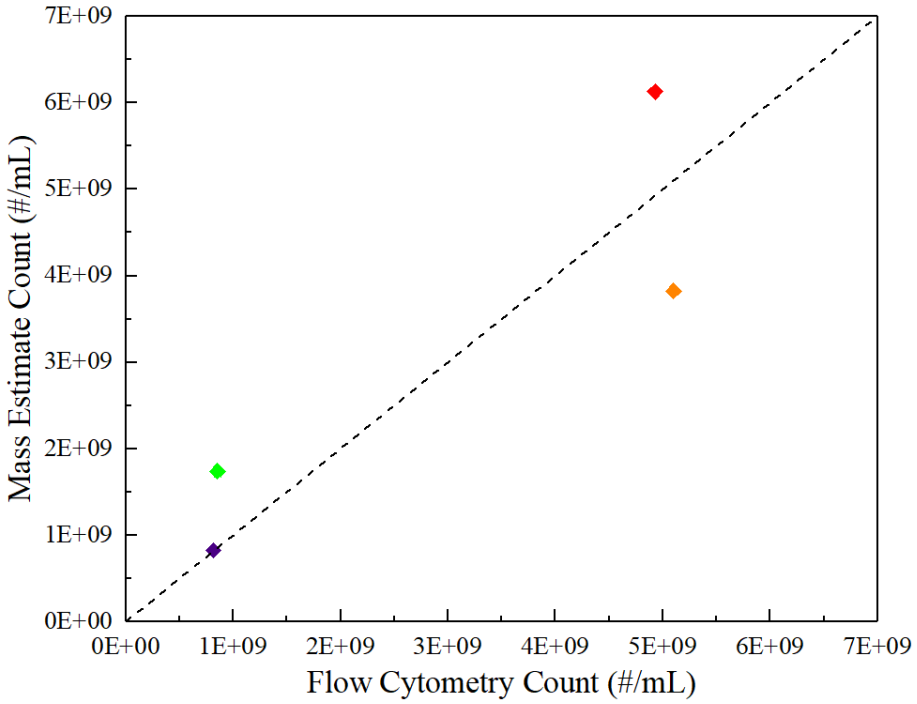

Figure 54. Comparison of stock rod particle concentration measurements between flow cytometry (x-axis) and mass (y-axis). MKS1(red), (MKS2 (orange), AB6 (green) and AB4 (purple).

Another error source in the conversion from mass concentration to number concentration comes from the poly dispersity in size of the rod samples. This is the largest error in the mass concentration calculation and therefore is the error used in calculation of the error bars in upcoming results.

5.3.4.2 Comparison to Leveque Prediction

Motivated by the drug delivery literature, Figure 52 makes comparisons between the rod samples and calculated behaviors of equivalent spheres, with the latter calculated from the Leveque equation and a bulk solution diffusivity appropriate to the sphere size. The darkest dashed line in each plot shows the calculated sphere capture rates for spheres whose diameters match the rod length. This situation considers the volume swept out by a rod rotating rapidly on multiple axes. It was found, as expected, that all the rod-shaped particles delivered more material to the surface then this upper size limit (Larger sized spheres deliver overall less material to the surface).

The next comparison was between the observed rod capture rates and that calculated for spheres (via Leveque) having the equivalent volume (darkest dashes). All the rod-shaped particles were also able to deliver more material then spheres of equivalent volume. This shows that the rods are more efficient at delivering material to the surface than spheres. But there seems to be some uncertainty that has to be addressed.

The final comparison was between the rod capture data and small spheres having diameters equal to the diameters of the rods. With the exception of rod sample AB4, which was both large and the highest aspect ratio, the rod capture rates exceed those of the equivalent spheres (this exception if addressed further in Section 5.3.4.1). This analysis reveals that how mass from rod-shaped particles accumulates more quickly than from different sizes of equivalent spheres, even when the latter adhere to a surface at the maximum transport limited rate, calculated according the Leveque equation.

While the mechanism of this behavior is not yet certain it is likely that the orientation of the rods as they pass through the boundary layer towards the surface is a critical component to this increased transport.

5.3.4.3 Orientation of Largest Rods

Sample AB4 (Aspect Ratio 3.17, length 2639 nm) were the only rods long enough that an accurate orientation data could be collected. Using a 20x objective, images of the surface were taken after the completion of the run by reintroduction of flowing buffer to removed free particles from the bulk solution. During this step, video was monitored to confirm that none of the captured particles escaped the surface. The flow chamber was then observed using a 40x objective. Since the camera was already set up for video capture, still images were captured by allowing the microscope to remain focused on a single point on the surface for about 5 sec and then the microscope was refocused on a different portion of the surface. Images were acquired using freeze frames of video both during the rinsing phase (with flow at a wall shear rate of 15 s^{-1}, the same as the flow conditions during particle capture) and after the rinse was completed (without flow). Here the pump was turned off and fluid retained in the flow chamber. The system was allowed to re-equilibrate for 10 minutes before images were acquired in these quiescent conditions.

Particles were then classified into three categories, depending on their orientation in the direction perpendicular to the surface: End (standing up perpendicular to the surface), transition (adhering by the end but leaning) and oriented (lying mostly flat) as seen in Figure 55.

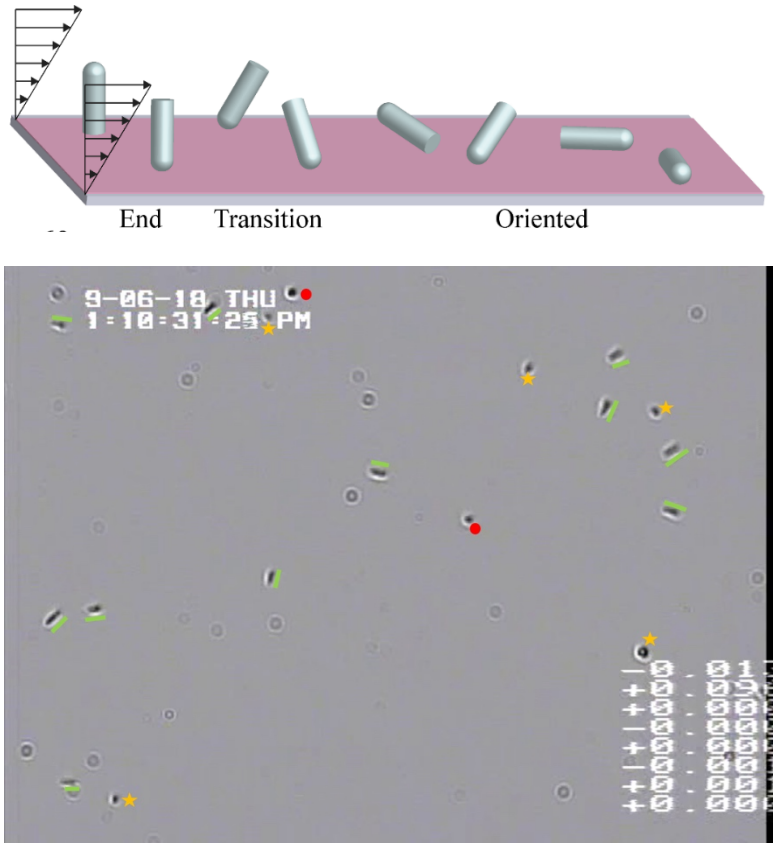

Figure 55. Definition of particle orientations criteria. Top is schematic of likely particle behavior and bottom is example of microscope image used for analysis. End-on particles are marked red, transition particles are marked yellow, and oriented particles are marked green. It is important to note that particles classified as orientated may not be lying completely flat on the surface but instead at a small enough angle that their orientation in-plane could be quantified precisely.

The in-surface-plane angle with respect to the flow direction is summarized in Figure 56, for approximately 350 particles in each run. Random orientation of captured particles would be indicated by an even height distribution across the bins in the figure. The data, however, indicate that flow biases the orientation of captured rods. This could be happening during flow itself, or a result of the adhesive process, for instance by a particle end. There is no statistical difference between the data sets with and without flow indicating that once particles are adhered to the surface they are relatively tightly bound and do not relax when the flow is turned off.

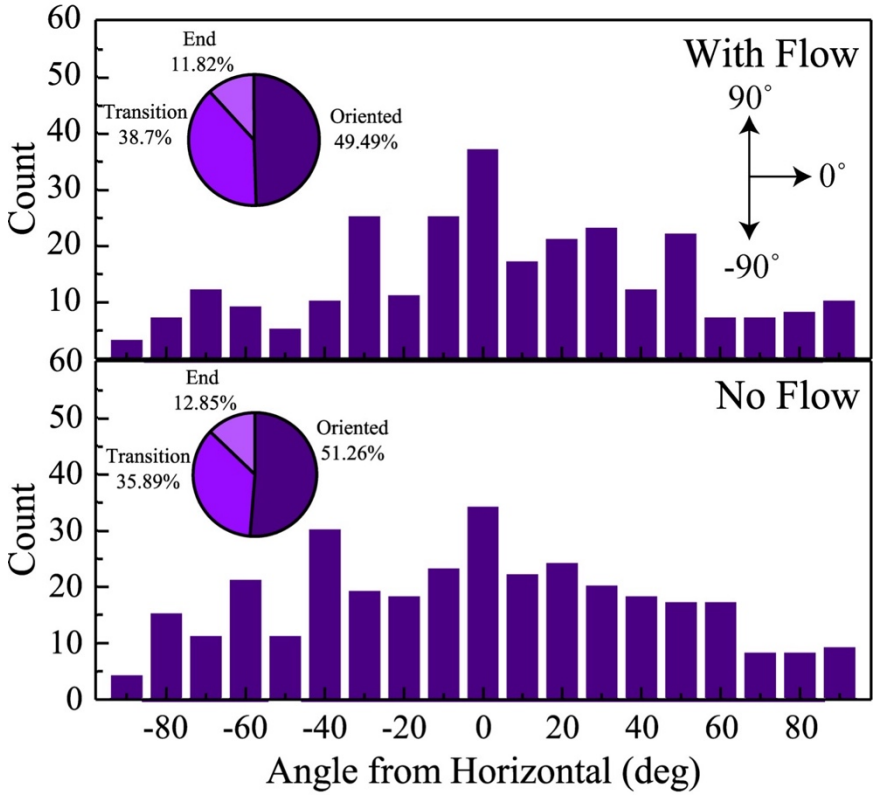

Figure 56. Orientation distribution of AB4 rods with and without flow. Data are raw particle counts and are not normalized. Flow rate in top portion is $15s^{-1}$.

5.3.5 Rod Diffusivity: Direct Calculations vs Inferred Values from particle capture

While capture of rod-shaped particles in Figure 52 appears highly efficient compared with that of spheres, further insight into capture behavior derives from consideration of the pseudo-steady state capture evident in the linear capture kinetics of Figure 50. To the extent that rod capture is transport limited, an equivalent rod diffusion coefficient can be derived from application of the Leveque equation to the observed capture kinetics. This equivalent diffusivity could potentially differ from the bulk solute quiescent diffusivities anticipated by equation 6.5-6.7 as a result of rod orientation in flow. The Pe number for the rod samples is on the order of 1 (0.74-1.25).

Figure 57 shows the results of this exercise: We find that for all but the largest rods the effective diffusion coefficients, back calculated from capture rates are significantly larger than predicted based on the models for a quiescent diffusion coefficient in Equations 5.3-5.5. This along with the orientation of the longest rods suggests that the flow is orientating the rods and increasing their transport rate to the surface.

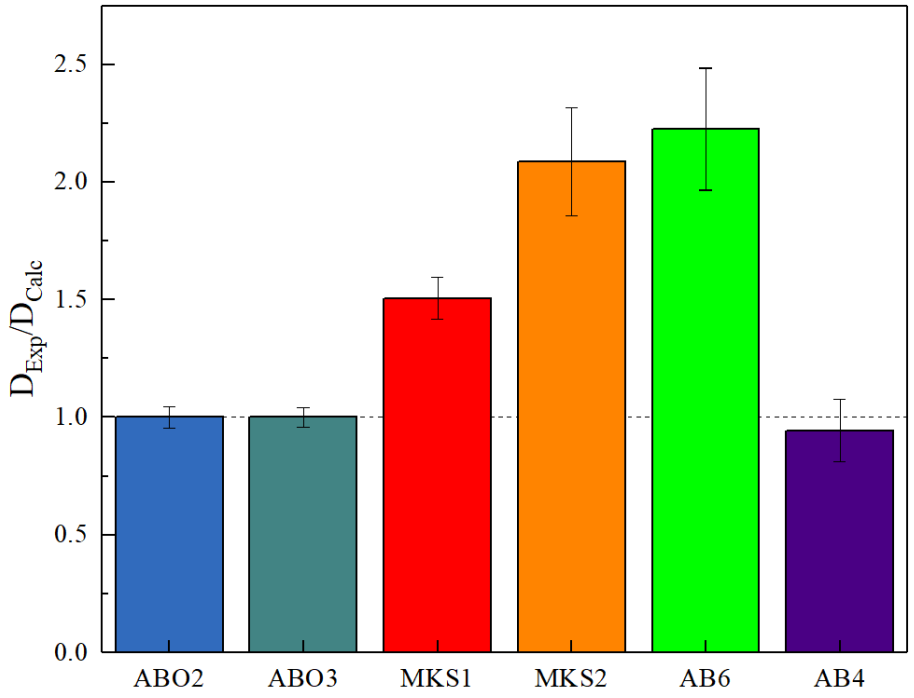

Figure 57. Ratio of diffusion coefficients obtained by fitting the flow cell data to the Leveque equation. And diffusion coefficients calculated using calculation 2 (Equations 6.3-6.5). Error bars are due to differences in diffusivity due to polydispersity in size.

The longest rods however have a dramatically lower capture rate, possibly as a result of fundamentally slower adhesion, (lower capture efficiency) relative to the increased hydrodynamic force with particle size. In fact, with the large particles in sample AB4, a log rolling type behavior was observed, that did not lead to particle arrest. This indicates that the electrostatic interaction forces between the poly-l-lysine surface and the silica particles might not be strong enough to capture particles in cases where there is significant

torque on the particles, or that lift forces stabilized particles against close approach to the surface in certain orientations.

5.4 Conclusions

This study showed that rod-shaped particles were able to more effectively deliver more particle mass to a strongly and rapidly-adherent surface compared with spherical particles of equivalent surface chemistry and volume or length scale.

The findings are significant in that rod-shaped particles could be highly effective as drug delivery packages due to their ability to orient with the flow and deliver material similar to the rate of their smallest dimension. There are however limits to this as large rod particles may prove to be more difficult to capture from flow and need a stronger surface force to successfully capture flowing rods. Additionally, further studied need to be completed to study the orientation, and flow behavior of such particles.

CHAPTER 6

CONCLUSIONS AND FUTURE WORK

Overall this dissertation showed three different ways that hydrodynamics can couple with particle chemistry and shape to affect colloid-surface interactions.

First, for engineered particles with capture controlled by sparse surface features, hydrodynamics produced adhesive capture rates that were substantially slower than particle capture rates using the same level of functionalization on an adhesive wall. The more efficient capture for the PLL functionalized wall occurred over a broad range of PLL surface loadings and ionic strengths at moderate shear rates.

Second, it was shown how the motility and the morphology of the bacteria play a significant role in the bacterial-surface interactions. Without flagella the No Flagella bacteria are able to approach the surface and dynamically interact with the surface for longer distances than any other strain. This is likely due to the lack of steric kicks from flagella interactions. At the other extreme the Super Swimmers are able to use their motility to stay engaged with the surface for longer periods of time. Their lower velocity however makes the overall distance traveled per engagement less than that of the No Flagella bacteria. Swimming also allows bacteria to actively transport to the surface increasing their number of interactions. Overall the Super Swimmers spend the most time engaging with the surface. When this project was expanded to look at the effect of surface mechanical properties, it was found that the effects due to the motility and morphology of the bacteria was significantly reduced on the soft hydrogel surface.

Finally, it was found that rod-shaped particles were able to more effectively deliver particle mass to a strongly and rapidly-adherent surface when compared with spherical particles of equivalent surface chemistry and volume or length scale. There are however limits to this as large rod particles may prove to be more difficult to capture from flow and need a stronger surface force to successfully capture flowing rods. Additionally, further studies need to be completed to study the orientation and flow behavior of such particles.

6.1 Stability of Patchy Particles

While the first portion of this thesis studied how the rotation of particles in flow can dictate the amount of surface that a patch is able to sample, compared with the amount a functionalized surface that a non-functionalized particle can sample. This project directly compared the behavior of functionalized particles on a unfunctionalized flat surface and bare particles on a functionalized flat surface in the presence of flow. Additionally, there is a large body of similar work comparing the aggregation and stability of colloids functionalized by polyelectrolytes in quiescent conditions.[20,22,24,30,44,46,47,274,275] Designing a system where the adhesion rate of particles onto a surface from flow is able to be directly compared to the aggregation and stability of a quiescent particle dispersion would led to the ability to begin to design particles able to selectively aggerate with target particles or cells, similar to the work done on selective capture in flow by the Santore lab.[50,51,105]

This could also potentially be used for the capture of small particles from solutions so that the small particles will settle out of solution at a faster rate. When there are two (or more) sized particles present in a dispersion, there are different zones of influence depending on if two of the same sized particles or two different sized particles are interacting. The

definitions for these zones of influence is shown in Figure 58 along with a comparison to the zone of influence of a particle on a flat surface. The zone of influence for the interaction between a large particle and a small particle will be smaller than the zone of influence for two large particles. Due to the lower threshold for aggregation seen for smaller particles,[276] similar to the lower adhesion threshold for smaller particle between a particle and a surface in flow, [48,105] a critical concentration of polyelectrolyte would allow the selective capture and aggregation of smaller particles by larger particles. This type of selective capture could be used to remove specific targets or containments from solution by capturing them on larger particles which will settle out of solution at a faster rate or be easily filtered out of solution.

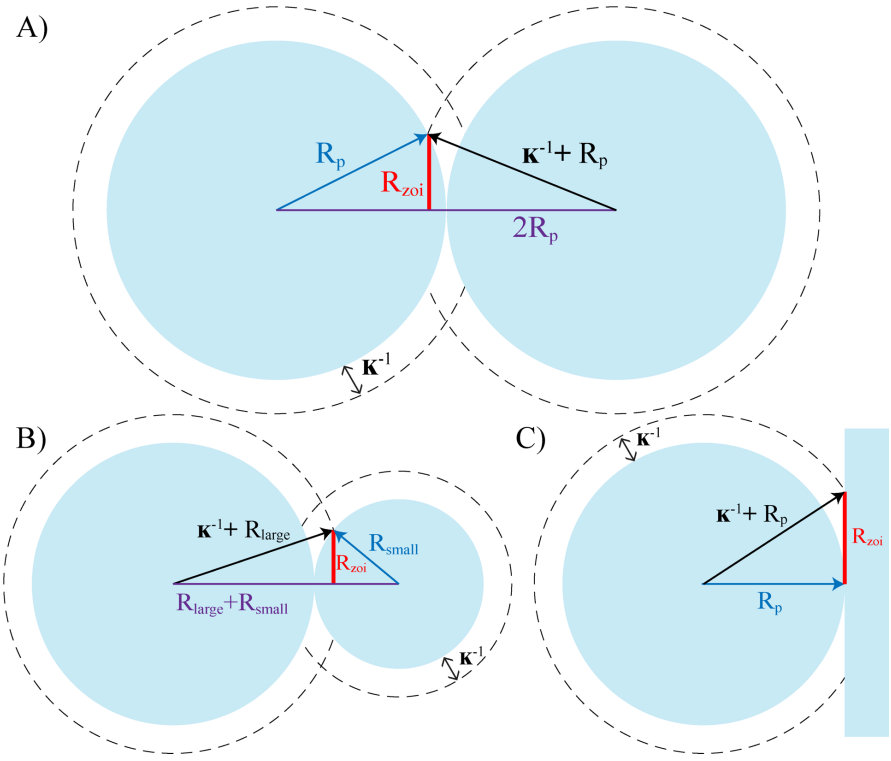

Figure 58. Definitions of the Zone of Influence in different conformations A) Between two identical particles, B) Between two particles of different sizes, C) Between a particle and a flat surface

6.2 Directionality of *E. coli* Swimming

In quiescent conditions it has been shown that smooth swimming *E. coli* with swim in clockwise circles.[75] When in narrow capillaries they swim in helical trajectories,[190] and in microfluidic channels with no imposed flow, both smooth swimming and run-and tumble swimmers have been showed to preferentially swim towards the right hand side of the chamber.[186] Preliminary analysis of the flow cell runs completed in Chapter 3 showed that the super swimmers have a directional bias in there y-direction motion. Two examples of this are seen in Figure 59 where by reversing the direction of the flow the preferred swimming direction of the bacteria can be controlled.

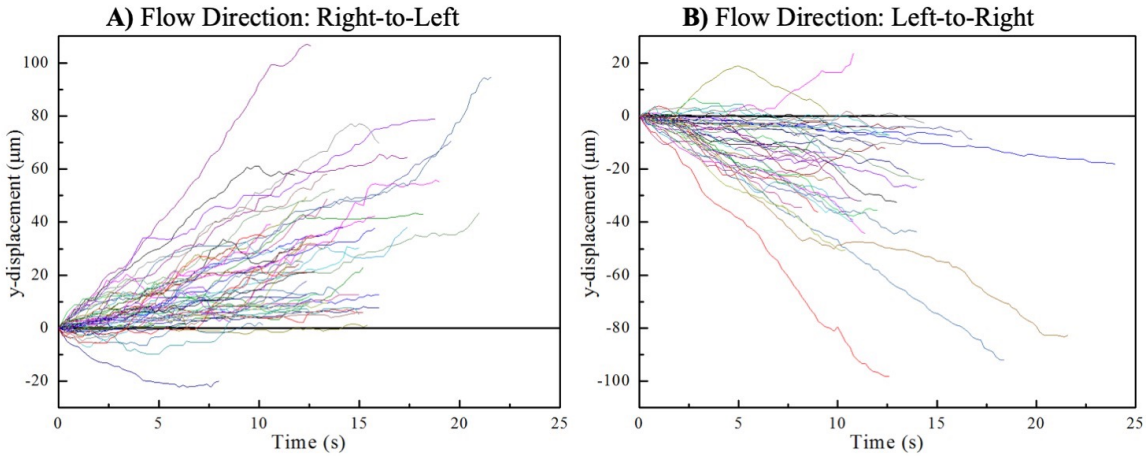

Figure 59. Y-displacement as a function of time for Super Swimmers on a brush surface. Plots show individual overall y-displacement for the same individual bacteria with surface engagements tracked in Chapter 3.

With even just a quick glance at the y-displacement tracks shown in Figure 59 it is clear that there is bias in the swimming direction of the Super Swimmers. Quantifying this behavior on the brush, potentially at multiple shear rates could provide further in sites on the hydrodynamic behavior of the bacteria. Additionally, well at first qualitative glance this directional behavior is seen in both hydrogel systems (Figure 60), though to a lesser

extent on the soft hydrogel, further quantitation may provide in sites into the hydrodynamic mechanisms for the differences in behavior seen with the different surface coatings.

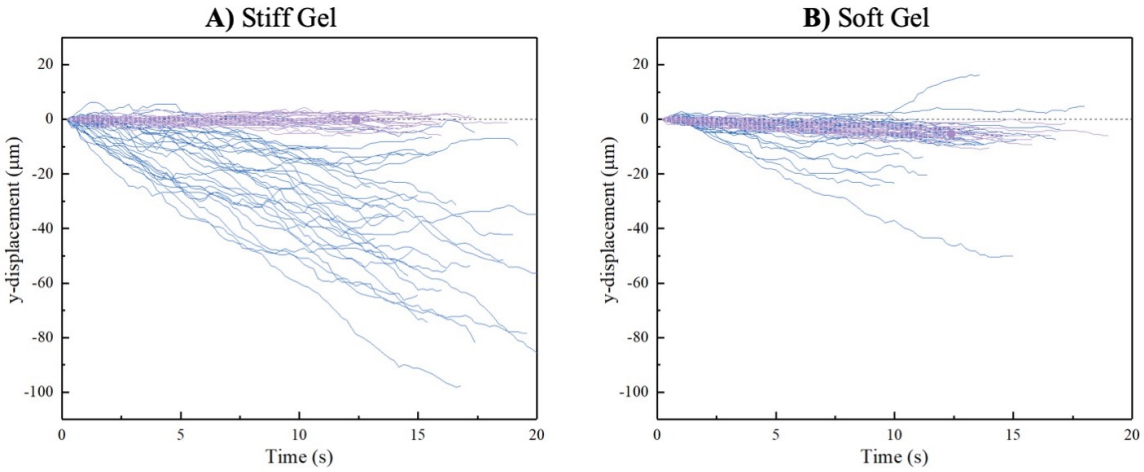

Figure 60. Y-displacement for the Super Swimmers (Blue) and No Flagella (Purple) on the stiff and soft hydrogels. Cells whose y-displacements are tracked here are the same cells as those tracked in Chapter 4. Y-displacement for the No Flagella bacteria is due to a slight angle in the alignment of the camera.

6.3 Flow Behavior of Rods Near a Surface

The studies discussed in Chapter 5 were limited to the capture of rods on an adhesive surface at a single shear rate. Rod shaped particles however have many other interesting flow behaviors could be studied using the rod system developed. Of particular interest in the flow behavior near surfaces in cases where the surface does not adhere the particles.

6.4 Rods as a model for bacteria behavior

Chapter 5 of this thesis discussed the increased diffusion rate of model rod-shaped colloids to a surface in flow while Chapter 3 and 4 discussed *E. coli* as a model bacterium. While this dissertation showed that there are many interesting flow behaviors exhibiting by both the bacteria and the rod-shaped particles. While the studies in this thesis look at separate phenomenon, the shape of the bodies of the *E. coli* draws obvious comparisons. An avenue

for further studies is in connecting the behavior of rod-shaped particles to the behavior of the No Flagella bacteria in flow.

REFERENCES

(1) Rowland, B. W. Colloid Chemistry in Paper Making. *J. Phys. Chem.* **1937**, *41* (7), 997–1005.

(2) De Gennes, P. G. Colloids: Ultradivided Matter. *Nature* **2001**, *412* (6845), 385.

(3) Svedberg, A.; Lindström, T. Improvement of the Retention-Formation Relationship Using Three-Component Retention Aid Systems, Royal Institute of Technology, 2012, Vol. 27.

(4) Bolto, B.; Gregory, J. Organic Polyelectrolytes in Water Treatment. *Water Res.* **2007**, *41* (11), 2301–2324.

(5) Perret, D.; Gaillard, J. F.; Dominik, J.; Atteia, O. The Diversity of Natural Hydrous Iron Oxides. *Environ. Sci. Technol.* **2000**, *34* (17), 3540–3546.

(6) W.B., R.; D.A., S.; W.R., S. *Colloidal Dispersions*; Cambridge University Press: Cambridge, U.K., 1989.

(7) Kalasin, S.; Browne, E. P.; Arcaro, K. F.; Santore, M. M. Selective Adhesive Cell Capture without Molecular Specificity: New Surfaces Exploiting Nanoscopic Polycationic Features as Discrete Adhesive Units. *RSC Adv.* **2017**, *7* (22), 13416–13425.

(8) Kalasin, S.; Dabkowski, J.; Nüsslein, K.; Santore, M. M. The Role of Nano-Scale Heterogeneous Electrostatic Interactions in Initial Bacterial Adhesion from Flow: A Case Study with Staphylococcus Aureus. *Colloids Surfaces B Biointerfaces* **2010**, *76* (2), 489–495.

(9) Shave, M. K.; Kalasin, S.; Ying, E.; Santore, M. M. Nanoscale Functionalized Particles with Rotation-Controlled Capture in Shear Flow. *ACS Appl. Mater. Interfaces* **2018**, *10* (34), 29058–29068.

(10) Elimelech, M.; O'Melia, C. R. Kinetics of Deposition of Colloidal Particles in Porous Media. *Environ. Sci. Technol.* **1990**, *24* (10), 1528–1536.

(11) Borkovec, M.; Papastavrou, G. Interactions between Solid Surfaces with Adsorbed Polyelectrolytes of Opposite Charge. *Curr. Opin. Colloid Interface Sci.* **2008**, *13* (6), 429–437.

(12) Adamczyk, Z.; Weroński, P. Application of the DLVO Theory for Particle Deposition Problems. *Adv. Colloid Interface Sci.* **1999**, *83* (1), 137–226.

(13) Fang, C.; Drelich, J. Theoretical Contact Angles on a Nano-Heterogeneous Surface Composed of Parallel Apolar and Polar Strips. *Langmuir* **2004**, *20* (16), 6679–6684.

(14) Sharma, A.; Konnur, R.; Kargupta, K. Thin Liquid Films on Chemically Heterogeneous Substrates: Self-Organization, Dynamics and Patterns in Systems Displaying a Secondary Minimum. *Phys. A Stat. Mech. its Appl.* **2003**, *318* (1–2), 262–278.

(15) Strobel, M.; Jones, V.; Lyons, C. S.; Ulsh, M.; Kushner, M. J.; Dorai, R.; Branch, M. C. A Comparison of Corona-Treated and Flame-Treated Polypropylene Films. *Plasmas Polym.* **2003**, *8* (1), 61–95.

(16) Kortright, J. B.; Kim, S. K.; Denbeaux, G. P.; Zeltzer, G.; Takano, K.; Fullerton, E. E. Soft-x-Ray Small-Angle Scattering as a Sensitive Probe of Magnetic and Charge Heterogeneity. *Phys. Rev. B - Condens. Matter Mater. Phys.* **2001**, *64* (9), 924011–924014.

(17) Tombácz, E.; Szekeres, M. Surface Charge Heterogeneity of Kaolinite in Aqueous Suspension in Comparison with Montmorillonite. *Appl. Clay Sci.* **2006**, *34* (1–4), 105–124.

(18) Gun'ko, V. M.; Leboda, R.; Turov, V. V.; Villiéras, F.; Skubiszewska-Zięba, J.; Chodorowski, S.; Marciniak, M. Structural and Energetic Nonuniformities of Pyrocarbon-Mineral Adsorbents. *J. Colloid Interface Sci.* **2001**, *238* (2), 340–356.

(19) Mahnke, J.; Stearnes, J.; Hayes, R. A.; Fornasiero, D.; Ralston, J. The Influence of Dissolved Gas on the Interactions between Surfaces of Different Hydrophobicity in Aqueous Media Part I. Measurement of Interaction Forces. *Phys. Chem. Chem. Phys.* **1999**, *1* (11), 2793–2798.

(20) Gregory, J. Rates of Flocculation of Latex Particles by Cationic Polymers. *J. Colloid Interface Sci.* **1973**, *42* (2), 448–456.

(21) Gregory, J.; Barany, S. Adsorption and Flocculation by Polymers and Polymer Mixtures. *Adv. Colloid Interface Sci.* **2011**, *169* (1), 1–12.

(22) Gregory, J. The Effect of Cationic Polymers on the Colloidal Stability of Latex Particles. *J. Colloid Interface Sci.* **1976**, *55* (1), 35–43.

(23) Szilagyi, I.; Rosicka, D.; Hierrezuelo, J.; Borkovec, M. Charging and Stability of Anionic Latex Particles in the Presence of Linear Poly(Ethylene Imine). *J. Colloid Interface Sci.* **2011**, *360* (2), 580–585.

(24) Popa, I.; Trulsson, M.; Papastavrou, G.; Borkovec, M.; J??nsson, B. Long-Ranged Attractive Forces Induced by Adsorbed Dendrimers: Direct Force Measurements and Computer Simulations. *Langmuir* **2009**, *25* (21), 12435–12438.

(25) Wang, Z.; Hemmer, S. L.; Friedrich, D. M.; Joly, A. G. Anthracene as the Origin of the Red-Shifted Emission from Commercial Zone-Refined Phenanthrene Sorbed on Mineral Surfaces. *J. Phys. Chem. A* **2001**, *105* (25), 6020–6023.

(26) Priest, C.; Stevens, N.; Sedev, R.; Skinner, W.; Ralston, J. Inferring Wettability of Heterogeneous Surfaces by ToF-SIMS. *J. Colloid Interface Sci.* **2008**, *320* (2), 563–568.

(27) Holthoff, H.; Schmitt, A.; Fernández-Barbero, A.; Borkovec, M.; Cabrerízo-Vílchez, M. Á.; Schurtenberger, P.; Hidalgo-Álvarez, R. Measurement of Absolute Coagulation Rate Constants for Colloidal Particles: Comparison of Single and Multiparticle Light Scattering Techniques. *J. Colloid Interface Sci.* **1997**, *192* (2), 463–470.

(28) Yu, W. L.; Bouyer, F.; Borkovec, M. Polystyrene Sulfate Latex Particles in the Presence of Poly(Vinylamine): Absolute Aggregation Rate Constants and Charging Behavior. *J. Colloid Interface Sci.* **2001**, *241* (2), 392–399.

(29) Popa, I.; Gillies, G.; Papastavrou, G.; Borkovec, M. Attractive Electrostatic Forces between Identical Colloidal Particles Induced by Adsorbed Polyelectrolytes. *J. Phys. Chem. B* **2009**, *113* (25), 8458–8461.

(30) Bouyer, F.; Robben, A.; Yu, W. L.; Borkovec, M. Aggregation of Colloidal Particles in the Presence of Oppositely Charged Polyelectrolytes : Effect of Surface Charge Heterogeneities. **2001**, No. 15, 5225–5231.

(31) Rasmuson, A.; Pazmino, E.; Assemi, S.; Johnson, W. P. Contribution of Nano- to Microscale Roughness to Heterogeneity: Closing the Gap between Unfavorable and Favorable Colloid Attachment Conditions. *Environ. Sci. Technol.* **2017**, *51* (4), 2151–2160.

(32) Duval, J. F. L.; Leermakers, F. A. M.; Van Leeuwen, H. P. Electrostatic Interactions between Double Layers: Influence of Surface Roughness, Regulation, and Chemical Heterogeneities. *Langmuir* **2004**, *20* (12), 5052–5065.

(33) Mayor, S.; Rao, M. Rafts: Scale-Dependent, Active Lipid Organization at the Cell Surface. *Traffic* **2004**, *5* (4), 231–240.

(34) PIKE, L. J. Lipid Rafts: Heterogeneity on the High Seas. *Biochem. J.* **2004**, *378* (2), 281–292.

(35) Hancock, J. F. Lipid Rafts: Contentious Only from Simplistic Standpoints. *Nat. Rev. Mol. Cell Biol.* **2006**, *7* (6), 456–462.

(36) Jacobs, C.; Shapiro, L. Bacterial Cell Division: A Moveable Feast. *Proc. Natl. Acad. Sci.* **1999**, *96* (11), 5891–5893.

(37) Jones, J. F.; Feick, J. D.; Imoudu, D.; Chukwumah, N.; Vigeant, M.; Velegol, D. Oriented Adhesion of Escherichia Coli to Polystyrene Particles. *Appl. Environ. Microbiol.* **2003**, *69* (11), 6515–6519.

(38) Shapiro, L.; Shapiro, L.; Mcadams, H. H.; Losick, R. 2002-Shapiro Generating and Exploiting Polarity in Bacteria. **2013**, *1942* (2002), 1942–1947.

(39) Silverblatt, F. J.; Dreyer, J. S.; Schauer, S. Effect of Pili on Susceptibility of Escherichia Coli to Phagocytosis. *Infect. Immun.* **1979**, *24* (1), 218–223.

(40) Strom, M. S.; Lory, S. Structure-Function and Biogenesis of the Type Iv Pili. *Annu. Rev. Microbiol.* **1993**, *47* (1), 565–596.

(41) Israelachvili, J. N. *Intermolecular and Surface Forces*, Third Edit.; Academic Press: Burlington, Mass, 2011.

(42) Lin, W.; Galletto, P.; Borkovec, M. Charging and Aggregation of Latex Particles by Oppositely Charged Dendrimers. *Langmuir* **2004**, *20* (18), 7465–7473.

(43) Feng, L.; Adachi, Y.; Kobayashi, A. Kinetics of Brownian Flocculation of Polystyrene Latex by Cationic Polyelectrolyte as a Function of Ionic Strength. *Colloids Surfaces A Physicochem. Eng. Asp.* **2014**, *440*, 155–160.

(44) Leong, Y. K. Charged Patch Attraction in Dispersion: Effect of Polystyrene Sulphonate Molecular Weight or Patch Size. *Colloid Polym. Sci.* **2001**, *279* (1), 82–87.

(45) Miklavic, S. J.; Chan, D. Y. C.; White, L. R.; Healy, T. W. Double Layer Forces between Heterogeneous Charged Surfaces. *J. Phys. Chem.* **1994**, *98* (36), 9022–9032.

(46) Leong, Y. K.; Scales, P. J.; Healy, T. W.; Boger, D. V. Interparticle Forces Arising from Adsorbed Polyelectrolytes in Colloidal Suspensions. *Colloids Surfaces A Physicochem. Eng. Asp.* **1995**, *95* (1), 43–52.

(47) Popa, I.; Gillies, G.; Papastavrou, G.; Borkovec, M. Attractive and Repulsive Electrostatic Forces between Positively Charged Latex Particles in the Presence of Anionic Linear Polyelectrolytes. *J. Phys. Chem. B* **2010**, *114* (9), 3170–3177.

(48) Kalasin, S.; Santore, M. M. Engineering Nanoscale Surface Features to Sustain Microparticle Rolling in Flow. *ACS Nano* **2015**, *9* (5), 4706–4716.

(49) Kalasin, S.; Santore, M. M. Sustained Rolling of Microparticles in Shear Flow over an Electrostatically Patchy Surface. *Langmuir* **2010**, *26* (4), 2317–2324.

(50) Kalasin, S.; Browne, E. P.; Arcaro, K. F.; Santore, M. M. Selective Adhesive Cell Capture without Molecular Specificity: New Surfaces Exploiting Nanoscopic Polycationic Features as Discrete Adhesive Units. *RSC Adv.* **2017**, *7* (22), 13416–13425.

(51) Fang, B.; Gon, S.; Nüsslein, K.; Santore, M. M. Surfaces for Competitive Selective Bacterial Capture from Protein Solutions. *ACS Appl. Mater. Interfaces* **2015**, *7* (19), 10275–10282.

(52) Fang, B.; Gon, S.; Park, M. H.; Kumar, K. N.; Rotello, V. M.; Nusslein, K.; Santore, M. M. Using Flow to Switch the Valency of Bacterial Capture on Engineered Surfaces Containing Immobilized Nanoparticles. *Langmuir* **2012**, *28* (20), 7803–7810.

(53) Gao, W.; Feng, X.; Pei, A.; Gu, Y.; Li, J.; Wang, J. Seawater-Driven Magnesium Based Janus Micromotors for Environmental Remediation. *Nanoscale* **2013**, *5* (11), 4696–4700.

(54) Gao, W.; Uygun, A.; Wang, J. Hydrogen-Bubble-Propelled Zinc-Based Microrockets in Strongly Acidic Media. *J. Am. Chem. Soc.* **2012**, *134* (2), 897–900.

(55) Soler, L.; Magdanz, V.; Fomin, V. M.; Sanchez, S.; Schmidt, O. G. Self-Propelled Micromotors for Cleaning Polluted Water. *ACS Nano* **2013**, *7* (11), 9611–9620.

(56) Baraban, L.; Makarov, D.; Streubel, R.; Mönch, I.; Grimm, D.; Sanchez, S.; Schmidt, O. G. Catalytic Janus Motors on Microfluidic Chip: Deterministic Motion for Targeted Cargo Delivery. *ACS Nano* **2012**, *6* (4), 3383–3389.

(57) Sundararajan, S.; Lammert, P. E.; Zudans, A. W.; Crespi, V. H.; Sen, A. Catalytic Motors for Transport of Colloidal Cargo. *Nano Lett.* **2008**, *8* (5), 1271–1276.

(58) Hong, Y.; Blackman, N. M. K.; Kopp, N. D.; Sen, A.; Velegol, D. Chemotaxis of Nonbiological Colloidal Rods. *Phys. Rev. Lett.* **2007**, *99* (17), 1–4.

(59) Ebbens, S. J. Active Colloids: Progress and Challenges towards Realising Autonomous Applications. *Curr. Opin. Colloid Interface Sci.* **2016**, *21*, 14–23.

(60) Palacci, J.; Sacanna, S.; Kim, S.-H.; Yi, G.-R.; Pine, D. J.; Chaikin, P. M. Light Activated Self-Propelled Colloids. *Phil. Trans. R. Soc. A* **2014**, *372*, 20130372.

(61) Palacci, J.; Sacanna, S.; Abramian, A.; Barral, J.; Hanson, K.; Grosberg, A. Y.; Pine, D. J.; Chaikin, P. M. Artificial Rheotaxis. *Sci. Adv.* **2015**, *1* (4), 1–7.

(62) Stevens, J. M.; Galyov, E. E.; Stevens, M. P. Actin-Dependent Movement of Bacterial Pathogens. *Nat. Rev. Microbiol.* **2006**, *4* (2), 91–101.

(63) Lauga, E.; Powers, T. R. The Hydrodynamics of Swimming Microorganisms. *Reports Prog. Phys.* **2009**, *72* (9).

(64) Purcell, E. M. Life at Low Reynolds Number. *Am. J. Phys.* **1977**, *45* (1), 3–11.

(65) Berg, H. C. The Rotary Motor of Bacterial Flagella. *Annu. Rev. Biochem.* **2003**, *72* (1), 19–54.

(66) Wu, K.-T.; Hsiao, Y.-T.; Woon, W.-Y. Entrapment of Pusher and Puller Bacteria near a Solid Surface. *Phys. Rev. E* **2018**, *98* (5), 052407.

(67) Koyasu, S.; Shirakihara, Y. Caulobacter Crescentus Flagellar Filament Has a Right-Handed Helical Form. *J. Mol. Biol.* **1984**, *173* (1), 125–130.

(68) Shaevitz, J. W.; Lee, J. Y.; Fletcher, D. A. Spiroplasma Swim by a Processive Change in Body Helicity. *Cell* **2005**, *122* (6), 941–945.

(69) Berg, H. C. The Rotary Motor of Bacterial Flagella. *Annu. Rev. Biochem.* **2003**, *72* (1), 19–54.

(70) Scharf, B. Real-Time Imaging of Fluorescent Flagellar Filaments of Rhizobium Lupini H13-3: Flagellar Rotation …. *J. Bacteriol.* **2002**, *182* (10), 2793–2801.

(71) Berg, H. C. Motile Behavior of Bacteria. *Phys. Today* **2000**, *53* (1), 24–29.

(72) Hansen, C. H.; Endres, R. G.; Wingreen, N. S. Chemotaxis in Escherichia Coli: A Molecular Model for Robust Precise Adaptation. *PLoS Comput. Biol.* **2008**, *4* (1), 0014–0027.

(73) Kirkegaard, J. B.; Goldstein, R. E. The Role of Tumbling Frequency and Persistence in Optimal Run-and-Tumble Chemotaxis. *IMA J. Appl. Math. (Institute Math. Its Appl.* **2018**, *83* (4), 700–719.

(74) Lauga, E.; Diluzio, W. R.; Whitesides, G. M.; Stone, H. A. Swimming in Circles : Motion of Bacteria near Solid Boundaries. **2006**, *90* (January), 400–412.

(75) Lauga, E.; DiLuzio, W. R.; Whitesides, G. M.; Stone, H. A. Swimming in Circles: Motion of Bacteria near Solid Boundaries. *Biophys. J.* **2006**, *90* (2), 400–412.

(76) Berke, A. P.; Turner, L.; Berg, H. C.; Lauga, E. Hydrodynamic Attraction of Swimming Microorganisms by Surfaces. *Phys. Rev. Lett.* **2008**, *101* (3), 1–4.

(77) Rothschild, Lord. Non-Random Distribution of Bull Spermatozoa in a Drop of Sperm Suspension. *Nature* **1963**, *200* (4904), 381.

(78) Cosson, J.; Huitorel, P.; Gagnon, C. How Spermatozoa Come to Be Confined to Surfaces. *Cell Motil. Cytoskeleton* **2003**, *54* (1), 56–63.

(79) Li, G. J.; Ardekani, A. M. Hydrodynamic Interaction of Microswimmers near a Wall. *Phys. Rev. E - Stat. Nonlinear, Soft Matter Phys.* **2014**, *90* (1), 1–12.

(80) Di Leonardo, R.; Dell'Arciprete, D.; Angelani, L.; Iebba, V. Swimming with an Image. *Phys. Rev. Lett.* **2011**, *106* (3), 038101.

(81) Jeffery, G. B. The Motion of Ellipsoidal Particles Immersed in a Viscous Fluid. *Proc. R. Soc. A Math. Phys. Eng. Sci.* **1922**, *102* (715), 161–179.

(82) Rusconi, R.; Stocker, R. Microbes in Flow. *Curr. Opin. Microbiol.* **2015**, *25*, 1–8.

(83) Rusconi, R.; Guasto, J. S.; Stocker, R. Bacterial Transport Suppressed by Fluid Shear. *Nat. Phys.* **2014**, *10* (3), 212–217.

(84) Marcos; Fu, H. C.; Powers, T. R.; Stocker, R. Bacterial Rheotaxis. *Proc. Natl. Acad. Sci. U. S. A.* **2012**, *109* (13), 4780–4785.

(85) Hill, J.; Kalkanci, O.; McMurry, J. L.; Koser, H. Hydrodynamic Surface Interactions Enable Escherichia Coli to Seek Efficient Routes to Swim Upstream. *Phys. Rev. Lett.* **2007**, *98* (6), 1–4.

(86) Lee, S. Y.; Ferrari, M.; Decuzzi, P. Shaping Nano-/Micro-Particles for Enhanced Vascular Interaction in Laminar Flows. *Nanotechnology* **2009**, *20* (49).

(87) Vahidkhah, K.; Bagchi, P. Microparticle Shape Effects on Margination, near-Wall Dynamics and Adhesion in a Three-Dimensional Simulation of Red Blood Cell Suspension. *Soft Matter* **2015**, *11* (11), 2097–2109.

(88) D'Apolito, R.; Tomaiuolo, G.; Taraballi, F.; Minardi, S.; Kirui, D.; Liu, X.; Cevenini, A.; Palomba, R.; Ferrari, M.; Salvatore, F.; et al. Red Blood Cells Affect the Margination of Microparticles in Synthetic Microcapillaries and Intravital Microcirculation as a Function of Their Size and Shape. *J. Control. Release* **2015**, *217*, 263–272.

(89) Toy, R.; Peiris, P. M.; Ghaghada, K. B.; Karathanasis, E. Shaping Cancer Nanomedicine: The Effect of Particle Shape on the in Vivo Journey of Nanoparticles NIH Public Access. *Nanomedicine (Lond)* **2014**, *9* (1), 121–134.

(90) Decuzzi, P.; Pasqualini, R.; Arap, W.; Ferrari, M. Intravascular Delivery of Particulate Systems: Does Geometry Really Matter? *Pharm. Res.* **2009**, *26* (1), 235–243.

(91) Decuzzi, P.; Lee, S.; Bhushan, B.; Ferrari, M. A Theoretical Model for the Margination of Particles within Blood Vessels. *Ann. Biomed. Eng.* **2005**, *33* (2), 179–190.

(92) Gentile, F.; Chiappini, C.; Fine, D.; Bhavane, R. C.; Peluccio, M. S.; Cheng, M. M. C.; Liu, X.; Ferrari, M.; Decuzzi, P. The Effect of Shape on the Margination Dynamics of Non-Neutrally Buoyant Particles in Two-Dimensional Shear Flows. *J. Biomech.* **2008**, *41* (10), 2312–2318.

(93) Müller, K.; Fedosov, D. A.; Gompper, G. Understanding Particle Margination in Blood Flow - A Step toward Optimized Drug Delivery Systems. *Med. Eng. Phys.* **2016**, *38* (1), 2–10.

(94) Champion, J. A.; Katare, Y. K.; Mitragotri, S. Particle Shape: A New Design Parameter for Micro- and Nanoscale Drug Delivery Carriers. *J. Control. Release* **2007**, *121* (1–2), 3–9.

(95) Gavze, E.; Shapiro, M. Particles in a Shear Flow near a Solid Wall: Effect of Nonsphericity on Forces and Velocities. *Int. J. Multiph. Flow* **1997**, *23* (1), 155–182.

(96) Kolhar, P.; Anselmo, A. C.; Gupta, V.; Pant, K.; Prabhakarpandian, B.; Ruoslahti, E.; Mitragotri, S. Using Shape Effects to Target Antibody-Coated Nanoparticles to Lung and Brain Endothelium. *Proc. Natl. Acad. Sci.* **2013**, *110* (26), 10753–10758.

(97) Doshi, N.; Prabhakarpandian, B.; Rea-ramsey, A.; Pant, K.; Sundaram, S.; Mitragotri, S. Flow and Adhesion of Drug Carriers in Blood Vessels Depend on Their Shape : A Study Using Model Synthetic Microvascular Networks. *J. Control. Release* **2010**, *146* (2), 196–200.

(98) Kim, D. K.; Hyun, J. Y.; Kim, S. C.; Kim, H. S.; Lee, S. Y. Inertial Effects on Cylindrical Particle Migration in Linear Shear Flow near a Wall. *Microfluid. Nanofluidics* **2016**, *20* (5), 1–10.

(99) Rosén, T.; Lundell, F.; Aidun, C. K. Effect of Fluid Inertia on the Dynamics and Scaling of Neutrally Buoyant Particles in Shear Flow. *J. Fluid Mech.* **2014**, *738*, 563–590.

(100) Leveque, A. Les Lois de La Transmission de Chaleur Par Convection. *Ann. Mines* **1928**, *Series 12* (13), 201–299.

(101) Lok, B. K.; Cheng, Y. L.; Robertson, C. R. Total Internal Reflection Fluorescence: A Technique for Examining Interactions of Macromolecules with Solid Surfaces. *J. Colloid Interface Sci.* **1983**, *91* (1), 87–103.

(102) K. Lok, B.; Cheng, Y.-L.; Robertson, C. R. Protein Adsorption on Crosslinked Polydimethylsiloxane Using Total Internal Reflection Fluorescence. *J. Colloid Interface Sci.* **1983**, *91* (1), 104–116.

(103) Zarghami, A.; Padding, J. T. Drag, Lift and Torque Acting on a Two-Dimensional Non-Spherical Particle near a Wall. *Adv. Powder Technol.* **2018**, *29* (6), 1507–1517.

(104) Kalasin, S.; Santore, M. M. Hydrodynamic Crossover in Dynamic Microparticle Adhesion on Surfaces of Controlled Nanoscale Heterogeneity. *Langmuir* **2008**, *24* (9), 4435–4438.

(105) Santore, M. M.; Kozlova, N. Micrometer Scale Adhesion on Nanometer-Scale Patchy Surfaces: Adhesion Rates, Adhesion Thresholds, and Curvature-Based Selectivity. *Langmuir* **2007**, *23* (9), 4782–4791.

(106) Kozlova, N.; Santore, M. M. Manipulation of Micrometer-Scale Adhesion by Tuning Nanometer-Scale Surface Features. *Langmuir* **2006**, *22* (3), 1135–1142.

(107) Bacchin, P.; Aimar, P.; Sanchez, V. Model for Colloidal Fouling of Membranes. *AIChE J.* **1995**, *41* (2), 368–376.

(108) Bluestein, D.; Niu, L.; Schoephoerster, R. T.; Dewanjeet, M. K. Fluid Mechanics of Arterial Stenosis: Relationship to the Development of Mural Thrombus. *Ann. Biomed. Eng.* **1997**, *25* (9), 344–356.

(109) Ninto, Y.; Garcia, M. H. Experiments on Particle—Turbulence Interactions in the near–Wall Region of an Open Channel Flow: Implications for Sediment Transport. *J. Fluid Mech.* **1996**, *326*, 285–319.

(110) Solomentsev, Y.; Böhmer, M.; Anderson, J. L. Particle Clustering and Pattern Formation during Electrophoretic Deposition: A Hydrodynamic Model. *Langmuir* **1997**, *13* (23), 6058–6068.

(111) Johnson, P. R.; Sun, N.; Elimelech, M. Colloid Transport in Geochemically Heterogeneous Porous Media : Modeling and Measurements Colloid Transport in Geochemically Heterogeneous Porous Media : Modeling and Measurements. *Environ. Sci. Technol.* **1996**, *30* (11), 3284–3293.

(112) Boks, N. P.; Norde, W.; van der Mei, H. C.; Busscher, H. J. Forces Involved in Bacterial Adhesion to Hydrophilic and Hydrophobic Surfaces. *Microbiology* **2008**, *154* (10), 3122–3133.

(113) Meinders, J. M.; van der Mei, H. C.; Busscher, H. J. Deposition Efficiency and Reversibility of Bacterial Adhesion under Flow. *J. Colloid Interface Sci.* **1995**, *176* (2), 329–341.

(114) Walz, J. Y. The Effect of Surface Heterogeneities on Colloidal Forces. *Adv. Colloid Interface Sci.* **1998**, *74*, 119–168.

(115) Kemps, J. A. L.; Bhattacharjee, S. Particle Tracking Model for Colloid Transport near Planar Surfaces Covered with Spherical Asperities. *Langmuir* **2009**, *25* (12), 6887–6897.

(116) Hoek, E. M. V.; Agarwal, G. K. Extended DLVO Interactions between Spherical Particles and Rough Surfaces. *J. Colloid Interface Sci.* **2006**, *298* (1), 50–58.

(117) Hoek, E. M. V.; Bhattacharjee, S.; Elimelech, M. Effect of Membrane Surface Roughness on Colloid-Membrane DLVO Interactions. *Langmuir* **2003**, *19* (11), 4836–4847.

(118) Bendersky, M.; Davis, J. M. DLVO Interaction of Colloidal Particles with Topographically and Chemically Heterogeneous Surfaces. *J. Colloid Interface Sci.* **2011**, *353* (1), 87–97.

(119) Brant, J. A.; Johnson, K. M.; Childress, A. E. Characterizing NF and RO Membrane Surface Heterogeneity Using Chemical Force Microscopy. *Colloids Surfaces A Physicochem. Eng. Asp.* **2006**, *280* (1–3), 45–57.

(120) Chatterjee, R.; Mitra, S. K.; Bhattacharjee, S. Particle Deposition onto Janus and Patchy Spherical Collectors. *Langmuir* **2011**, *27* (14), 8787–8797.

(121) Duffadar, R. D.; Davis, J. M. Dynamic Adhesion Behavior of Micrometer-Scale Particles Flowing over Patchy Surfaces with Nanoscale Electrostatic Heterogeneity. *J. Colloid Interface Sci.* **2008**, *326* (1), 18–27.

(122) Duffadar, R. D.; Kalasin, S.; Davis, J. M.; Santore, M. M. The Impact of Nanoscale Chemical Features on Micron-Scale Adhesion: Crossover from Heterogeneity-Dominated to Mean-Field Behavior. *J. Colloid Interface Sci.* **2009**, *337* (2), 396–407.

(123) Everett, W. N.; Wu, H. J.; Anekal, S. G.; Sue, H. J.; Bevan, M. A. Diffusing Colloidal Probes of Protein and Synthetic Macromolecule Interactions. *Biophys. J.* **2007**, *92* (3), 1005–1013.

(124) Kline, T. R.; Chen, G.; Walker, S. L. Colloidal Deposition on Remotely Controlled Charged Micropatterned Surfaces in a Parallel-Plate Flow Chamber. *Langmuir* **2008**, *24* (17), 9381–9385.

(125) Li, Y.; Wang, Y.; Pennell, K. D.; Abriola, L. M. Investigation of the Transport and Deposition of Fullerene (C60) Nanoparticles in Quartz Sands under Varying Flow Conditions Investigation of the Transport and Deposition of Fullerene (C60) Nanoparticles in Quartz Sands under Varying Flow Conditions. **2008**, *42* (19), 7174–7180.

(126) Ma, H.; Pazmino, E.; Johnson, W. P. Surface Heterogeneity on Hemispheres-in-Cell Model Yields All Experimentally-Observed Non-Straining Colloid Retention Mechanisms in Porous Media in the Presence of Energy Barriers. *Langmuir* **2011**, *27* (24), 14982–14994.

(127) Song, L.; Elimelech, M. Transient Deposition of Colloidal Particles in Heterogeneous Porous Media. *Journal of Colloid And Interface Science*. 1994, pp 301–313.

(128) Song, L.; Johnson, P. R.; Elimelech, M. Kinetics of Colloid Deposition onto Heterogeneously Charged Surfaces in Porous Media. *Environ. Sci. Technol.* **1994**, *28* (6), 1164–1171.

(129) Haque, M. E.; Shen, C.; Li, T.; Chu, H.; Wang, H.; Li, Z.; Huang, Y. Influence of Biochar on Deposition and Release of Clay Colloids in Saturated Porous Media. *J. Environ. Qual.* **2017**, *46* (6), 1480.

(130) Johnson, W. P.; Rasmuson, A.; Pazmiño, E.; Hilpert, M. Why Variant Colloid Transport Behaviors Emerge among Identical Individuals in Porous Media When Colloid-Surface Repulsion Exists. *Environ. Sci. Technol.* **2018**, *52* (13).

(131) Pazmino, E.; Trauscht, J.; Dame, B.; Johnson, W. P. Power Law Size-Distributed Heterogeneity Explains Colloid Retention on Soda Lime Glass in the Presence of Energy Barriers. *Langmuir* **2014**, *30* (19), 5412–5421.

(132) Trauscht, J.; Pazmino, E.; Johnson, W. P. Prediction of Nanoparticle and Colloid Attachment on Unfavorable Mineral Surfaces Using Representative Discrete Heterogeneity. *Langmuir* **2015**, *31* (34), 9366–9378.

(133) Lüthi, Y.; Rička, J.; Borkovec, M. Colloidal Particles at Water-Glass Interface: Deposition Kinetics and Surface Heterogeneity. *J. Colloid Interface Sci.* **1998**, *206* (1), 314–321.

(134) Tian, Y.; Gao, B.; Wu, L.; Muñoz-Carpena, R.; Huang, Q. Effect of Solution Chemistry on Multi-Walled Carbon Nanotube Deposition and Mobilization in Clean Porous Media. *J. Hazard. Mater.* **2012**, *231–232*, 79–87.

(135) Farrokhi-Rad, M.; Shahrabi, T. Effect of Triethanolamine on the Electrophoretic Deposition of Hydroxyapatite Nanoparticles in Isopropanol. *Ceram. Int.* **2013**, *39* (6), 7007–7013.

(136) Kalasin, S.; Santore, M. M. Near-Surface Motion and Dynamic Adhesion during Silica Microparticle Capture on a Polymer (Solvated PEG) Brush via Hydrogen Bonding. *Macromolecules* **2016**, *49* (1), 334–343.

(137) Chen, X.; Shen, W.; Kou, S.; Liu, H. GC-MS Study of the Removal of Dissolved and Colloidal Substances in Recycled Papermaking by Flocculation with Nano-Size TiO 2 Colloids. *BioResources* **2011**, *6* (3), 3300–3312.

(138) Plleva, F. M.; Galaev, I. Y.; Mattiasson, B. Macroporous Gels Prepared at Subzero Temperatures as Novel Materials for Chromatography of Particulate-Containing Fluids and Cell Culture Applications. *J. Sep. Sci.* **2007**, *30* (11), 1657–1671.

(139) Seekell, R. P.; Dever, R.; Zhu, Y. Control Hydrogel-Hyaluronic Acid Aggregation toward the Design of Biomimetic Superlubricants. *Biomacromolecules* **2014**, *15* (7), 2760–2768.

(140) Caputo, K. E.; Lee, D.; King, M. R.; Hammer, D. A. Adhesive Dynamics Simulations of the Shear Threshold Effect for Leukocytes. *Biophys. J.* **2007**, *92* (3), 787–797.

(141) Goldsmith, H. L.; McIntosh, F. A.; Shahin, J.; Frojmovic, M. M. Time and Force Dependence of the Rupture of Glycoprotein IIb-IIIa- Fibrinogen Bonds between Latex Spheres. *Biophys. J.* **2000**, *78* (3), 1195–1206.

(142) Konda, S. S. M.; Brantley, J. N.; Bielawski, C. W.; Makarov, D. E. Chemical Reactions Modulated by Mechanical Stress: Extended Bell Theory. *J. Chem. Phys.* **2011**, *135* (16).

(143) Pierres, A.; Benoliel, A. M.; Bongrand, P.; van der Merwe, P. A. Determination of the Lifetime and Force Dependence of Interactions of Single Bonds between Surface-Attached CD2 and CD48 Adhesion Molecules. *Proc. Natl. Acad. Sci.* **1996**, *93* (26), 15114–15118.

(144) Tees, D. F. J.; Coenen, O.; Goldsmith, H. L. Interaction Forces between Red Cells Agglutinated by Antibody. IV. Time and Force Dependence of Break-Up. *Biophys. J.* **1993**, *65* (3), 1318–1334.

(145) Tees, D. F. J.; Waugh, R. E.; Hammer, D. A. A Microcantilever Device to Assess the Effect of Force on the Lifetime of Selectin-Carbohydrate Bonds. *Biophys. J.* **2001**, *80* (2), 668–682.

(146) Tees, D. F. J.; Woodward, J. T.; Hammer, D. A. Reliability Theory for Receptor-Ligand Bond Dissociation. *J. Chem. Phys.* **2001**, *114* (17), 7483–7496.

(147) Chong, S. H.; Ham, S. Dynamics of Hydration Water Plays a Key Role in Determining the Binding Thermodynamics of Protein Complexes. *Sci. Rep.* **2017**, *7* (1), 1–10.

(148) Bhatia, S. K.; King, M. R.; Hammer, D. A. The State Diagram for Cell Adhesion Mediated by Two Receptors. *Biophys. J.* **2003**, *84* (April), 2671–2690.

(149) Lawrence, M. B.; Springer, T. A. Leukocytes Roll on a Selectin at Physiologic Flow Rates: Distinction from and Prerequisite for Adhesion through Integrins. *Cell* **1991**, *65* (5), 859–873.

(150) Alon, R.; Hammer, D. A.; Springer, T. A. Lifetime of the P-Selectin-Carbohydrate Bond and Its Response to Tensile Force in Hydrodynamic Flow. *Nature* **1995**, *377* (6544), 86–86.

(151) Bhatia, S. K.; Hammer, D. A. Influence of Receptor and Ligand Density on the Shear Threshold Effect for Carbohydrate-Coated Particles on L-Selectin. *Langmuir* **2002**, *18* (15), 5881–5885.

(152) Han, J.; Zern, B. J.; Shuvaev, V. V.; Davies, P. F.; Muro, S.; Muzykantov, V. Acute and Chronic Shear Stress Differently Regulate Endothelial Internalization of Nanocarriers Targeted to Platelet-Endothelial Cell Adhesion Molecule-1. *ACS Nano* **2012**, *6* (10), 8824–8836.

(153) Moore, T. L.; Hauser, D.; Gruber, T.; Rothen-Rutishauser, B.; Lattuada, M.; Petri-Fink, A.; Lyck, R. Cellular Shuttles: Monocytes/Macrophages Exhibit Transendothelial Transport of Nanoparticles under Physiological Flow. *ACS Appl. Mater. Interfaces* **2017**, *9* (22), 18501–18511.

(154) Simion, V.; Constantinescu, C. A.; Stan, D.; Deleanu, M.; Tucureanu, M. M.; Butoi, E.; Manduteanu, I.; Simionescu, M.; Calin, M. P-Selectin Targeted Dexamethasone-Loaded Lipid Nanoemulsions: A Novel Therapy to Reduce Vascular Inflammation. *Mediators Inflamm.* **2016**, *2016*.

(155) Kelley, W. J.; Safari, H.; Lopez-Cazares, G.; Eniola-Adefeso, O. Vascular-Targeted Nanocarriers: Design Considerations and Strategies for Successful Treatment of Atherosclerosis and Other Vascular Diseases. *Wiley Interdiscip. Rev. Nanomedicine Nanobiotechnology* **2016**, *8* (6), 909–926.

(156) Gon, S.; Bendersky, M.; Ross, J. L.; Santore, M. M. Manipulating Protein Adsorption Using a Patchy Protein-Resistant Brush. *Langmuir* **2010**, *26* (14), 12147–12154.

(157) Zhang, J.; Srivastava, S.; Duffadar, R. D.; Davis, J. M.; Rotello, V. M.; Santore, M. M. Manipulating Microparticles with Single Surface-Immobilized Nanoparticles. *Langmuir* **2008**, *24* (13), 6404–6408.

(158) Santore, M. M.; Zhang, J.; Srivastava, S.; Rotello, V. M. Beyond Molecular Recognition: Using a Repulsive Field to Tune Interfacial Valency and Binding Specificity between Adhesive Surfaces. *Langmuir* **2009**, *25* (1), 84–96.

(159) Duffadar, R. D.; Davis, J. M. Interaction of Micrometer-Scale Particles with Nanotextured Surfaces in Shear Flow. *J. Colloid Interface Sci.* **2007**, *308* (1), 20–29.

(160) Lin, S.; Wiesner, M. R. Exact Analytical Expressions for the Potential of Electrical Double Layer Interactions for a Sphere-Plate System. *Langmuir* **2010**, *26* (22), 16638–16641.

(161) Goldman, A. J.; Cox, R. G.; Brenner, H. Slow Viscous Motion of a Sphere Parallel to a Plane Wall - II Couette Flow. *Chem. Eng. Sci.* **1967**, *22* (4), 653–660.

(162) Robeson, J. L.; Tilton, R. D. Effect of Concentration Quenching on Fluorescence Recovery after Photobleaching Measurements. *Biophys. J.* **1995**, *68* (5), 2145–2155.

(163) Fu, Z.; Santore, M. M. Poly(Ethylene Oxide) Adsorption onto Chemically Etched Silicates by Brewster Angle Reflectivity. *Colloids Surfaces A Physicochem. Eng. Asp.* **1998**, *135* (1–3), 63–75.

(164) Toscano, A.; Santore, M. M. Fibrinogen Adsorption on Three Silica-Based Surfaces: Conformation and Kinetics. *Langmuir* **2006**, *22* (6), 2588–2597.

(165) Blaakmeer, J.; Bohmer, M. R.; Stuart, M. a C.; Fleer, G. J. Adsorption of Weak Polyelectrolytes on Highly Charged Surfaces - Poly(Acrylic Acid) on Polystyrene Latex With Strong Cationic Groups. *Macromolecules* **1990**, *23* (8), 2301–2309.

(166) Böhmer, M. R.; Evers, O. A.; Scheutjens, J. M. M. Weak Polyelectrolytes Between Two Surfaces: Adsorption and Stabilization. *Macromolecules* **1990**, *23* (8), 2288–2301.

(167) Santore, M. M. Dynamics in Adsorbed Homopolymer Layers: Understanding Complexity from Simple Starting Points. *Curr. Opin. Colloid Interface Sci.* **2005**, *10* (3–4), 176–183.

(168) Sukhishvili, S. A.; Granick, S. Polyelectrolyte Adsorption onto an Initially-Bare Solid Surface of Opposite Electrical Charge. *J. Chem. Phys.* **1998**, *109* (16), 6861–6868.

(169) Scales, P. J.; Grieser, F.; Healy, T. W.; White, L. R.; Chan, D. Y. C. Electrokinetics of the Silica-Solution Interface: A Flat Plate Streaming Potential Study. *Langmuir* **1992**, *8* (3), 965–974.

(170) Popping, B.; Deratani, A.; Sebille, B.; Desbois, N.; Lamarche, J. M.; Foissy, A. The Effects of Electrical Charge on the Adsorption of a Weak Cationic Polyelectrolyte onto Silica, Silicon Carbide and Calcium Fluoride. *Colloids and Surfaces* **1992**, *64* (2), 125–133.

(171) Sukhishvili, S. A.; Granick, S. Kinetic Regimes of Polyelectrolyte Exchange between the Adsorbed State and Free Solution. *J. Chem. Phys.* **1998**, *109* (16), 6869–6878.

(172) Hansupalak, N.; Santore, M. M. Sharp Polyelectrolyte Adsorption Cutoff Induced by a Monovalent Salt. *Langmuir* **2003**, *19* (18), 7423–7426.

(173) Dahlgren, M. A. G.; Claesson, P. M.; Audebert, R. Highly Charged Cationic Polyelectrolytes on Mica: Influence of Polyelectrolyte Concentration on Surface Forces. *J. Colloid Interface Sci.* **1994**, *166*, 343–349.

(174) Bendersky, M.; Santore, M. M.; Davis, J. M. A Computational Study of Chemically Heterogeneous Particles : Patchy vs . Uniform Particles in Shear Flow. *Cond-Mat* **2015**.

(175) Berg, H. C. Motile Behavior of Bacteria. *Phys. Today* **2000**, *53* (1), 24–29.

(176) Besser, R. E.; Lett, S. M.; Weber, J. T.; Barrett, T. J.; Doyle, M. P.; Griffin, P. M. An Outbreak of Diarrhea and Hemolytic Uremic Syndrome ForEscherichia Coli 0157:H7 in Fresh- Pressed Apple Cider. *J. Am. Med. Assoc.* **1993**, *269(17)*, :2217-2220.

(177) Center for Disease Control and Prevention. Ongoing Multistate Outbreak of Escherichia Coli Serotype O157 : H7 Infections Associated with Consumption of Fresh Spinach. *Morb. Mortal. Wkly. Rep.* **2006**, *55*, 1–2.

(178) Scallan, E.; Hoekstra, R. M.; Angulo, F. J.; Tauxe, R. V.; Widdowson, M. A.; Roy, S. L.; Jones, J. L.; Griffin, P. M. Foodborne Illness Acquired in the United States-Major Pathogens. *Emerg. Infect. Dis.* **2011**, *17* (1), 7–15.

(179) Romeo, T. *Bacterial Biofilms*; 2008; Vol. 322.

(180) Trautner, Barbara W.; Darouiche, R. O. Catheter Associated Infections. *Arch Intern Med.* **2004**, *164* (8), 842–850.

(181) Pedley, T. J.; Kessler, J. O. Hydrodynamic Phenomena in Suspensions of Swimming Microorganisms. *Annu. Rev. Fluid Mech.* **1992**, *24*, 313–358.

(182) Hu, J.; Yang, M.; Gompper, G.; Winkler, R. G. Modelling the Mechanics and Hydrodynamics of Swimming E. Coli. *Soft Matter* **2015**, *11* (40), 7843–8020.

(183) Misselwitz, B.; Barrett, N.; Kreibich, S.; Vonaesch, P.; Andritschke, D.; Rout, S.; Weidner, K.; Sormaz, M.; Songhet, P.; Horvath, P.; et al. Near Surface Swimming of Salmonella Typhimurium Explains Target-Site Selection and Cooperative Invasion. *PLoS Pathog.* **2012**, *8* (7), 9.

(184) Conrad, J. C.; Gibiansky, M. L.; Jin, F.; Gordon, V. D.; Motto, D. A.; Mathewson, M. A.; Stopka, W. G.; Zelasko, D. C.; Shrout, J. D.; Wong, G. C. L. Flagella and Pili-Mediated near-Surface Single-Cell Motility Mechanisms in P. Aeruginosa. *Biophys. J.* **2011**, *100* (7), 1608–1616.

(185) Li, G.; Bensson, J.; Nisimova, L.; Munger, D.; Mahautmr, P.; Tang, J. X.; Maxey, M. R.; Brun, Y. V. Accumulation of Swimming Bacteria near a Solid Surface. *Phys. Rev. E - Stat. Nonlinear, Soft Matter Phys.* **2011**, *84* (4), 1–8.

(186) DiLuzio, W. R.; Turner, L.; Mayer, M.; Garstecki, P.; Weibel, D. B.; Berg, H. C.; Whitesides, G. M. Escherichia Coli Swim on the Right-Hand Side. *Nature* **2005**, *435* (7046), 1271–1274.

(187) Elgeti, J.; Gompper, G. Wall Accumulation of Self-Propelled Spheres. *EPL (Europhysics Lett.* **2013**, *101* (4), 48003.

(188) Pratt, L. A.; Kolter, R. Genetic Analysis of Escherichia Coli Biofilm Formation: Roles of Flagella, Motility, Chemotaxis and Type I Pili. *Mol. Microbiol.* **1998**, *30* (2), 285–293.

(189) Kaya, T.; Koser, H. Direct Upstream Motility in Escherichia Coli. *Biophys. J.* **2012**, *102* (7), 1514–1523.

(190) Ping, L.; Wasnik, V.; Emberly, E. Bacterial Motion in Narrow Capillaries. *FEMS Microbiol. Ecol.* **2015**, *91* (2), 1–7.

(191) Kolewe, K. W.; Kalasin, S.; Shave, M.; Schiffman, J. D.; Santore, M. M. Mechanical Properties and Concentrations of Poly(Ethylene Glycol) in Hydrogels and Brushes Direct the Surface Transport of Staphylococcus Aureus. *ACS Appl. Mater. Interfaces* **2018**, acsami.8b18302.

(192) Berne, C.; Ducret, A.; Hardy, G. G.; Brun, Y. V. Adhesions Involved in Attachment to Abiotic Surfaces by Gram-Negative Bacteria. *Microbiol. Spectr.* **2015**, *3* (4), 1–45.

(193) Thomas, W. E.; Trintchina, E.; Forero, M.; Vogel, V.; Sokurenko, E. V. Bacterial Adhesion to Target Cells Enhanced by Shear Force. *Cell* **2002**, *109* (7), 913–923.

(194) Nilsson, L. M.; Thomas, W. E.; Trintchina, E.; Vogel, V.; Sokurenko, E. V. Catch Bond-Mediated Adhesion without a Shear Threshold: Trimannose versus Monomannose Interactions with the FimH Adhesin of Escherichia Coli. *J. Biol. Chem.* **2006**, *281* (24), 16656–16663.

(195) Palacci, J.; Sacanna, S.; Steinberg, A. P.; Pine, D. J.; Chaikin, P. M. Living Crystals of Light-Activated Colloidal Surfers. *Science (80-.).* **2013**, *339* (6122), 936–940.

(196) Patch, A.; Yllanes, D.; Marchetti, M. C. Kinetics of Motility-Induced Phase Separation and Swim Pressure. *Phys. Rev. E* **2017**, *95* (1), 1–8.

(197) Yang, X.; Manning, M. L.; Marchetti, M. C. Aggregation and Segregation of Confined Active Particles. **2014**, *672* (c), 6477–6484.

(198) Blount, Z. D. The Unexhausted Potential of E. Coli. *Elife* **2015**, *4*, 1–12.

(199) Baba, T.; Ara, T.; Hasegawa, M.; Takai, Y.; Okumura, Y.; Baba, M.; Datsenko, K. A.; Tomita, M.; Wanner, B. L.; Mori, H. Construction of Escherichia Coli K-12 in-Frame, Single-Gene Knockout Mutants: The Keio Collection. *Mol. Syst. Biol.* **2006**, *2*.

(200) Liu, X.; Matsumura, P. The FlhD/FlhC Complex, a Transcriptional Activator of the <i>Escherichia Coli<i/> Flagellar Class II Operons. *J. Bacteriol.* **1994**, *176* (23), 7345–7351.

(201) Nguyen, C. C.; Saier, M. H. Structural and Phylogenetic Analysis of the MotA and MotB Families of Bacterial Flagellar Motor Proteins. *Res. Microbiol.* **1996**, *147* (5), 317–332.

(202) Kingshott, P.; Griesser, H. J. Surfaces That Resist Bioadhesion. *Curr. Opin. Solid State Mater. Sci.* **1999**, *4* (4), 403–412.

(203) Banerjee, I.; Pangule, R. C.; Kane, R. S. Antifouling Coatings: Recent Developments in the Design of Surfaces That Prevent Fouling by Proteins, Bacteria, and Marine Organisms. *Adv. Mater.* **2011**, *23* (6), 690–718.

(204) Hucknall, A.; Rangarajan, S.; Chilkoti, A. In Pursuit of Zero: Polymer Brushes That Resist the Adsorption of Proteins. *Adv. Mater.* **2009**, *21* (23), 2441–2446.

(205) Gon, S.; Fang, B.; Santore, M. M. Interaction of Cationic Proteins and Polypeptides with Biocompatible Cationically-Anchored PEG Brushes. *Macromolecules* **2011**, *44* (20), 8161–8168.

(206) Kenausis, G. L.; Vörös, J.; Elbert, D. L.; Huang, N.; Hofer, R.; Ruiz-Taylor, L.; Textor, M.; Hubbell, J. A.; Spencer, N. D. Poly(l -Lysine)- g -Poly(Ethylene Glycol) Layers on Metal Oxide Surfaces: Attachment Mechanism and Effects of Polymer Architecture on Resistance to Protein Adsorption †. *J. Phys. Chem. B* **2000**, *104* (14), 3298–3309.

(207) Huang, N.; Michel, R.; Vörös, J.; Textor, M.; Hofer, R.; Rossi, A.; Elbert, D. L.; Hubbell, J. a; Spencer, N. D. Poly (l-Lysine) -g-Poly (Ethylene Glycol) Layers on Metal Oxide Surfaces : Surface-Analytical Characterization and Resistance to Serum and Fibrinogen Adsorption Poly (L -Lysine) -g-Poly (Ethylene Glycol) Layers on Metal Oxide Surfaces : Surface-An. *Langmuir* **2001**, *17* (2), 489–498.

(208) Huang, N.; Vörös, J.; De Paul, S. M.; Textor, M.; Spencer, N. D. Biotin-Derivatized Poly(L-Lysine)-g-Poly(Ethylene Glycol): A Novel Polymeric Interface for Bioaffinity Sensing. *Langmuir* **2002**, *18* (1), 220–230.

(209) Gon, S.; Santore, M. M. Sensitivity of Protein Adsorption to Architectural Variations in a Protein-Resistant Polymer Brush Containing Engineered Nanoscale Adhesive Sites. *Langmuir* **2011**, *27* (24), 15083–15091.

(210) Fang, B.; Gon, S.; Park, M.; Kumar, K. N.; Rotello, V. M.; Nusslein, K.; Santore, M. M. Bacterial Adhesion on Hybrid Cationic Nanoparticle-Polymer Brush Surfaces: Ionic Strength Tunes Capture from Monovalent to Multivalent Binding. *Colloids Surfaces B Biointerfaces* **2011**, *87* (1), 109–115.

(211) Morales-Soto, N.; Anyan, M. E.; Mattingly, A. E.; Madukoma, C. S.; Harvey, C. W.; Mark, A.; Déziel, E.; Kearns, D. B.; Shrout, J. D. Preparation, Imaging, and Quantification of Bacterial Surface Motility Assays. *J. Vis. Exp.* **2015**, No. 98, 1–10.

(212) Kearns, D. B. A Field Guide to Bacterial Swarming Motility. *Nat Rev Micro 8* (9), 634–644.

(213) Swiecicki, J. M.; Sliusarenko, O.; Weibel, D. B. From Swimming to Swarming: Escherichia Coli Cell Motility in Two-Dimensions. *Integr. Biol. (United Kingdom)* **2013**, *5* (12), 1490–1494.

(214) Blair, D. F.; Berg, H. C. The MotA Protein of E. Coli Is a Proton-Conducting Component of the Flagellar Motor. *Cell* **1990**, *60* (3), 439–449.

(215) Chattopadhyay, S.; Moldovan, R.; Yeung, C.; Wu, X. L. Swimming Efficiency of Bacterium Escherichia Coli. *Proc. Natl. Acad. Sci.* **2006**, *103* (37), 13712–13717.

(216) Darnton, N. C.; Turner, L.; Rojevsky, S.; Berg, H. C. On Torque and Tumbling in Swimming Escherichia Coli. *J. Bacteriol.* **2007**, *189* (5), 1756–1764.

(217) Fang, B.; Jiang, Y.; Rotello, V. M.; Nüsslein, K.; Santore, M. M. Easy Come Easy Go: Surfaces Containing Immobilized Nanoparticles or Isolated Polycation Chains Facilitate Removal of Captured Staphylococcus Aureus by Retarding Bacterial Bond Maturation. *ACS Nano* **2014**, *8* (2), 1180–1190.

(218) Ortega, A.; Garcia De La Torre, J. Hydrodynamic Properties of Rodlike and Dislike Particles in Dilute Solution. *J. Chem. Phys.* **2003**, *119* (18), 9914–9919.

(219) Shave, M. K.; Kalasin, S.; Ying, E.; Santore, M. M. Nanoscale Functionalized Particles with Rotation-Controlled Capture in Shear Flow. *ACS Appl. Mater. Interfaces* **2018**, *10* (34), 29058–29068.

(220) Razavi, S.; Kretzschmar, I.; Koplik, J.; Colosqui, C. E. Nanoparticles at Liquid Interfaces: Rotational Dynamics and Angular Locking. *J. Chem. Phys.* **2014**, *140* (1).

(221) Cui, J.; Long, D.; Shapturenka, P.; Kretzschmar, I.; Chen, X.; Wang, T. Janus Particle-Based Microprobes: Determination of Object Orientation. *Colloids Surfaces A Physicochem. Eng. Asp.* **2017**, *513*, 452–462.

(222) Schwarz-Linek, J.; Arlt, J.; Jepson, A.; Dawson, A.; Vissers, T.; Miroli, D.; Pilizota, T.; Martinez, V. A.; Poon, W. C. K. Escherichia Coli as a Model Active Colloid: A Practical Introduction. *Colloids Surfaces B Biointerfaces* **2016**, *137*, 2–16.

(223) Belas, R. Biofilms, Flagella, and Mechanosensing of Surfaces by Bacteria. *Trends Microbiol.* **2014**, *22* (9), 517–527.

(224) Kolewe, K. W.; Peyton, S. R.; Schiffman, J. D. Fewer Bacteria Adhere to Softer Hydrogels. *ACS Appl. Mater. Interfaces* **2015**, *7* (35), 19562–19569.

(225) Song, F.; Brasch, M. E.; Wang, H.; Henderson, J. H.; Sauer, K.; Ren, D. How Bacteria Respond to Material Stiffness during Attachment: A Role of Escherichia Coli Flagellar Motility. *ACS Appl. Mater. Interfaces* **2017**, *9* (27), 22176–22184.

(226) Flemming, H.-C.; Wingender, J. The Biofilm Matrix. *Nat. Rev. Microbiol.* **2010**, *8*, 623–633.

(227) CDC. Antibiotic Resistance Threats in the United States, 2013. **2013**, 114.

(228) Hori, K.; Matsumoto, S. Bacterial Adhesion: From Mechanism to Control. *Biochem. Eng. J.* **2010**, *48* (3), 424–434.

(229) van Loosdrecht, M. C.; Lyklema, J.; Norde, W.; Zehnder, A. J. Influence of Interfaces on Microbial Activity. *Microbiol. Rev.* **1990**, *54* (1), 75–87.

(230) Hermansson, M. The DLVO Theory in Microbial Adhesion. *Colloids Surfaces B Biointerfaces* **1999**, *14* (1–4), 105–119.

(231) Katsikogianni, M.; Missirlis, Y. F. Concise Review of Mechanisms of Bacterial Adhesion to Biomaterials and of Techniques Used in Estimating Bacteria-Material Interactions. *Eur. Cells Mater.* **2004**, *8*, 37–57.

(232) Poortinga, A. T.; Bos, R.; Norde, W.; Busscher, H. J. *Electric Double Layer Interactions in Bacterial Adhesion to Surfaces*; 2002; Vol. 47.

(233) O'Toole, G. A.; Wong, G. C. L. Sensational Biofilms: Surface Sensing in Bacteria. *Curr. Opin. Microbiol.* **2016**, *30* (1999), 139–146.

(234) Lichter, J. A.; Thompson, M. T.; Delgadillo, M.; Nishikawa, T.; Rubner, M. F.; Van Vliet, K. J. Substrata Mechanical Stiffness Can Regulate Adhesion of Viable Bacteria. *Biomacromolecules* **2008**, *9* (6), 1571–1578.

(235) Saha, N.; Monge, C.; Dulong, V.; Picart, C.; Glinel, K. Influence of Polyelectrolyte Film Stiffness on Bacterial Growth. *Biomacromolecules* **2013**, *14* (2), 520–528.

(236) Bakker, D. P.; Huijs, F. M.; De Vries, J.; Klijnstra, J. W.; Busscher, H. J.; Van Der Mei, H. C. Bacterial Deposition to Fluoridated and Non-Fluoridated Polyurethane Coatings with Different Elastic Modulus and Surface Tension in a Parallel Plate and a Stagnation Point Flow Chamber. *Colloids Surfaces B Biointerfaces* **2003**, *32* (3), 179–190.

(237) Sae-Ung, P.; Kolewe, K. W.; Bai, Y.; Rice, E. W.; Schiffman, J. D.; Emrick, T. S.; Hoven, V. P. Antifouling Stripes Prepared from Clickable Zwitterionic Copolymers. *Langmuir* **2017**, *33* (28), 7028–7035.

(238) Nejadnik, M. R.; van der Mei, H. C.; Norde, W.; Busscher, H. J. Bacterial Adhesion and Growth on a Polymer Brush-Coating. *Biomaterials* **2008**, *29* (30), 4117–4121.

(239) Cheng, G.; Zhang, Z.; Chen, S.; Bryers, J. D.; Jiang, S. Inhibition of Bacterial Adhesion and Biofilm Formation on Zwitterionic Surfaces. *Biomaterials* **2007**, *28* (29), 4192–4199.

(240) Hsu, L. C.; Fang, J.; Borca-Tasciuc, D. A.; Worobo, R. W.; Moraru, C. I. Effect of Micro- and Nanoscale Topography on the Adhesion of Bacterial Cells to Solid Surfaces. *Appl. Environ. Microbiol.* **2013**, *79* (8), 2703–2712.

(241) Singh, A. V.; Vyas, V.; Patil, R.; Sharma, V.; Scopelliti, P. E.; Bongiorno, G.; Podestà, A.; Lenardi, C.; Gade, W. N.; Milani, P. Quantitative Characterization of the Influence of the Nanoscale Morphology of Nanostructured Surfaces on Bacterial Adhesion and Biofilm Formation. *PLoS One* **2011**, *6* (9).

(242) Kolewe, K. W.; Zhu, J.; Mako, N. R.; Nonnenmann, S. S.; Schiffman, J. D. Bacterial Adhesion Is Affected by the Thickness and Stiffness of Poly(Ethylene Glycol) Hydrogels. *ACS Appl. Mater. Interfaces* **2018**, acsami.7b12145.

(243) Gu, H.; Ren, D. Materials and Surface Engineering to Control Bacterial Adhesion and Biofilm Formation: A Review of Recent Advances. *Front. Chem. Sci. Eng.* **2014**, *8* (1), 20–33.

(244) Kolewe, K. W.; Dobosz, K. M.; Emrick, T.; Nonnenmann, S. S.; Schiffman, J. D. Fouling-Resistant Hydrogels Prepared by the Swelling-Assisted Infusion and Polymerization of Dopamine. *ACS Appl. Bio Mater.* **2018**, *1* (1), 33–41.

(245) Kolewe, K. W.; Kalasin, S.; Santore, M. M.; Schiffman, J. D. Mechanically Sensitive Surface Transport of Staphylococcus Aureus MW2 on Poly(Ethylene Glycol) Surfaces. *prep*.

(246) Herrick, W. G.; Nguyen, T. V.; Sleiman, M.; McRae, S.; Emrick, T. S.; Peyton, S. R. PEG-Phosphorylcholine Hydrogels as Tunable and Versatile Platforms for Mechanobiology. *Biomacromolecules* **2013**, *14* (7), 2294–2304.

(247) Bäckström, S.; Benavente, J.; Berg, R. W.; Stibius, K.; Larsen, M. S.; Bohr, H.; Hélix-nielsen, C. Tailoring Properties of Biocompatible PEG-DMA Hydrogels with UV Light. *Mater. Sci. Appl.* **2012**, *3* (June), 425–431.

(248) Zhang, Y.; Chan, H. F.; Leong, K. W. Advanced Materials and Processing for Drug Delivery: The Past and the Future. *Adv. Drug Deliv. Rev.* **2013**, *65* (1), 104–120.

(249) Ta, H. T.; Truong, N. P.; Whittaker, A. K.; Davis, T. P.; Peter, K. The Effects of Particle Size, Shape, Density and Flow Characteristics on Particle Margination to Vascular Walls in Cardiovascular Diseases. *Expert Opin. Drug Deliv.* **2018**, *15* (1), 33–45.

(250) Gratton, S. E. A.; Ropp, P. A.; Pohlhaus, P. D.; Luft, J. C.; Madden, V. J.; Napier, M. E.; DeSimone, J. M. The Effect of Particle Design on Cellular Internalization Pathways. *Proc. Natl. Acad. Sci.* **2008**, *105* (33), 11613–11618.

(251) Geng, Y.; Dalhaimer, P.; Cai, S.; Tsai, R.; Tewari, M.; Minko, T.; Discher, D. E. Shape Effects of Filaments versus Spherical Particles in Flow and Drug Delivery. *Nat. Nanotechnol.* **2007**, *2* (4), 249–255.

(252) Mitragotri, S. In Drug Delivery, Shape Does Matter. *Pharm. Res.* **2009**, *26* (1), 232–234.

(253) Li, K.; Ma, H. Deposition Dynamics of Rod-Shaped Colloids during Transport in Porous Media under Favorable Conditions. *Langmuir* **2018**, *34* (9), 2967–2980.

(254) Liu, Q.; Lazouskaya, V.; He, Q.; Jin, Y. Effect of Particle Shape on Colloid Retention and Release in Saturated Porous Media. *J. Environ. Qual.* **2010**, *39* (2), 500.

(255) Salerno, M. B.; Flamm, M.; Logan, B. E.; Velegol, D. Transport of Rodlike Colloids through Packed Beds. *Environ. Sci. Technol.* **2006**, *40* (20), 6336–6340.

(256) Ma, H.; Pedel, J.; Fife, P.; Johnson, W. P. Hemispheres-in-Cell Geometry to Predict Colloid Deposition in Porous Media. *Environ. Sci. Technol.* **2009**, *43* (22), 8573–8579.

(257) Tang, L.; Cheng, J. Nonporous Silica Nanoparticles for Nanomedicine Application. *Nano Today* **2013**, *8* (3), 290–312.

(258) Desai, N. Challenges in Development of Nanoparticle-Based Therapeutics. *AAPS J.* **2012**, *14* (2), 282–295.

(259) Venkataraman, S.; Hedrick, J. L.; Ong, Z. Y.; Yang, C.; Ee, P. L. R.; Hammond, P. T.; Yang, Y. Y. The Effects of Polymeric Nanostructure Shape on Drug Delivery. *Adv. Drug Deliv. Rev.* **2011**, *63* (14–15), 1228–1246.

(260) Decuzzi, P.; Godin, B.; Tanaka, T.; Lee, S. Y.; Chiappini, C.; Liu, X.; Ferrari, M. Size and Shape Effects in the Biodistribution of Intravascularly Injected Particles. *J. Control. Release* **2010**, *141* (3), 320–327.

(261) Decuzzi, P.; Ferrari, M. The Adhesive Strength of Non-Spherical Particles Mediated by Specific Interactions. *Biomaterials* **2006**, *27* (30), 5307–5314.

(262) Shinde Patil, V. R.; Campbell, C. J.; Yun, Y. H.; Slack, S. M.; Goetz, D. J. Particle Diameter Influences Adhesion under Flow. *Biophys. J.* **2001**, *80* (4), 1733–1743.

(263) Thomas, W. E.; Nilsson, L. M.; Forero, M.; Sokurenko, E. V.; Vogel, V. Shear-Dependent "stick-and-Roll" Adhesion of Type 1 Fimbriated Escherichia Coli. *Mol. Microbiol.* **2004**, *53* (5), 1545–1557.

(264) Kuijk, A.; Van Blaaderen, A.; Imhof, A. Synthesis of Monodisperse, Rodlike Silica Colloids with Tunable Aspect Ratio. *J. Am. Chem. Soc.* **2011**, *133* (8), 2346–2349.

(265) Kuijk, A.; Imhof, A.; Verkuijlen, M. H. W.; Besseling, T. H.; Van Eck, E. R. H.; Van Blaaderen, A. Colloidal Silica Rods: Material Properties and Fluorescent Labeling. *Part. Part. Syst. Charact.* **2014**, *31* (6), 706–713.

(266) Li, W.; Lu, K.; Walz, J. Y.; Anderson, M. Effects of Rod-like Particles on the Microstructure and Strength of Porous Silica Nanoparticle Composites. *J. Am. Ceram. Soc.* **2013**, *96* (2), 398–406.

(267) Peng, B.; Soligno, G.; Kamp, M.; de Nijs, B.; de Graaf, J.; Dijkstra, M.; van Roij, R.; van Blaaderen, A.; Imhof, A. Site-Specific Growth of Polymers on Silica Rods. *Soft Matter* **2014**, *10*, 9644–9650.

(268) Choma, J.; Jamioła, D.; Ludwinowicz, J.; Jaroniec, M. Deposition of Silver Nanoparticles on Silica Spheres and Rods. *Colloids Surfaces A Physicochem. Eng. Asp.* **2012**, *411*, 74–79.

(269) Yang, Y.; Chen, G.; Martinez-Miranda, L. J.; Yu, H.; Liu, K.; Nie, Z. Synthesis and Liquid-Crystal Behavior of Bent Colloidal Silica Rods. *J. Am. Chem. Soc.* **2016**, *138* (1), 68–71.

(270) Hagemans, F.; Van Der Wee, E. B.; Van Blaaderen, A.; Imhof, A. Synthesis of Cone-Shaped Colloids from Rod-Like Silica Colloids with a Gradient in the Etching Rate. *Langmuir* **2016**, *32* (16), 3970–3976.

(271) Datskos, P.; Chen, J.; Sharma, J. Addressable Morphology Control of Silica Structures by Manipulating the Reagent Addition Time. *RSC Adv.* **2014**, *4* (480), 2291–2294.

(272) Datskos, P.; Sharma, J. Synthesis of Segmented Silica Rods by Regulation of the Growth Temperature. *Angew. Chemie - Int. Ed.* **2014**, *53* (2), 451–454.

(273) Stöber, W.; Fink, A.; Bohn, E. Controlled Growth of Monodisperse Silica Spheres in the Micron Size Range. *J. Colloid Interface Sci.* **1968**, *26* (1), 62–69.

(274) Hierrezuelo, J.; Sadeghpour, A.; Szilagyi, I.; Vaccaro, A.; Borkovec, M. Electrostatic Stabilization of Charged Colloidal Particles with Adsorbed Polyelectrolytes of Opposite Charge. *Langmuir* **2010**, *26* (19), 15109–15111.

(275) Borkovec, M.; Szilagyi, I.; Popa, I.; Finessi, M.; Sinha, P.; Maroni, P.; Papastavrou, G. Investigating Forces between Charged Particles in the Presence of Oppositely Charged Polyelectrolytes with the Multi-Particle Colloidal Probe Technique. *Adv. Colloid Interface Sci.* **2012**, *179–182*, 85–98.

(276) Yang, Y. J.; Kelkar, A. V.; Corti, D. S.; Franses, E. I. Effect of Interparticle Interactions on Agglomeration and Sedimentation Rates of Colloidal Silica Microspheres. *Langmuir* **2016**, *32* (20), 5111–5123.